Open Ceramics 8 (2021) 100177

Contents lists available at ScienceDirect

Open Ceramics

journal homepage: www.sciencedirect.com/journal/open-ceramics

# Nano and micro-forms of calcium titanate: Synthesis, properties and application

T. Křenek [a], T. Kovářík [a], J. Pola [a,*], T. Stich [b], D. Docheva [b]

[a] New Technologies-Research Center, University of West Bohemia, Univerzitní 8, 306 14, Pilsen, Czech Republic
[b] Experimental Trauma Surgery, Department of Trauma Surgery, University Regensburg Medical Centre, 93042, Regensburg, Germany

ARTICLE INFO

*Keywords:*
Calcium titanate
Micro/nanoforms

ABSTRACT

This article reviews synthetic approaches, properties and potential use of nano and micron sized forms of particles and coats of calcium titanate $CaTiO_3$ and its composites. Our aim is to classify these forms according to the way of their fabrication and provide a brief outline of synthetic methods, properties and potential applications of these forms as inspired from luminescence, photocatalytic and catalytic performance, pollutants removal ability, inducement of biomimetic hydroxylapatite formation and bioengineering. The significance of the CT forms in luminescence-structure relationship, biomimetic calcium phosphates formation and osseointegration with bone tissue are dealt with in more detail.

## 1. Introduction

Calcium titanate $CaTiO_3$ (CT) belonging to metal titanate compounds with a perovskite structure has aroused ongoing interest in fundamental and applied research of materials. It is known as an impressively chemical resistant n-type semiconductor, a ceramic dielectric with high dielectric constant, a thermal resistive element due to its negative temperature coefficient [1–3], and its structural [4,5], electric and optical [6–9] properties have been widely examined particularly due to flexibility in its structural transformations [5,10] and applications in ferroelectric and dielectric ceramic materials, high performance capacitors, sensors, electroluminescent devices, radioactive waste and microwave communication systems.

Great attention has been also given to the development of nano- and micron-sized CT particles, films and composites. These species possess specific properties due to their high surface areas and small sizes and are applied in environmental remediation, electronics, catalytic and photocatalytic processes, biomimetic calcium phosphates formation and biomedical engineering.

CT can exist in an amorphous or crystalline orthorhombic, tetragonal or cubic structures (Fig. 1) among those the high temperature cubic phase is stable above 1374 °C, tetragonal phase is stable at 1250–1350 °C and the orthorhombic phase is stable below 1213 °C [11,12]; these values little differ from those of earlier studies [5,13]. The reversible orthorhombic (Pbmm) ↔ tetragonal (*I*4/mcm) ↔ cubic (Pm3 m) phase transitions respectively assigned near 1225 °C and 1360 °C [11,12] reflect the temperature dependent orthorhombic distortions induced by tilting of the TiO6 octahedra.

As a consequence, many micro- and nanosized CT phases of this review measured at ambient temperature are regarded orthorhombic and only very few are considered cubic. However, the CT perovskite has long been considered as a non-polar material and it was only recently [14] that a new polar phase occurring in nanoparticles, ultrathin films or even on surface layer of bulk single crystals has been detected and shown to originate from $TiO_6$ octahedron distortion and to undergo non-apparent polar to non-polar isostructural transition within the stable orthorhombic CT phase above ambient temperature. The term “orthorhombic”, often given in the Tables, thus overlooks possible occurrence of this nanophase which can be detected only by using nonlinear optics and spectroscopy, X-ray diffraction, and microscopy studies.

In this article we review synthetic approaches to various nano- and micron-sized CT particles, coats and composites and show how their distinctive physical and chemical properties have been applied in the abovementioned fields of research. With many syntheses reported, we preferred to classify these three different CT entities according to the mode of their synthesis and to append notes on properties and potential applications of each entity obtained via the distinctive procedure. Such classification is then ensued by several sections showing importance of some CT entities in several specific fields of nowadays interest.

* Corresponding author.
*E-mail address:* pola@icpf.cas.cz (J. Pola).

https://doi.org/10.1016/j.oceram.2021.100177
Received 5 June 2021; Received in revised form 22 August 2021; Accepted 24 August 2021
Available online 27 August 2021

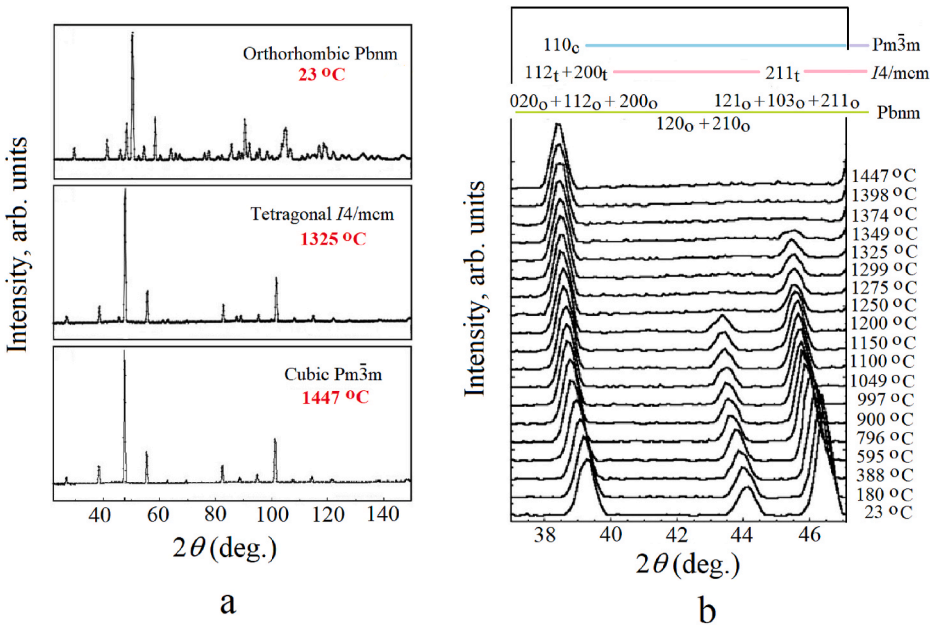


**Fig. 1.** Rietveld patterns of neutron diffraction data of orthorhombic, tetragonal and cubic phase of CT (a) and selected neutron diffraction patterns of CT at 23–1447 °C (b) showing the orthorhombic ($020_o$, $112_o$, $200_o$, $120_o$, $210_o$, $121_o$, $103_o$ and $211_o$) reflections at 23–1200 °C, the tetragonal ($112_t$, $200_t$, and $211_t$) reflections at 1250–1349 °C and the cubic $110_c$ reflection between 1374 and 1447 °C. (The $hkl_o$, $hkl_t$, and $hkl_c$ respectively denote the hkl reflections of the orthorhombic, tetragonal and cubic phases.) Adapted from refs. 11 and 12, Copyright Elsevier.

**Table 1**
Heating of $TiO_2$–CaO and $TiO_2$–$CaCO_3$ mixtures.

| Heating conditions | CT particles properties | CT particles application | Ref. |
|---|---|---|---|
| Stoichiometric CaO–$TiO_2$, CaO from snail shell-$TiO_2$ and $CaCO_3$–$TiO_2$ amounts, mortar-pestle grinding for 20 min, 2 h heating at 200° C | Orthorhombic phase, $SiO_2$, MgO and $Si_5P_6O_{25}$ impurities from calcined snail shell and unreacted reactants | UV light photo-induced degradation of aqueous methylene blue (MB) dye | [15] |
| Stepwise heating, cooling and mortar-pestle grinding of stoichiometric CaO–$TiO_2$ until final 20 h heating at 1000° C | Orthorhombic phase, BET surface area 300 $m^2$/g, sizes 90 nm-2 μm | Solar light photo-induced degradation of aqueous MB dye; antimicrobial activity | [16] |
| Heating of 1:1 and 3:2 proportions of $CaCO_3$–$TiO_2$ in three thermal-cooling-grinding cycles, final heating at 1150 °C | Orthorhombic phase, CaO and $TiO_2$ impurities, particle sizes 10 μm and 8.4 μm | High resistivity at room temperature, possible use as thermistors | [17] |
| Stoichiometric $CaCO_3$–$TiO_2$ amounts ground in mortar for 30 min and heated at 900° C for 2 h | Orthorhombic, 50 nm-sized spherical particles with $CaCO_3$ traces, Band gap 3.39 eV, Crystalline Scherer size 42 nm | Thermoluminescence of γ-irradiated nanophosphor | [18] |
| Griding stoichiometric $CaCO_3$–$TiO_2$ amounts in agate mortar and heating up to 500° C and 2 h at 1050° C | Crystalline, Surface area 4.9 $m^2$/g | Catalyst for transesterification of oil aimed at effective biodiesel production | [19] |

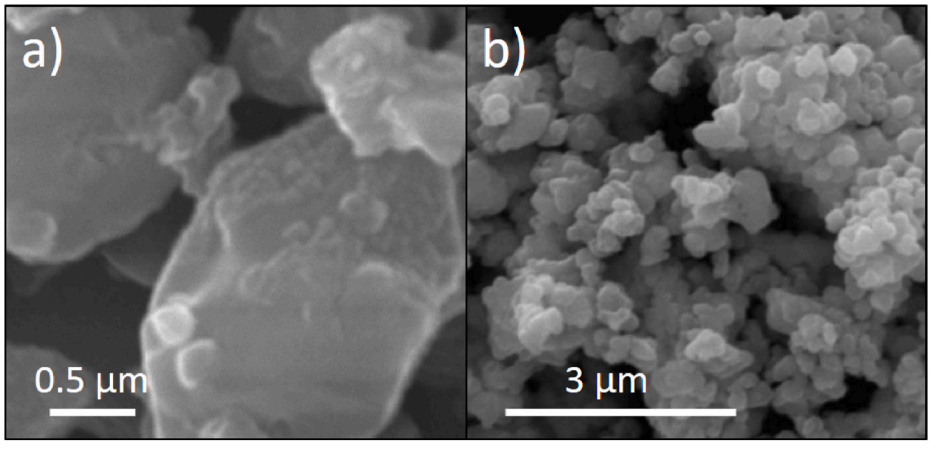


**Fig. 2.** SEM images of CT particles prepared in a (adapted from ref. 16, Copyright Der Pharma Chemica) and b (adapted from ref. 18, Copyright Elsevier).

## 2. Nano and micro $CaTiO_3$ particles – synthesis and use

Many synthetic procedures of nano- and micro-sized CT particles which differ in phase, size, shape, morphology, arrangement of subunits into various three-dimensional ultrafine structures have been reported within last 4 decades with the aim to discover new properties of these particles and their potential application. These procedures can be classified into traditional solid state reactions and advanced wet chemical routes. The former processes are accomplished by conventional annealing, microwave irradiation and/or mechanical milling of binary mixtures of Ca- and Ti-containing CT precursors with or without a mineralization compound or they involve thermal decomposition of a

**Table 2**
Mechanical activation of $TiO_2$–CaO, $Ca(OH)_2$ or $CaCO_3$) mixtures.

| Conditions | CT particles properties | Ref. |
|---|---|---|
| CaO-rutile 100 h milling | Scherrer crystallite size 11–12 nm | [23] |
| CaO-rutile and $CaCO_3$-rutile 4 h milling | μm-sized particles | [24] |
| $CaCO_3$–$TiO_2$Optimal ball/powder ratio, 70 h milling | Different morphologies 30–70 nm particles | [25] |
| $Ca(OH)_2$–$TiO_2$, Optimal ball/powder ratio, 60 h milling | Cubic phase, Zeta size 20–120 nm, soft μm-sized agglomerates | [26] |
| CaO-anatase, 6 h milling | Orthorhombic phase, agglomerated nanocrystals grow to 125 nm upon annealing | [27] |
| $CaCO_3$–$TiO_2$, 5 h milling, | 10 nm-sized crystallites in amorphous phase | [28] |
| CaO-anatase, CaO rutile 2–5 h discontinuous milling | Microcrystals with 5 nm grains grow to 20–50 nm within longer milling | [29, 30] |
| CaO- anatase CaO-rutile 240 h milling | Crystalline μm and sub-μm-sized powder, BET surface area from CaO- anatase 15.5 $m^2/g$ CaO-rutile 10.7 $m^2/g$ | [31] |
| CaO–$TiO_2$ 1.5 h milling | Sub-μm sized particles stabilized against agglomeration in water by acrylic-poly(ethyleneglycol) suspensions | [32] |
| CaO–$TiO_2$ 7–15 h milling | Orthorhombic phase, Scherrer crystallite size 28–30 nm, fast response time and enhanced sensing behavior of resistance thermistor material | [33] |
| CaO-rutile 4 h milling | Pure crystalline particles | [34] |

**Table 3**
Mechanochemical reactions combined with additional heating.

| Synthetic conditions | CT particles properties | CT particles application | Ref. |
|---|---|---|---|
| $CaCO_3$-rutile, $CaCO_3$-anatase; a sequence of 100 h milling in $H_2O$, drying, 70 h milling and annealing either at 800° C (anatase) or 1000° C (rutile) | Crystalline | | [35] |
| CaO-rutile, CaO-anatase, $Ca(OH)_2$-rutile, $Ca(OH)_2$-anatase; 2 h grinding, heating 627–927° C | Crystalline | | [29] |
| $CaCO_3$–$TiO_2$;1 h milling and 2 h heating at 920° C | Crystalline, uniform spherical shape, crystallite size 120 nm | | [36] |
| $CaCO_3$-anatase;2 h two step milling (EtOH presence),2 h calcination at 700° C | Crystalline Mass median particles diameter 17 μm | Catalyst for methanolysis of sunflower oil at 165° C | [37] |
| $CaCO_3$-rutile: 8 h discontinuous milling ensued by 4 h heating at 700° C. $Ca(OH)_2$-rutile: 4 h discontinuous milling ensued by 2 h heating at 700° C | Pure crystalline | | [34] |
| $CaCO_3$–$TiO_2$; 1 h milling and 2 h heating at 850° C | Crystalline, agglomerated μm-sized particles Surface area of particles milled for 6 h −3.25 $m^2/g$ | | [38] |

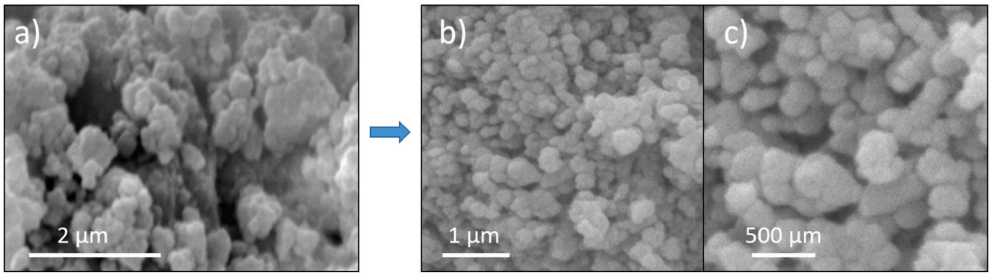


**Fig. 3.** Morphology change of milled CT particles by short extra annealing demonstrated at different magnification (a and b) of annealed product. Reproduced from ref. 25, Copyright Int. J. Phys. Sci.

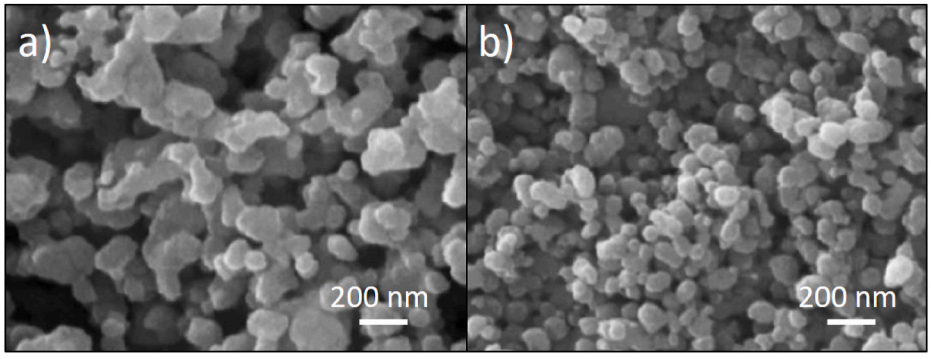


**Fig. 4.** SEM images of the non-activated (a) and activated (b) CT samples annealed at 900 °C. Reproduced from ref. 36, Copyright Elsevier.

**Table 4**
Solid state syntheses at lower temperatures.

| Synthetic conditions | CT particles properties | CT particles application | Ref. |
|---|---|---|---|
| Low temperature synthesis from $Ca(NO_3)_2{\cdot}4H_2O$ and $TiO_2$ nanocrystals, 10 h heating to only 600° C | Orthorhombic aggregates of oxygen-deficient 26–60 nm particles having UV and visible absorption and strong visible light emission at 527–568 nm | Green light-luminescent material<br>Matrix for immobilization of enzyme, electrochemical biosensor | [39]<br>[40] |
| Mixing $CaCl_2.2H_2O$ and $TiO_2$ powders, pressing, sintering at 800° C, leaching, washing and drying. | Crystalline 1–10 μm particles | | [41] |
| $CaCl_2$ -$TiO_2$ sintering with $Pb(Ac)_2.3H_2O$ (mineralization agent),4 h heating at 780 °C | 50–100 μm whiskers | Piezoelectric ceramics | [43] |
| 2 h grinding of tetra-*n*-butyl titanate with hydrated calcium nitrate and 2 h annealing at 700° C | Orthorhombic,<br>Agglomerated oval sub-micron particles, band gap 3.37 eV<br>Scherer crystallite size 37 nm | Thermoluminescence of γ-irradiated nanophosphor | [18] |

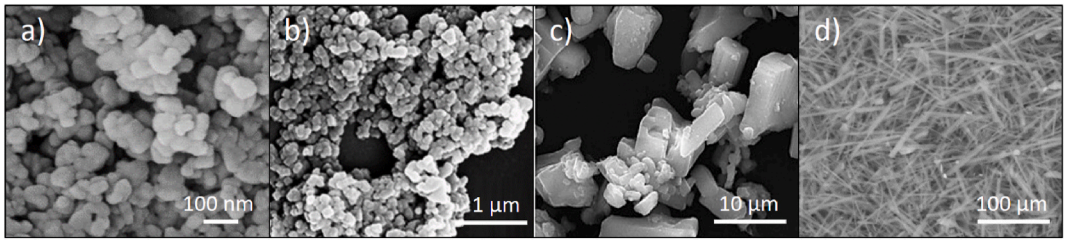


**Fig. 5.** SEM images of nano- and μm-sized CT particles produced by lower temperature processes; reproduced from ref. 39 (a), ref. 40 (b), ref. 41 (c), all Copyright Elsevier and from ref. 43 (d), Copyright Trans Tech Publications, Ltd.

**Table 5**
Thermal decomposition of single source precursor.

| Synthetic conditions | CT particles properties | CT particles application | Ref. |
|---|---|---|---|
| Calcium titanyl oxalate1 h heating at 900° C | Agglomerated sub-μm particles | | [44] |
| Calcium titanyl oxalate<br>1 h microwave heating at 500 and 700° C or conventional heating at 700 °C | Crystalline μm bodies of specific surface area 11.8 and 5.6 $m^2/g$ formed by microwave heating at respective 500° C and 700° C.<br>Smaller than 100 nm-sized nanoparticles with specific surface area 8.7 $m^2/g$ formed by conventional heating at 700° C | | [45] |
| Ca nitrilotriacetatoperoxotitanate<br>2 h heating at 675° | Aggregates of 40–100 nm sized particles, BET specific surface area 14.0 $m^2/g$, dielectric ceramic properties of sintered CT disc annealed at 1250° C | | [46] |
| Ca nitrilotriacetatoperoxotitanate microwave pretreatment and heating at 680° C | Agglomerated irregularly shaped μm-sized particles made of crystalline mesoporous entities smaller than 100 nm, specific surface area ~20 $m^2/g$ and pore diameter effected by microwave pretreatment | | [47] |
| Ca titanyl citrate<br>9 h heating up to 600° C and 700° C | Respective surface areas 28 or 10 $m^2/g$,<br>Respective E gap 3,0 or 3.50 eV | Catalyst for oxidation of harmful 2-(methylthio)- benzothiazole | [48] |
| Ca catecholate $Ca[Ti(C_6H_4O_2)_3]$, $H_2O$, 1 h heating at 600° C | Crystallite size ~ 50 nm, ultrasonically dispersed particles in water are ~ 3 μm big and their surface area is 10 $m^2/g$ | | [50] |
| Layer-structured $CaBi_4Ti_4O_{15}$ compound Sintering at 950° C | Crystalline μm thin-mm sized plates | Ceramic with improved microwave dielectric low-loss properties | [51] |

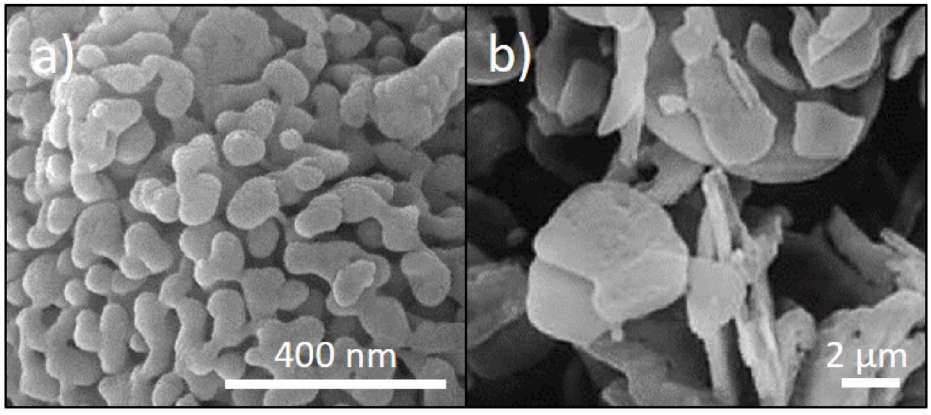


**Fig. 6.** SEM images of agglomerated nanoparticles (a, reproduced from ref. 46, Copyright Elsevier) and platelike shaped particles (b, reproduced from ref. 51, Copyright Elsevier).

**Table 6**
Syntheses by solution combustion.

| Synthetic conditions | CT particles properties | CT particles application | Ref. |
|---|---|---|---|
| Solution of calcium nitrate- titanyl nitrate (precursors)-tetra formyl tris-azine (fuel), furnace temperature 450° C, crystalization at ~ 900° C | Specific surface area 21 $m^2$/g, agglomerated particles, average size 0.9 μm | | [54] |
| Solution of calcium nitrate-titanyl nitrate (precursors)-urea (fuel), furnace temperature 500° C | Orthorhombic phase, agglomerated porous and irregularly shaped μm-sized particles, Scherer crystal size 43 nm, band gap 3.34 eV | Thermoluminescence of γ-irradiated nanophosphor | [18] |
| Solution of calcium nitrate and Ti peroxo complex (precursors)-tartaric acid (fuel), Furnace temperature 550° C | TEM particle size 30–70 nm, BET surface area ~30.89 $m^2$/g, band gap 3.54 eV, Photoluminescence, frequency dependence of dielectric constant | Solar light photocatalyst for degradation of MB dye | [55] |
| Ultrasonic generation of aerosol from solution of citric acid, Ca nitrate and Ti isopropoxide sprayed onto furnace flown with $N_2$/$O_2$ gas at 750° C | Orthorhombic, crystallite size 6–9 nm, smooth surface spheres large 1–5 μm | Promising catalyst | [56] |

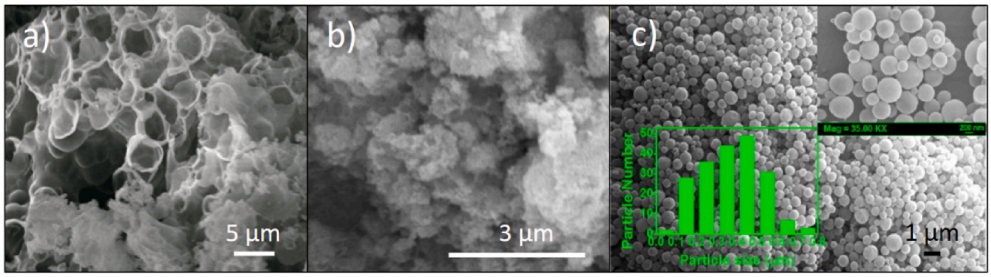


**Fig. 7.** SEM images of highly porous and agglomerated particles with polycrystalline nanoparticles (a, reproduced from ref. 55, Copyright Bentham Science Publishers), agglomerated particles with irregular shape and size (b, reproduced from ref. 18, Copyright Elsevier) and spherical particles (c, reproduced from ref. 56, Copyright Elsevier).

**Table 7**
Simple sol-gel synthesis and gel annealing.

| Synthetic conditions | CT particles properties | CT particles application | Ref. |
|---|---|---|---|
| Ca acetate, Ti isopropoxide, in butanol, transparent gel dried at 110° C and heated at 900° C | Crystalline, agglomerated particles of mean diameter 70 nm, surface area 21 $m^2$/g | | [57] |
| Ca nitrate, Ti isopropoxide, citric acid, in isopropanol, gel dried 96 h at 50° C and heated 1 h at 600° C | Orthorhombic phase, irregularly shaped particles of median size 27 nm, BET surface area 43.9 $m^2$/g, zero point charge at 3.5 pH | Adsorbent of $As^{III}$ from aqueous solutions | [58] |
| Ca nitrate, Ti isopropoxide, in ethanol, viscous gel dried 2 h at 200° C and heated 1 h at 750° C | Agglomerated nanocrystals, Scherrer crystallite size 49 nm, homogeneously dispersed particles in crosslinked poly (glycerol sebacate) | Biodegradable elastomer in soft tissue engineering | [59] |
| $CaCl_2$, Ti isopropoxide, citric acid, in ethanol, gel dried 24 h at 80° C and heated 2 h at 500, 700, 900° C | Orthorhombic phase, average crystallite size 27, 32, 39 nm, surface area or 48 or 73 $m^2$/g, spongy or spherical particles, band gap 3.03, 2.95, 2.82 eV, photoluminescence | Solar light photocatalyst for degradation of MB and Rhodamine B (RhB) dyes | [60] |
| Ca nitrate, Ti butoxide, chelating oxalic, salicylic or cinnamic acid, in ethanol 2.5 h gel calcination at 700° C | Crystallite Scherrer size 9 nm, Particle size 40–50 nm, Band gap 3.35 eV, | UV light photocatalyst of degradation of aqueous Methyl orange (MO) dye, room temperature ferromagnetism | [61] |
| Hydrated Ca nitrate, Ti butoxide, citric acid, in EtOH, 12 h drying at 80° C, 3 h calcination at 700° C | Orthorhombic, irregularly shaped 0.1–5 μm particles, Scherrer crystallite size 34 nm, band gap 3.42 eV | Photocatalyst of UV–vis light degradation of MB dye | [62] |
| Ca nitrate, Ti isopropoxide, acetylacetone inhibitor, lauryl amine hydrochloride as structure directing surfactant, in ethanol; yellow gel dried 2 h at 80° C and heated 4 h at 500–650° C | Cubic crystalline mesoporous phase, surface area 35 and 15 $m^2$/g, mean mesopore diameter 6.12–15. 8 nm, band gap 3.55–3.59 eV, surface area 9.7 $m^2$/g, | Visible light photocatalyst of $H_2$ production from $H_2O$, sensitized by Eosin Y | [63] |

single pre-synthesized solid state precursor. The latter processes are called solution combustion, sol-gel, hydrothermal, solvothermal and peroxo complex approach involve different multistep reactions occurring in aqueous phase and are more suitable for engineering novel architectures through particle growth control.

### 2.1. Solid state reactions

#### 2.1.1. Heating of binary mixtures

Conventional heating of milled mixtures of ultrafine powders of CaO or $CaCO_3$ with $TiO_2$ was broadly used as a relatively easy and low cost synthesis of CT particles. However, it has some drawbacks of non-uniform particles distribution and the presence of unreacted precursors and contaminants acquired during the subsequent grinding process, which have negative impact on CT properties. Very high temperatures are required owing to the reluctance of direct reactions between the solid reactants. $CaCO_3$ releases $CO_2$ to form CaO above 700 °C and melting points of $TiO_2$ (1843 °C) and CaO (2613 °C) are extremely high. Ultrafine CT powders were thus initially prepared by heating stoichiometric amounts of CaO and $TiO_2$ at 1350 °C for several hours during which time the proportions of both reactants were maintained [4]. Later synthetic studies encompassed different heating conditions of

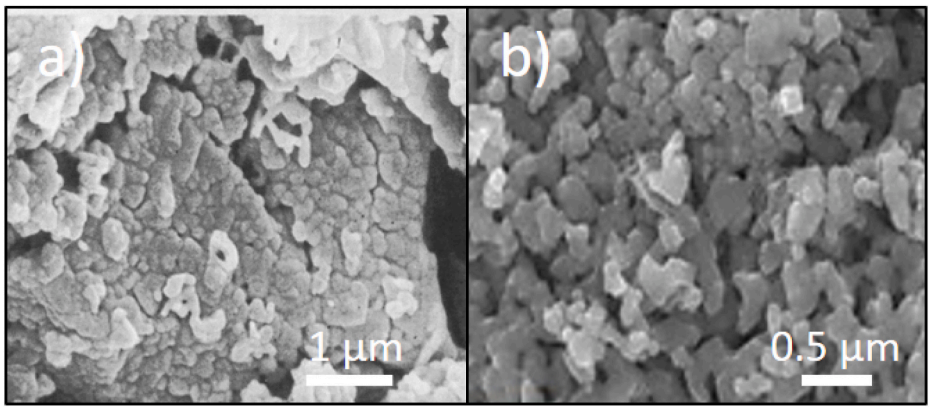


**Fig. 8.** SEM images of sintered irregular nanoparticles (a, reproduced from ref. 57, Copyright American Chemical Society) and oval nanoparticles (b, reproduced from ref. 60, Copyright Elsevier).

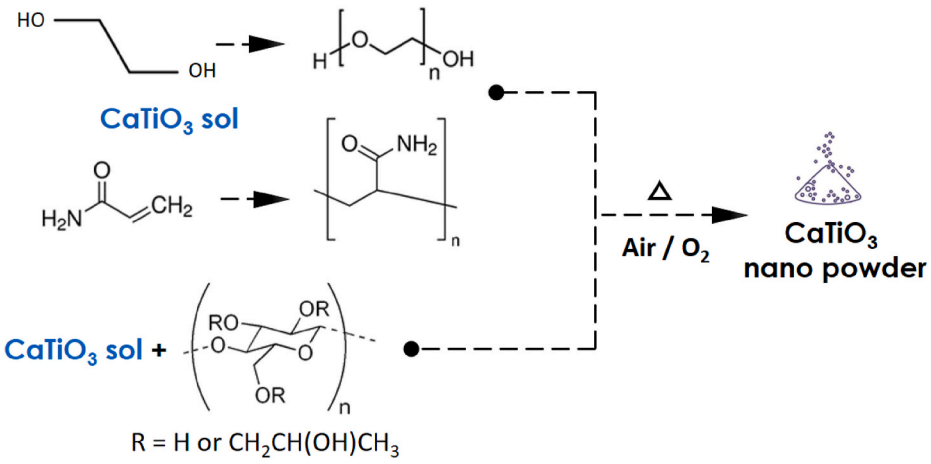


**Scheme 1.** Incorporation of CT sol into polymerizing ethylene glycol and acryl amide and hydroxypropyl cellulose.

mixed CaO–$TiO_2$ and $CaCO_3$–$TiO_2$ mixtures combined with the grinding of the heated mixtures in agate mortar and they aimed at the recognition of various potential uses of different CT particles as solar-light photocatalyst, thermistor, antimicrobial agent and phosphor. Heating conditions of the binary mixtures, properties of prepared CT particles and their potential applications are given in Table 1. Examples of an appearance and facile self-agglomerization of CT nanoparticles are given in Fig. 2.

*2.1.2. Mechanical activation of binary mixtures*

This method, also called mechanical alloying, is a solid-state powder process at ambient temperature and consists in high energy milling of powdered mixtures of two solid components, one either CaO or $CaCO_3$ and another rutile or anatase. In such ball-milling or grinding process, solid particles come into intimate contact with mechanical forces which induce physical changes on their surface [20], thereby enabling the outmost surface regions of particles to undergo chemical reactions above temperatures being by 0.4–0.5 times lower than the melting points of the inorganic solids. These reactions are feasible due to increased mobility of species (defects) in the near-surface regions [21,22] and they result in creation of previously unexposed surfaces, particles disintegration and also involve aggregation and agglomeration phenomena which control the size distribution of final particles. The procedures given in Table 2 concern single mechanochemical treatments of binary mixtures, whereas those given in Table 3 show these treatments ensued by conventional heating and confirm that the development of CT grains in the post-annealed mixtures occurs at lower temperatures due to pre-activation of the reactant particles by mechanical forces.

The milling of CaO - $TiO_2$ mixtures is facile as leading to single CT phase in short times [23,24,27], whereas milling of $CaCO_3$–$TiO_2$ mixtures is accompanied by an increase in $CO_2$ pressure and is therefore hampered by the necessity to reduce $CO_2$ pressure during the milling [24]. Such milling is lengthy [25] but can be used to prepare activated powders composed of mixed phases for further low temperature sintering. The milled particles are very reactive and susceptible to agglomeration and their further short annealing results in de-agglomeration (Fig. 3).

Optimal milling conditions of an equimolar $Ca(OH)_2$-anatase mixture with ethanol allow formation of CT nanoparticles which have been proven by XRD analysis to have diffraction pattern correlating with (220), (400), (422) and (440) planes of cubic crystal structure [26]. The mechanochemical formation of CT from anatase and CaO thermally produced from $CaCO_3$ is more facile than the analogous CT formation from rutile [28].

The cooperative use of the mechanochemical and heating effects shows that the solid state CT synthesis starting from the milled mixtures of $CaCO_3$ and $TiO_2$ (both rutile and anatase) permits a complete formation of crystalline CT, whereas the same annealing without the initial milling results in an incomplete formation of CT [35]. The pre-milling also results in the formation of smaller CT particles (Fig. 4).

The relevance of the combination of both effects has also been demonstrated with $Ca(OH)_2$- anatase or $Ca(OH)_2$-rutile mixtures by proving that both discontinuously ground mixtures yield crystalline CT contaminated with precursors impurities but effectively yield pure crystalline CT phase after additional heating at 627–927 °C [30]. Similar favorable effect has also been found in mechanically activated and

**Table 8**
Synthesis via sol-gel complex/polymer precursor and annealing.

| Synthetic conditions | CT particles properties | CT particles application | Ref. |
|---|---|---|---|
| Ti isopropoxide, $CaCO_3$, anhydrous citric acid, ethylene glycol; 4 h heating of resin at 350° C for better pulverization, 2 h calcination at 400 and 500° C and microwave irradiation | Orthorhombic phase, average Scherrer crystallite sizes 21–28 nm, band gap 2.58–3.42 eV; high structural organization degree of microwave irradiated samples | | [66] |
| Ti butoxide, $CaCO_3$, citric acid, ethylene glycol, resin annealing for 4 h at 350° C and for 2 h at 700° | Orthorhombic phase, crystallite size 27 nm, BET surface area 34.6 $m^2/g$, average pore diameter 4.5 nm, $pH_{ZPC}$ 10.1, band gap 3.44 eV | UV photocatalyst for bleaching of MB dye and photo-degradation of pollutants in textile- and tannery wastewater | [67] |
| Ti isopropoxide, $CaCO_3$, anhydrous citric acid, ethylene glycol; resin annealing for 4 h at 350° C, further heated for 2 h at 400–600° C and irradiated by microwaves | Orthorhombic phase, microwave oven processed powders show higher structural organization than those processed in conventional furnace | Effect of micro waves on structural and photoluminescent behavior of CT powders | [68] |
| Ti isopropoxide, hydrated Ca nitrate, HCl, $H_2O$, hydroxypropyl cellulose; gel drying at room temperature, annealing at 400–800° C | Agglomerated mesoporous particles, crystallite size 3.5 nm, surface area 51-21 $m^2/g$ | | [69] |
| Ti butoxide, Ca nitrate, citric acid, EDTA, in EtOH/acetic acid, cotton, D311 resin or sorghum straw as bio-templates; annealing at 750, 900° C | Porous micron entities - broken microtubules with irregular hollows and holes on the walls or porous microspheres; crystallite size 32–37 nm, BET surface area ~65 $m^2/g$, mean pore diameter ~ 9 nm | Adsorber of aqueous heavy (Cd, Pb, Ni, Zn) metals and photocatalyst of UV photolytic degradation of MB dye | [71–73] |
| Ti butoxide, Ca nitrate, acetic acid, PVP, EtOH, $H_2O$; solvent evaporation at 60° C, 5 h calcination at 700° C | Crystalline rod-like ~ 2 mm long and ~100 nm thick particles, band gap 3.08 eV | Photocatalyst of degradation of aqueous MO dye | [74] |
| Ti isopropoxide, hydrated Ca nitrate, ethylene glycol; solution aging for 48 h at 80° C, calcination at 100–300° C and annealing (crystallization) to 700–850° C, planetary milling | Porous μm-sized particles with surface area 10.6, 19.7 and 21.2 $m^2/g$ convert by milling to agglomerated sub-μm bodies composed of 50–60 nm-sized particles | | [75] |
| Ti butoxide, $H_2O$, $HNO_3$, hydrated Ca nitrate, EDTA or carboxylic acid, acryl amide, glucose; gelation at 70° C, drying at 120° C, calcination at 600° C | Spherical particles, average size 25–55 nm, band gap ~3.6 eV, BET surface area 26–62 $m^2/g$, | Photocatalyst in UV photolytic degradation of aqueous MO dye | [77] |
| Ti butoxide, $H_2O$, $HNO_3$, hydrated Ca nitrate, tartaric acid, glucose, acryl amide; gelation at 70° C, calcification at 600° C | Spherical particles, average size 136 nm, surface area 42.7 $m^2/g$, band gap 3.62 eV | Stable and efficient catalyst for degradation of MO, MB and RhB dyes in water by ultrasonic radiation | [78] |
| Ti butoxide, hydrated Ca nitrate, citric acid, in EtOH; PVP, Pluronic, dimethylformamide; nozzle electrospinning, 12 h drying at 80° C, 2 h calcination at 600–800° C | Orthorhombic, nanotubes with outer diameter 105–230 nm and inner diameter 70 nm | Platform for sustained drug loading and delivery | [79] |

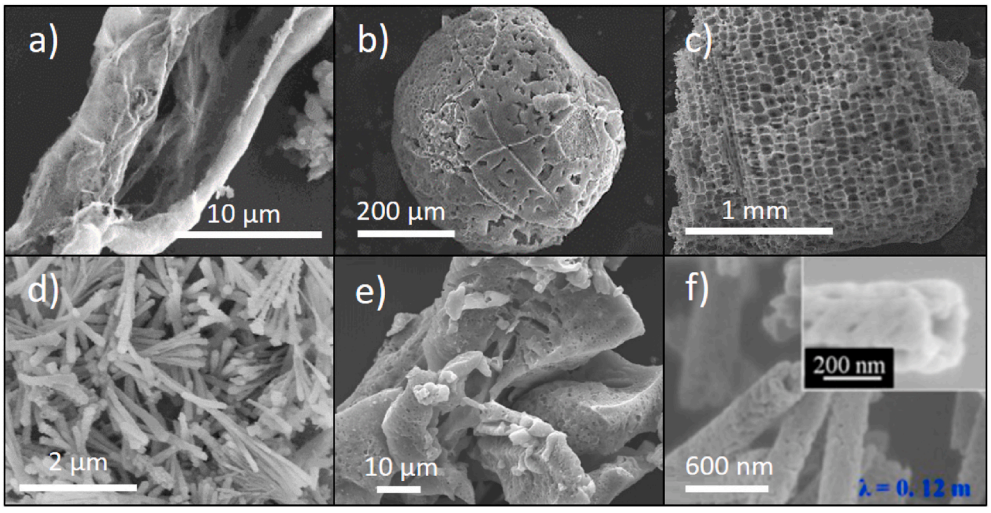


**Fig. 9.** SEM images of broken microtubules (a, reproduced from ref. 71, Copyright Elsevier), nano/micro porous microspheres (b, reproduced from ref. 72, Copyright Elsevier), microporous network (c, reproduced from ref. 73, Copyright Elsevier), nano/micro rods (d, reproduced from ref. 74, Copyright Int. J. Electrochem. Sci.), nanoporous bodies (e, reproduced from ref. 75, Copyright J. Ceram. Proc. Res.) and uniform hollow nanofibers with porous structure (f, reproduced from ref. 79, Copyright Elsevier).

annealed $CaCO_3$–$TiO_2$ mixtures which afforded purer, finer and non-agglomerated CT particles than the heated but non-activated mixtures. It was deduced that smaller and almost uniform spherically shaped particles produced through the combined activation and heating procedures promote further sintering due to higher reactivity of particles generated by milling [38].

### 2.1.3. Lower temperature processes

The noted disadvantage of the use of very high temperatures to achieve CT synthesis from solid CaO, $CaCO_3$ and $TiO_2$ precursors can be removed by choosing different Ca compounds and addition of a mineralization agent (Table 4).

Annealing of hydrated calcium nitrate $Ca(NO_3)_2{\cdot}4H_2O$ with $TiO_2$ nanocrystals at 600 °C represents a low-temperature synthesis of CT, in which $TiO_2$ nanoparticles become immersed during the initial temperature rise in liquid phase of dehydrating $Ca(NO_3)_2{\cdot}4H_2O$ and melting $Ca(NO_3)_2$ [39,40]. The reaction between both reactants at the developing liquid-solid interphase is therefore more facile than the reactions of $TiO_2$ with CaO or $CaCO_3$, which require temperatures above 900 °C.

Also CT synthesis by heating of $TiO_2$ fine particles in excess of calcium chloride bihydrate $CaCl_2.2H_2O$ at above 800 °C [41] is achieved at lower temperature, which is likely due to supposed transient formation of CaO [42] or easier released Ca ions from initially dehydrating and subsequently melting $CaCl_2$ in the developing liquid $CaCl_2$-solid $TiO_2$

**Table 9**
Surfactant and polymer free hydrothermal method.

| Synthetic conditions | CT particles properties | CT particles application | Ref. |
|---|---|---|---|
| Ti butoxide, hydrated Ca nitrate, $H_2O$, NaOH, Teflon vessel, 24 h heating at 200 °C; 12 h drying at 80° C | Orthorhombic, irregularly shaped 0.1–5 μm spongy particles, Scherrer crystallite size 44 nm, surface area 18 $m^2$/g, band gap 3.49 eV | Photocatalyst of UV–vis light degradation of MB dye | [62] |
| Ti tetrachloride $TiCl_4$, calcium chloride dihydrate $CaCl_2.2H_2O$,$H_2O$, KOH, Teflon vessel, 3 h heating at 250° C; 4 h drying at 60° C | Orthorhombic, porous 2 μm long hollow square prisms with 100 nm wall thickness and internal cavity diameter 120 nm, band gap 3.63 eV | | [81] |
| Ti plates, NaOH, Ca $(OH)_2$, Teflon autoclave,24 h annealing at 130° C | 10 μm wide 3-D lamellate structures composed of interconnected 100–200 nm thick petals | Superhydrophilic to superhydrophobic surface transition upon coating with vinyl-terminated polydimethylsilicone | [82] |
| Titanate $H_2Ti_nO_{2n+1}.xH_2O$ nanowires on Ti foil, NaOH, $H_2O$, $CaCl_2$, Teflon vessel, 24 h heating at 200° C | 1–3 μm long and 1 μm thick microtubes | High dielectric constant, non-ferroelectric nature | [83] |
| Ti butoxide, $CaCl_2.2H_2O$, NaOH, $H_2O$, EtOH; autoclave, 36 h heating at 260, 280 and 300° C, 12 h drying at 90° C | Micrometer-sized butterfly-like dendrites | | [84] |
| Ti butoxide, $CaCl_2.2H_2O$, NaOH, $H_2O$, EtOH; Teflon flask, 24–36 h heating at 180 °C,12 h drying at 90° C | Micron sized dendrites and various (cross-cubic, prism-like, butterfly-like) morphologies of composed nanoflakes, crystalline size 93–153 nm | Dendrites of vertically aligned nanoflakes exert UV light trapping effect (multiple reflections and scattering); photocatalyst of UV light degradation of MO, RhB and MO dyes | [85] |
| Anatase, $CaCl_2.2H_2O$, NaOH, $H_2O$, Teflon-lined digestion bomb; 12–96 h heating at 110–150° and different pH (9–13) for 12–72 h, 12 h drying at 90° C | 120–130 nm thick nanowires grown from intermediary twinned 2–3 μm sized crystals with cubic and rectangular shape | | [86] |
| Ti isopropoxide Ti $(OC_3H_7)_4$,$Ca(OH)_2$, NaOH, $H_2O$, Teflon flask, 24 h heating/ controlled stirring at 120° C | Orthorhombic μm-sized dendrites and rectangular prisms; process optimized for massive formation of dendrites | | [87] |
| Titanate nanofibers, $CaCl_2$, $H_2O$, NaOH, PTFE-lined autoclave, 24 h heating at 150 °C, 24 h drying at 100 °C | Microtubular structures with rectangular cross-section | Photoeletrochemical response of dye-sensitized solar cell | [88] |
| Hydrated $TiO_2$, CaO, $H_2O$, PTFE lined vessel,2 h heating at 250° C | Rectangular platelets of 0.5–1.5 μm length | | [89] |
| Pretreated eggshell powder, $H_2O$, $TiO_2$, PTFE bottle in autoclave, 48 h heating at 180° C, 12 h drying at 80° C | Orthorhombic, cuboid-like structure, size 0.2 μm, surface area 20.9 $m^2$/g, | Adsorber of Congo red dye | [90] |
| $TiCl_4$ and $Ti(OR)_4$ with R = Bu, iPr were precursors for $TiO(OH)_2$ hydrogel, KOH, hydrated Ca nitrate; teflon-lined autoclave, 12 h heating at 180° C drying at 60° C | Orthorhombic, crystallite size ~60 nm, CT cuboids with side length less than 1 μm or 2 μm and fern-like nanoparticles, BET surface area 28, 85 and 108 $m^2$/g | Fern-like nanoparticles exhibit excellent photocatalytic activity for As(III) removal in aqueous solution under UV-254 nm irradiation | [91] |
| $TiO(OH)_2$, $CaCl_2$, $H_2O$, KOH, autoclave, heating by microwaves for 1 min and additional heating at 140° C under pressure for 10–160 min, 12 h drying at 80° C | Polycrystalline, orthorhombic phase, micro-cubes with edge length ~2 μm, | Photoluminescence due to the tilt of $TiO_6$–$TiO_6$ adjacent octahedra | [92] |
| $TiCl_4$ or Ti isopropoxide, KOH, $CaCl_2$, $H_2O$, autoclave, 4 min microwave heating at 140 °C,12 h drying at 60° C | Orthorhombic, polycrystalline, microcubes produced by self-organization of nanoplates; Different local order around Ti in CT structures obtained by different Ti sources | UV-light induced visible photoluminescence | [93] |
| Ti isopropoxide-triethanolamine complex or nanoparticulate $TiO_2$ aqueous dispersion, Ca isopropoxide, $H_2O$, 72 h heating in Teflon vessel for 100–250 °C | Cubic, concave cubic and rod-like cubic particles with respective surface area 3.2, 3.1 and 9.7 $m_2$/g; band gap 3. 6 eV | UV photocatalytic decomposition of acetic acid in water | [94] |
| Ti isopropoxide, Ca nitrate, NaOH, $H_2O$, ionic liquid; ultrasound irradiation, 80 h drying, 5 h calcination at 700° C | Orthorhombic, porous ~ 20 nm spheres, crystallite size 8.8 nm, surface area 147.3 $m^2$/g, band gap 3.2 eV | UV–Vis photocatalyst for MB dye degradation and water cleavage | [95] |
| P25 $TiO_2$ powder, $CaCl_2$, NaOH,24 h heating in Teflon-lined vessel at 200° C, 12 h drying at 60° C | Orthorhombic, CT nanocuboids of 0.3–0.5 μm width and 0.8–1.1 μm length, BET surface 4.9 $m^2$/g, absorption edge 367.4 nm, band gap 3.38 eV | Solar light photocatalyst for degradation of RhB dye, Photoluminescent monitoring of OH radical | [96] |

interface at temperatures around melting point of $CaCl_2$ (772 °C).

Sub-micrometer crystallized CT whiskers produced from $CaCl_2$ and $TiO_2$ in the presence of the mineralization agent $(Pb(Ac)_2.3H_2O)$ are developed already at 780 °C. It is presumed that molten $CaCl_2$ salt enhances interaction with solid $TiO_2$ and that generated PbO provides seeds for nucleation of the developing CT whiskers [43].

Another lower-temperature synthesis of CT has been conducted through grinding of the stoichiometric amounts of solid tetra-*n*-butyl

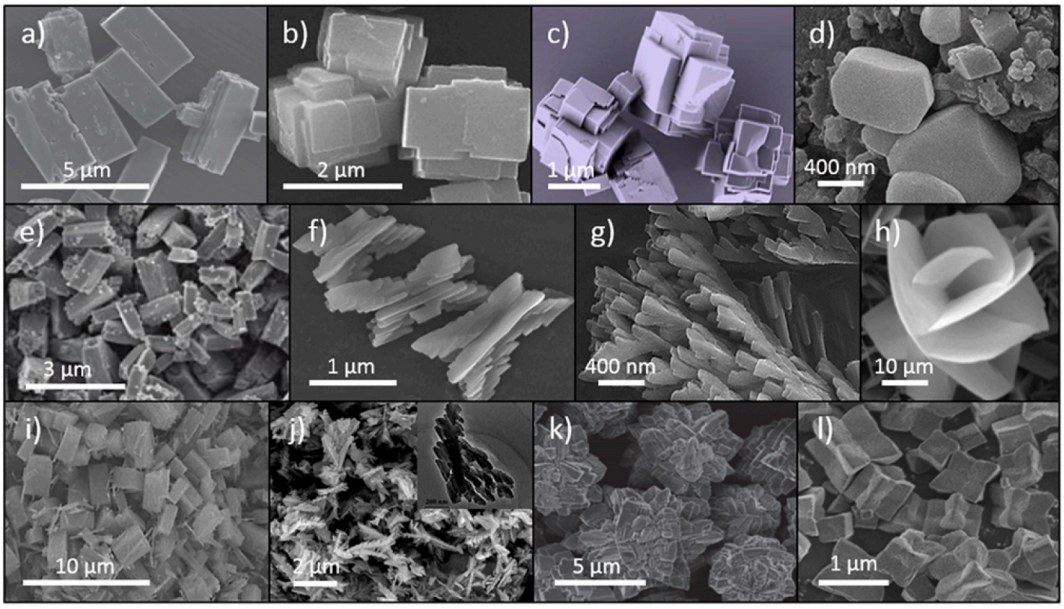


**Fig. 10.** SEM and FESEM images of platelets (a, reproduced from ref. 85, Copyright Ceram. Soc. Jap.), multifaced microcubes (b, reproduced from ref. 92; c, reproduced from ref. 93, both Copyright Elsevier), polyhedral prisms (d, reproduced from ref. 87, Copyright Royal Society of Chemistry), rectangular hollow structures (e, reproduced from ref. 83, Copyright American Chemical Society), butterfly-like dendrites (f, reproduced from ref. 84, Copyright Royal Society of Chemistry), dendrites (g, reproduced from ref. 87, Copyright Royal Society of Chemistry), nanolamellate structures (h, reproduced from ref. 82, Copyright American Chemical Society), microcubes (i, reproduced from ref. 88, Copyright American Chemical Society), fern-like structures (j, reproduced from ref. 91, Copyright Elsevier), cross-cubic shaped morphpology (k, reproduced from ref. 85, Copyright Ceramic Society of Japan), or concave cubic merged particles (l, reproduced from ref. 94, Copyright Royal Society of Chemistry).

**Table 10**
Surfactant and polymer assisted hydrothermal method.

| Synthetic conditions | CT particles properties | CT particles application | Ref. |
|---|---|---|---|
| $CaCl_2$, NaOH, $H_2O$, urea, $TiO_2$ 4 h heating at 180° C by micowaves in Teflon vessel | Orthorhombic phase, 1 µm-sized rectangular prism-like particles | | [97] |
| Ti isopropoxide, EtOH, $CaCl_2$, NaOH, $H_2O$, PEG or CTAB or TSC, 12 h heating in teflon vessel at 120–180° C, 12 h drying at 80 °C | Orthorhombic phase, cuboids of 3.2–4.7 mm length and 1.7–2.3 mm width, point of zero charge 3.8 pH | Efficient adsorber of Cd, Pb and Cu | [98] |
| Reactive $TiO_2$.x $H_2O$ gel, CaO, PVA, 5–8 h heating in Teflon vessel at 150° C | Rectangular platelets 0.1–0.5 µm in length | | [99] |
| Reactive $TiO_2$.x$H_2O$ gel, Ca nitrate, KOH, PVA, 24 h heating in Teflon autoclave at 200° C | Aggregated 1 µm prisms (no PVA) and mesoporous hierarchical 3D networks composed of 80 nm thick nanowires (with PVA); respective surface areas 4.8 $m^2$/g and 26.6 $m^2$/g. Band gap 3.55 eV | Visible light photocatalytic hydrogen production from water induced by 3D network morphology | [100] |

titanate ($Ti(OC_4H_9)_4$) and hydrated calcium nitrate ($Ca(NO_3)_2.4H_2O$) in an agate mortar ensued by heating of a developed semi-solid product at 700 °C [18]. It was shown that the grinding facilitates the hydrolysis of titanate and evaporation of butanol and that the semi-solid product is presumably titanyl nitrate.

The morphology of CT particles obtained by the lower temperature processes depends mostly on the choice of the reactants, and as seen below (Fig. 5), oval and sharp nanoparticles, irregular and faceted µm-sized particles and µm-sized needle-like and large objects can me formed.

### 2.1.4. *Single-source precursor approach*

Another way for decreasing high temperatures required for CT formation from solid precursors is thermal decomposition of a single-source precursor which is stable organobimetallic compound whose structure is tailored to allow thermal conversion into stoichiometry of CT (Table 5).

Such strategy is documented by heating of calcium titanyl oxalate, calcium nitrilotriacetatoperoxotitanate or calcium titanyl citrate [44–48] at temperatures between 500 and 700 °C, which are sufficient for conversion to micro- and nanosized powders of CT (Table 5). The reaction temperature can be even lowered considerably by employing microwaves [45,47]. In fact, conventional heating of calcium titanyl oxalate monitored by TG and DT analyses proceeding at 450–600 °C via an amorphous $Ca_2Ti_2O_5CO_3$ intermediate allows formation of crystalline (pseudo cubic) CT at 570–750 °C [49]. The favorable microwave effect on the pore diameter of mesoporous crystalline CT nanoparticles [47] is possibly due to interactions of microwaves with structural defects (oxygen vacancies and unpaired electrons) of CT. Further example of a single compound decomposing to CT is calcium catecholate complex [50].

A heat-induced topochemical microcrystal conversion of bismuth layer-structured compound $CaBi_4Ti_4O_{15}$ into platelike CT particles [51] in molten salt also belongs to this section. This process conserves the particle shape from an anisotropically shaped precursor to the target compound particle through a topochemical, topotactic and/or pseudomorphic reaction while the chemical composition of the particle is changed.

Different morphologies of several types of CT particles obtained by the single-source precursor approach are illustrated in Fig. 6.

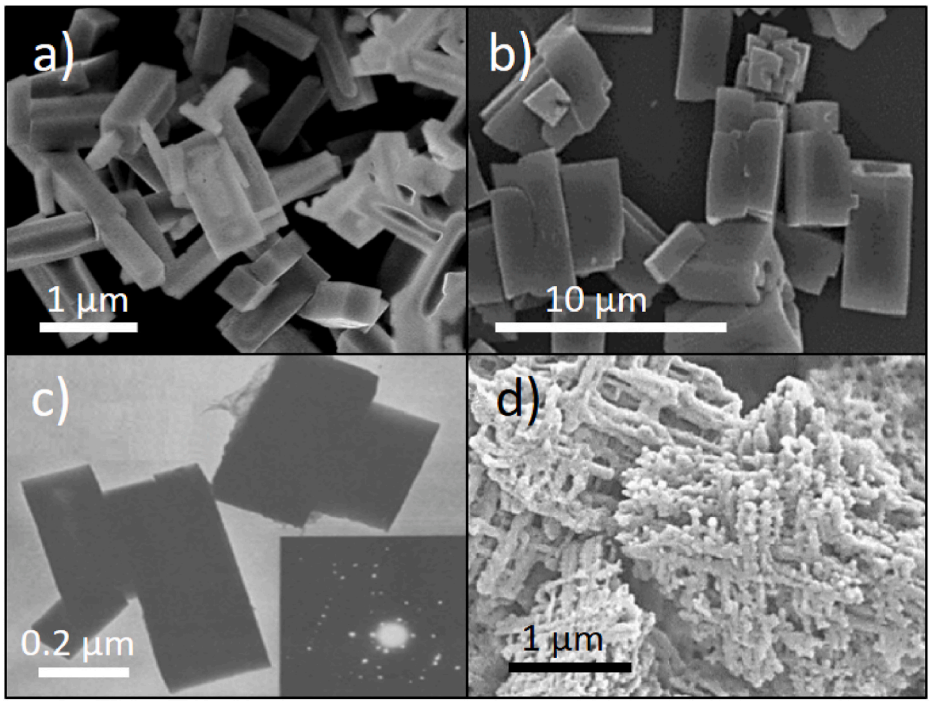


**Fig. 11.** FESEM, SEM and TEM images of cuboids (a, reproduced from ref. 97, Copyright Royal Society of Chemistry, and b reproduced from ref. 98, Copyright Elsevier (b), platelets (c, reproduced from ref. 99, Copyright Elsevier) and porous 3D hierarchical structures (d, reproduced from ref. 100, Copyright Elsevier).

**Table 11**
Solvothermal syntheses.

| Synthetic conditions | CT particles properties | CT particles application | Ref. |
|---|---|---|---|
| Minute amounts of Ti butoxide and aqueous Ca nitrate in excess of PEG solvent, NaOH (mineralizer); 15 h heating at 180° C | Orthorhombic, hollow sub-µm-sized cubes with walls assembled by three-dimensionally twinned and textured nanodomains | Photoluminescence of hollow cubes | [101] |
| Ti butoxide, solid Ca nitrate and NaOH (mineralizer) in excess of PEG solvent; 15 h heating at 180° C | Orthorhombic, spherical shaped 600 nm-sized walnut morphology with hollow interior, shell thickness 200 nm, composed of 40 nm-sized nanocubes | | [102] |
| Ti butoxide, hydrated Ca nitrate, PEG solvent, NaOH, at 180 and 220° C, drying at 60° C under vacuum | Orthorhombic,sub-µm sized particles of different (octahedral, spherical or cubic) morphology depending on water content and NaOH concentration | UV light photocatalyst of degradation of MB dye | [103] |
| Ti isopropoxide $Ti(OC_3H_7)_4$, ethylene glycol or diethylene glycol, $Ca(OH)_2$, $H_2O$; 6 h annealing at 200° C | Orthorhombic, 1–2 µm sized concave cubic-shaped particles, flake-shaped incorporating calcium titanium glycolate | | [104] |
| Ti butoxide, Ca nitrate, NaOH, EtOH–$H_2O$; 12 h heating at 150° C | Tubular and non-tubular 1D, 2D (T-like or cross-like) and 3D microstructures | | [106] |
| Ti butoxide, hydrated $CaCl_2$, NaOH, EtOH–$H_2O$, 24 h heating at 180° C, 12 h drying at 90° C | Smaller loose and 3.4–4 µm-sized dense microspheres composed of nanosheets, surface area 6.06 $m^2/g$, band gap 3.5 eV | UV light photocatalyst of degradation of RhB dye | [107] |
| Ti butoxide, $CaCl_2$, PVP, NaOH, EtOH–$H_2O$, 24 h heating at 140–220° C, 12 h drying at 90° C | µm-sized flower-like, prism-like, nanosheet, dendrite, cross cubic and polyhedron morphologies | Long-term electrochemical stability, UV photocatalyst for RhB dye degradation | [108] |
| Ti butoxide, $CaCl_2$, EtOH, NaOH, $H_2O$, acetylacetone stabilizer; 36 h heating at 180° C, 24 h drying at 180° C; milling 15–35 min | Orthorhombic, 1 µm-sized mesoporous particles (band gap 3.33 eV, surface area 44 $m^2/g$), after milling (band gap 3.17 eV, surface area 27 $m^2/g$) | UV light photocatalyst of degradation of Malachite Green (MG) dye | [109] |

### 2.2. Wet chemistry

The syntheses accomplished in the liquid phase can be classified according to the types of chemical reactions needed to change the Ca and Ti reactants into CT ultrafine product. They are called solution combustion, simple sol-gel approach, sol-gel polymer precursor approach, hydrothermal and solvothermal route and peroxo complex approach.

#### 2.2.1. Solution combustion

Solution combustion is a method early designed for the production of fine-particle ceramic powders by combustion of redox compounds or mixtures and is described as a low-temperature initiated, self-propagating, gas-producing, exothermic reaction yielding sinteractive submicron-sized materials with large surface area [52,53]. Its specific version suitable for fast synthesis of solid CT network [18,54,55] consists of mixing a calcium salt with a titanium precursor in water and an ensuing contact of the resulting solution to high temperatures in a pre-heated furnace (Table 6). The process is completed in few minutes and involves dehydration, decomposition reactions, formation of gases and highly viscous liquids which swell, auto ignite with flames and form voluminous foamy products. The addition of a fuel component (tetra formyl tris-azine, urea or tartaric acid) increases flame temperatures above 900 °C and aids the evolution of larger amounts of gases favorable for the development of CT nanopowders with high specific surface area.

A unique spray-pyrolysis can be also regarded as a mode of solution

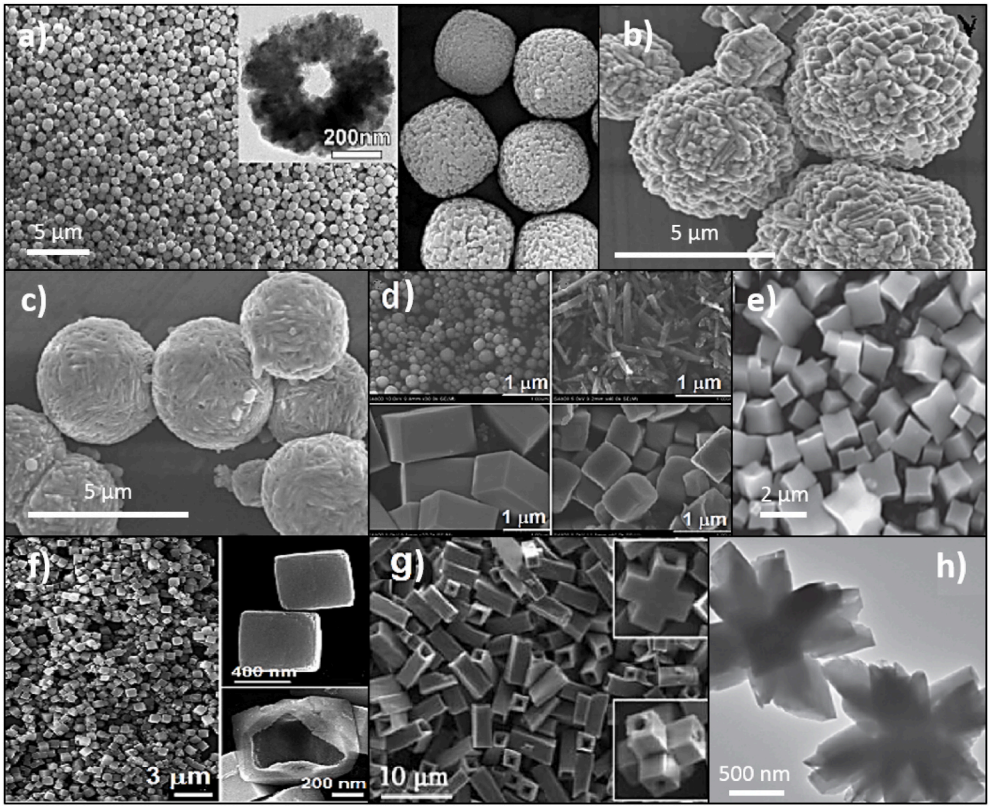


**Fig. 12.** SEM images of walnut-like structures (a, reproduced from ref. 102, Copyright Royal Society of Chemistry), loose (b) and dense (c) spheres (reproduced from ref. 107, Copyright Elsevier), rectangular bars and cubes (d, reproduced from ref. 103, Copyright Royal Society of Chemistry), concave cubes (e, reproduced from ref. 104, Copyright Jap. Inst. Metals Mater.), mesocubes with flat surface or hollow interior (f, reproduced from ref. 101, Copyright Royal Society of Chemistry), 1-, 2- and 3- D tubular particles (g, reproduced from ref. 106, Copyright American Chemical Society) and flower-like crystals (h, reproduced from ref. 108, Copyright Ceramic Society of Japan).

**Table 12**
Peroxo complex approach.

| Synthetic conditions | CT particles properties | CT particles application | Ref. |
|---|---|---|---|
| Hydrated $CaCl_2$, $TiCl_4$, precipitation after mixing with $NH_3$/$H_2O_2$ solution, 1 h calcination at 900° C, mixing with glycerol and PVA binder, milling, drying at 80° C | Surface area 18 $m^2$/g | High sinterability | [114] |
| Hydrated Ca acetate, $TiO(SO_4)$, $H_2O_2$, NaOH, precipitation, 0.5 h heating at 95° C, microwave heating for 3–30 min | Orthorhombic, Scherrer crystallite size 44–49 nm, band gap 2.67–3.08 eV, truncated ~100-30 nm sized nanospheres | UV light photocatalyst of degradation of MB and MG dyes | [115, 116] |

combustion approach and consists of an ultrasonic generation od aerosol from a solution of Ca and Ti sources and subsequent feeding the sols into a flow of $O_2/N_2$ gases at high temperatures provided by furnace. The appearance of µm-sized spherical particles generated in Ref. [56] is controlled by the concentration od precursor solution and the rapid evaporation of solvent from the droplet surface, which can lead to the formation of a salt crust around the particles.

The different procedures classified under the solution combustion approach afford particles of different morphologies as seen in Fig. 7.

### 2.2.2. Simple sol-gel approach

The sol–gel synthesis of a wide range of inorganic materials is based on the hydrolysis and condensation of molecular precursors and involves formation of sols (colloidal particles suspended in a liquid) which participate in a gelation process to finally yield interpenetrating networks of solid and solvent phase. The sol-gel approach to solid CT structure (Table 7) involves reactive mixing the titanium alkoxides with calcium salts in alcohol, reactions with small amounts of water, formation of transparent gels and heating the gels to temperatures which are noticeably lower than those required for CT formation by the solid phase reactions. It was presumed that the gel formation involves intermediary $Ti(O\text{-}iPr)_x(OAc)_z$ molecules [57] that are likely formed via intermolecular redistribution of groups attached to Ti and Ca of the primary reactants. Several sol-gel syntheses were carried out in the presence of citric acid [58,60,62] or hydroxycarboxylic or dicarboxylic acids [61] which assist gel formation as a mild acidifier and chelating agent. Other syntheses were conducted by using acetylacetone inhibiting hydrolysis of Ti alkoxide and a structure-directing surfactant assisting formation of a mesoporous-assembled CT structure [63]. The morphology and size of CT nanoparticles after gel calcination is little influenced by the structure of chelating acid. It is however seen that somewhat different conditions of the simple sol-gel approach result in nanoparticles which strongly agglomerate into bodies with dense or porous structures (Fig. 8).

### 2.2.3. Sol-gel polymer precursor approach

There are several sol-gel-based CT syntheses in which an added polymer precursor is either formed from monomer in the course of sol-gel process or simply added to the solution undergoing sol-gel transition (Scheme 1). Both these organic entities interact with aqueous solutions of Ti complexes produced from soluble Ti and Ca compounds and incorporate them into their polymeric network. Detailed modes of such interaction appear unknown, but following heating and calcination of isolated and dried products in an air or oxygen flow removes organic skeleton by oxidative combustion and leaves inorganic phase of ultrafine CT particles (Table 8).

A well known sol-gel polymeric precursor approach to nano- and micro-sized CT species is based on the Pechini invention of preparing alkaline earth titanates [64] by utilizing the ability of

**Table 13**
Physical and physicochemical methods.

| Synthetic mode | CT coat properties | CT coat application | Ref. |
|---|---|---|---|
| Radiofrequency magnetron sputtering of CT target in Ar gas followed by annealing of deposited film on Ti in air at 600° C | 50 nm thick film on Ti substrate with a Ti oxides layer underneath | Enhanced formation of calcium phosphate in SBF and improved new bone formation *in vivo* | [117] [118] |
| UHV sputtering for thin film deposition at room temperature on Si substrate and at 550 and 650° C on Pt/TiN electrode | Amorphous 31 nm thick film with rms = 0.19 nm deposited on Si; crystalline 60 nm thick film with rms 0.46 nm deposited on Pt/TiN; 5 and 32 nm thick films on Pt/TiN covered by Ru layer; band gap 3.8–4.38 eV | Promising insulating film in industrial MIM capacitor applications | [119] [120] |
| Pulsed laser deposition from CT target in 100 mTorr of $O_2$ on substrates kept at 750 °C | Highly epitaxial 350 nm films on $SrRuO_3$ layers on $SrTiO_3$ and $LaAlO_3$ substrates with dielectric constant tunable with electric field | Improved tuning of dielectric constant by electric field at −73° C | [121] |
| Pulsed laser deposition from CT target in $5 \times 10^{-5}$ mbar of $O_2$ on $TiO_2$ terminated Nb-doped $SrTiO_3$ substrates kept at 680° C followed by in situ UHV diagnosis | $TiO_2$-terminated film of 20 unit cells thickness has surface metallic states, consisting of a two-dimensional electron gas and plasmons visible as loss XPS peaks | | [122] |
| Q-switch pulsed Nd:YAG laser (335 nm) ablative CT deposition at low $O_2$ pressure on Ti substrate kept at 600° C | Thin film with interposed 40 nm rutile layer | | [123] |
| Pulsed laser deposition on orthorhombic (101)-oriented $NdGaO_3$ and cubic (001)-oriented $La_{0.18}Sr_{0.82}Al_{0.65}Ta_{0.35}O_3$ substrates kept at 650° C | ~10 nm thick films epitaxial grown on both substrates experience a 1.1% biaxial strain and display ferroelectric properties below Curie temperature 140 K | Key role of symmetry in controlling ferroelectric properties of perovskite oxide thin films | [124] |
| MBE of thin films with Ti/Ca ~1 stoichiometry using elemental Ca and Ti isopropoxide co-supplied with molecular $O_2$, allowing deposition within self-regulated adsorption-controlled growth window on (001) $(LaAlO_3)_{0.3}(SrAl_{0.5}Ta_{0.5}O_3)_{0.7}$ substrate heated at 900° C | ~20 nm thick films grown inside the stoichiometric growth window have tensile strain-induced ferroelectric properties and transform at 175 K to paraelectric form | Stoichiometric control is a mandatory requirement to achieve strain-induced functional properties | [125] |
| MBE of thin films with Ti/Ca ~1 stoichiometry using elemental Ca and Ti isopropoxide co-supplied with molecular $O_2$, allowing deposition within self-regulated adsorption-controlled growth window on (001)$LaSrAlO_4$ or $LaAlO_3$ substrate heated at 900° C | 14 nm thick films grown inside the stoichiometric growth window have compressive strain-induced ferroelectric properties lasting from room temperature up to 800 K | Ferroelectric thin film | [126] |
| CVD from vaporized Ca and Ti sources - (bisdipivaloylmethanato-calcium) and bisisopropoxy-bis-dipivaloylmethanato-titanium) in Ar and $O_2$ on fused quartz glass plates heated at 600–800° C | Film morphology changes from dense structure/grain size 50 nm to cauliflower columnar texture/grain size 2–3 μm upon increasing $O_2$ pressure and substrate temperature | Biomimetic hydroxyapatite deposition from Hanks' solution, enhancement of differentiation of mouse bone marrow stromal ST-2 cells | [127] [128] [129] |
| Laser induced CVD from vaporized (bisdipivaloylmethanato-calcium) and bisisopropoxy-bis-dipivaloylmethanato-titanium) and $O_2$ on AlN substrate heated at 327–727° C | Highly (011)- and (101)- and (121)-oriented CT films with cone-like morphology or squarely faceted texture and the nano-pores | Inducer of apatite formation from SBF | [130] [131] |

alpha-hydroxycarboxylic acids to form complexes with titanium and subsequently undergo heat-induced polyesterification [65] upon addition of polyhydroxy alcohol to form solid transparent polymeric resin containing homogeneously distributed non-seggregated Ti complexes. Further calcination of such hetero-polymeric resin in an oxygen flow then promotes pre-pyrolysis and total oxidation of the organic matter, which transforms the resin into ultrafine CT particles. In this approach, Ti alkoxides (butoxide or isopropoxide) and citric acid are precursors for the formation of a Ti complex, which reacts with Ca nitrate or carbonate in the course of polyesterification, but timing of distinct reaction steps in procedures [66–68] can be somewhat different. The crystalline phase formation in these processes can be probed by photoluminescence to monitor structural order-disorder in CT lattice [68].

A modified reaction scheme was applied in the process [69] using hydroxylpropyl cellulose as a polymeric fugitive agent where the first step consists in the preparation of $TiO_2$ sol by hydrolysis of Ti alkoxide through the optimized methodology [70] and uses HCl as peptization catalyst and the second step is an addition of a solution of calcium nitrate into $TiO_2$ sol. Similar approach involving sacrificing agent is CT synthesis using cotton fiber template [71], D311 poly (methylacrylate-divinylbenzene) resin [72], sorghum straw [73] or polyvinylpyrrolidone (PVP) [74].

Another approach enabling to prepare processable polymeric precursor with the same type chemicals, but in the absence of citric acid and water, is called steric entrapment of cations by ethylene glycol polymer [75]. In this process, solutions of reactants form gels upon long aging and such gels undergo an explosive exothermic reaction during the calcination process. The mechanism of the gel formation thus differs from the Pechini gelation and may be mostly controlled by

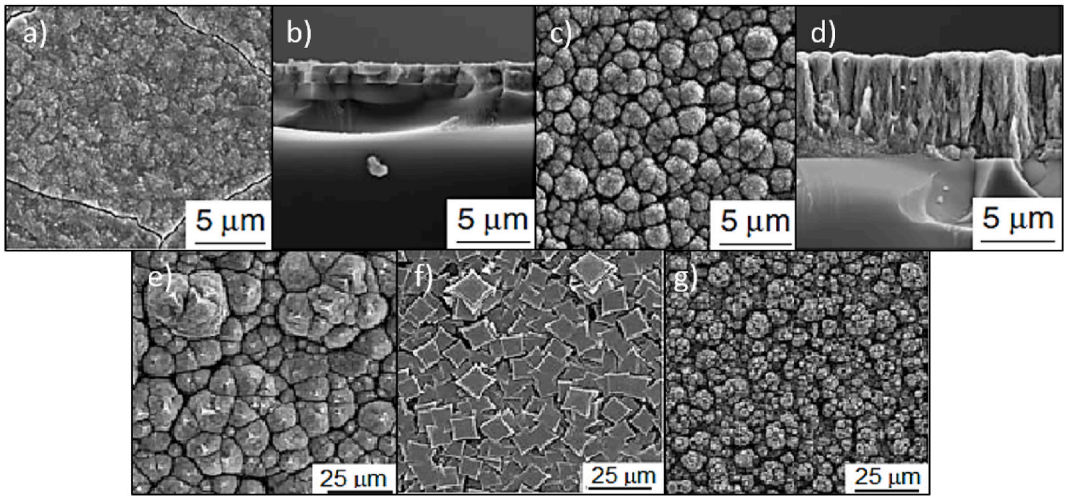


**Fig. 13.** Surface and cross-sectional morphology of CT films prepared at 600 °C (a, b) and 800 °C (c, d) by MOCVD (reproduced from ref. 127, Copyright Jap. Inst. Metals and ref. 128, Copyright Trans. Tech. Publ.) and surface morphology of (011)-oriented films with pyramidal facets (e), (101)-oriented films with square facets (f) and (121)-oriented films with granular morphology prepared by laser MOCVD (g), reproduced from ref. 130, Copyright J. Jap. Soc. Powder Metal., and ref. 131, Copyright Springer).

intermolecular exchange of oxidic groups between Ti isopropoxide and ethylene glycol (exchange reaction between –OH and i-PrO- groups), while the explosive stage should involve radical reactions.

CT nanoparticles were also prepared by a polyacrylamide gel route which is accomplished by developing a uniform distribution of intermediate organobimetallic species in growing polyacrylamide network [76]. It is based on gelation of acidified aqueous solution of Ti alkoxide, Ca nitrate, a chelating agent (ethylenediaminotetraacetic or other carboxylic acids), and acryl amide [77,78]. Adding glucose to the precursor solution overcomes gel shrinkage and using different structures of chelating acids allows calcined CT particles to get different size.

Porous CT nanotubes with controlled microstructure were prepared via a single-nozzle electrospinning approach when CT sols comprising PVP and a Pluronic polyoxypropylenepolyoxyethylene block copolymer initially changes to core-shell structure and after drying and calcination in air develop to CT nanotube whose structure can be tailored by the ratios of sol components [79].

This approach offers a number of CT particles with different morphologies like broken microtubes, hollow nanofibers, porous networks and porous particles, rods or porous spheres (Fig. 9).

### 2.2.4. *Hydrothermal route*

The hydrothermal route involving the use of Teflon-lined high-pressure vessels is a less cost and reaction time demanding process which allows formation of CT particles at lower temperatures (Table 9) due to facilitating intimate contact between Ca and Ti reactants in alkaline aqueous phase and offeres chances to produce CT particles of various sizes and morphologies (Fig. 10). The process consists of dissolution of Ca and often also Ti reactants, formation of a hydroxylated $CaTi(OH)_x$ precursor, the precursor dehydration and CT nucleation and growth. The final CT product can be developed through heterogeneous path by inward diffusion of dissolved $Ca^{2+}$ ions into solid $TiO_2$ or through homogeneous path by liquid phase reaction between soluble $[Ti(OH)_6]^{2-}$ complex and $Ca^{2+}$ species.

A thermodynamic model of hydrothermal synthesis of $CaTiO_3$ predicted the optimum conditions for the synthesis of phase-pure $CaTiO_3$ from some Ca and Ti sources within temperature range 160–200° [80] and indicated that hydrothermal system is controlled by kinetic inhibition of CT formation by little soluble $Ca(OH)_2$, which governs the transport of Ca species to an interface bearing reactive Ti species, proper stirring under nitrogen (exclusion of $CO_2$), the correct pH chosen by amounts of Ca source and NaOH/KOH mineralizer and larger sizes of Ti source particles.

Various smooth and porous nanoparticles produced under various conditions can accept morphology of nanowires, nanocubes, nanotubes, platelets or fern-like dendritic structures. The nanoparticle growth and self-organization of building blocks is often explained by Ostwald ripening process in which larger particles are formed at expense of more reactive smaller particles. For example, the fabrication of microtubular CT undergoes the initial dissolution of titanate nanofibers by Ostwald ripening process to convert into micrometer-sized fiber-bundles, while recrystallization occurs simultaneously until tubular microstrucures are obtained [88]. Dendrites usually form under non-equilibrium conditions and their growth is controlled by interface kinetics, surface tension and concentrations gradients all of which may result in a discrepancy in the growth velocity of two (metastable and stable) crystallographic planes.

It was also shown that microwave processing enhances evolution of CT crystalline phase whose structure can differ with two different Ti sources, as demonstrated by different degree of distortion of local Ti symmetry and indicated by different photoluminescence spectra [93]. Low temperature hydrothermal process was also performed by using ultrasound irradiation in the presence of ionic liquid at ambient pressure [95]. The growth of differently sized and shaped CT nano- and micro-sized particles can thus be achieved through changes in the composition of the liquid medium and its alkalinity, different lengths of hydrothermal treatment, different stirring rates and also using different Ti and Ca sources and their ratios.

All these hydrothermal media can thus noticeably control the size and morphology of generated CT nanoparticles through vapour pressure and solubility of the Ca and Ti compounds in water. Their potential can, however, be further enhanced by using surfactant or template agents which can assist shaping process of the growing CT seeds (Table 10). Urea can act as a template or form a structural precursor complex in the formation of rectangular CT prisms [97], polyethylene glycol (PEG) and cetyltrimethyl ammonium bromide (CTAB) or trisodium citrate (TSC) effect formation of smaller irregular particles and larger cuboids [98], an addition of polyvinyl alcohol (PVA) to the hydrothermal solution leads to the formation of smaller CT particles [99], and polyvinyl alcohol (PVA) serves as a structure directing agent to form network-like hierarchical structures built from crystalline nanowires which can promote the photocatalytic performance [100]. Various structures of CT nanoparticles produced by the surfactant and polymer assisted hydrothermal approach are given in Fig. 11.

**Table 14**
Hydrothermal formation of CT Films.

| Synthetic conditions | CT coat properties | CT coat application | Ref. |
|---|---|---|---|
| 6 h heating of Ti plate with Ca $(EDTA)^{2-}$ solution at pH at 250 °C | 20 μm thick film of 1 μm-sized hexagonal plate-like particles | | [132] |
| 1 h heating of Ti plate with $Ca(OH)_2$ in water at 6.3 MPa and 280° C | Rough structured surface | Enhancement of hydroxyapatite formation from SBF as compared to titanium surface | [133] |
| Dipping of preformed nanoporous $TiO_2$ film of 20 nm-sized particles on F-doped $SnO_2$ (FTO)-coated glass in aqueous $CaCl_2/TiCl_4$ solution at 70° C, sintering in air at 750° C | Cubic phase, smooth layer on nanoporous $TiO_2$ film | N3 sensitized CT-modified $TiO_2$ nanocrystalline electrode with enhanced visible light absorption; the dye-sensitized solar cell of enhanced photocurrent and photoelectric conversion efficiency | [134] |
| 24 h heating of Ti plate or rod with KOH–$CaCl_2$ solution at 150° C | Layer of low adhesion to Ti surface, stepped morphology, 1 or ~10 μm euhedral cubic particles in a close mutual contact | Precursor for fabrication of CT/hydroxyapatite double layer | [135] |
| $HNO_3/H_2O_2$ pretreated Ti screws, aqueous solution of Ca nitrate and NaOH, 4 h heating at 110° C | Dense layer of uniform ca. 1 μm sized cubic particles | CT-coated titanium screws increased alkaline phosphatase activity and proliferation of MC3T3-E1 cells | [136] |
| 24 h heating at 180° C of μm-sized flower-like $TiO_2$ on FTO substrates in Ca acetate solution | Band gap 3.24 eV | UV light photocatalyst of degradation of MB dye | [137] |
| Titania anodic films of ordered $TiO_2$ nanotubes preformed in glycerol- $NH_4F$ solution on Ti foil, 12 h heating in saturated $Ca(OH)_2$ solution at 120 °C, annealing to 450° C | Highly ordered vertically aligned $CaTiO_3$ nanotube array, band gap 3.4 eV | Excellent optical absorption ability and higher photovoltage and photocurrent compared with $TiO_2$ nanotube, an alternative choice for $TiO_2$ nanotube photoanode | [138] |
| Titania anodic films of ordered $TiO_2$ nanotubes preformed in glycerol–$H_2O$–$NH_4F$ solution on Ti foil, 12 h heating in saturated $Ca(OH)_2$ solution at 150 °C | Crystalline nanobricks as cube-like structures with 45–75 nm short and 125–275 nm long edges | Efficient hydroxyapatite inducer from simulated body fluid | [139] |
| Titania anodic films preformed in ethylene glycol–$H_2O$–$NH_4F$ solution on Ti foil, 5 h heating in NaOH–$Ca(OH)_2$ solution at 150 °C | Orthorhombic phase with regular micrometer-sized elliptic, flower or prism shaped morphologies | High capability to induce nucleation and growth of biomimetic apatite from SBF | [140] |
| Electrochemical treatment of TiAl anode with Ca $(OH)_2$–NaOH–$H_2O$ at 200° C and 2 MPa | 4–5 μm thick films of 1 μm grains with seldom $TiO_2$ voids | Improvement of oxidation resistance of TiAl alloys at high temperatures | [141] |
| Electrochemical treatment of Ti anode with Ca $(OH)_2$–NaOH–$H_2O$ at 200° C and 2 MPa | Orhorhombic phase, 200–300 nm thick film with dominant microplatelet regions growing parallel to Ti surface with minor microstar-like $CaCO_3$ and 100 nm pinholes | Inducer of Ca apatite formation from SBF | [142] [143] |
| $Na_{0.8}H_{1.2}Ti_3O_7$ micro-sheets (obtained by hydrothermal reaction of Ti with NaOH solution) were modified by ion exchange to $H_2Ti_3O_7$ micro-sheets then hydrothermally treated to CT microsheets scaffold in saturated $Ca(OH)_2$ solution at 180 °C | Osteoconductive scaffold, thickness of the microsheets on Ti foil ~3.5 μm | Promoter of MC3T3-E1 cells spreading, proliferation, and differentiation *in vitro,* enhancement of osteoinductivity *in vivo* | [144] |

### 2.2.5. Solvothermal route

Heating of Ca and Ti source precursors in an excess of alcohol instead of water is another way to produce micro/nano CT particles. Such a procedure in Teflon-lined vessels can yield CT particles which differ from those obtained by the hydrothermal approach due to involvement of liquid phase which contains only minute amounts of water needed for dissolution Ca salts and which can modify the morphology of CT growth as a shape-controlling mediator through interfacial interactions (Table 11).

Hollow sub-micrometer sized CT cubes with twinned and textured orthorhombic (pseudocubic) nanodomains in three dimensions have been grown in excess of poly(ethylene glycol) (PEG) containing minute amounts of aqueous Ca nitrate. The PEG molecules appear to enable the growth of these species, which is not possible when PEG is stepwise diluted with water in which case prismatic single crystal rectangular rods, aligned stacks of rectangular nano-plates or butterfly shaped crystals are formed instead [101]. In a completely water-free PEG solution [102], CT nanocubes form and undergo an oriented self-assembly into spherical particles, which is enhanced by the surface-adsorbed PEG molecules. The growth of nanocubes and their aggregation occurs simultaneously and competes with the disappearance of the small nanocubes in the cores of the spheres during an Ostwald ripening process. Water plays an important role in recrystallization that extends from the particle surface to the cores via an Ostwald ripening process. Similar morphologies were also observed in water-free PEG where spherical particles piled up with nanocubes, octahedral or cubic particles with voids on surface or rectangular particles were produced at different temperature within 280-220 °C and where smaller particles with rounder and smoother surface were formed upon addition of water [103]. CT microparticles can be also formed in water/polyol solutions by heating Ca a source compound with stable Ti complex with triethanolamine [104].

Another solvothermal medium are mixtures of water with amphiphilic ethanol which can act as a versatile soft template, kinetically control the growth rates of different crystalline faces and morphology of final products through ethanol/water ratios [105]. In such medium, various tubular and non-tubular microstructures were prepared and they consist of 1D, 2D T-like or cross-like, and 3D entites whose structure can be tuned by NaOH concentration and ethanol/water ratio [106]. Further examples are loose and dense microspheres piled up with nanosheets [107] or μm-sized flower-like, prism-like, dendrite, cross cubic polyhedron and nanosheet morphologies [108]. The latter crystalline forms were produced with and without PVP which adsorbs onto different crystal phases via ligand coordination and may govern the growth of particles.

The combination of solvothermal and subsequent mechanochemical routes confirmed that the initially produced mesoporous μm-particles decrease their band gap and surface area but enhance their photocatalytical efficiency for dye degradation after milling [109]. The

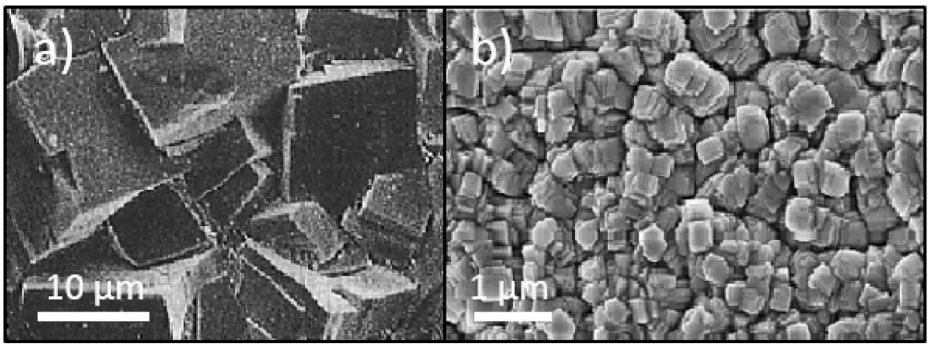


**Fig. 14.** SEM images of CT layers consisting of euhedral cubes (a, reproduced from ref. 135, Copyright J. Ceram. Soc. Jap.) and cubic microparticles (b, reproduced from ref. 136, Copyright Royal Society of Chemistry).

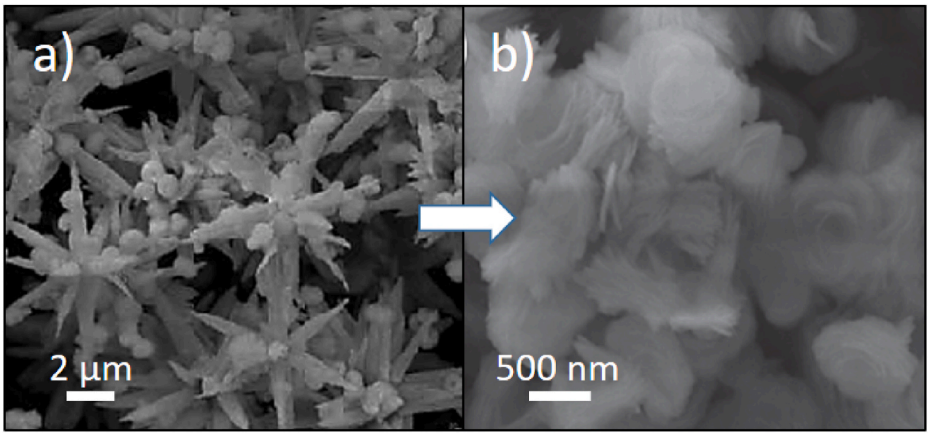


**Fig. 15.** Hydrothermal CT transformation from micro-flower to micro-nest morphology. Reproduced from ref. 137, Copyright Royal Society of Chemistry.

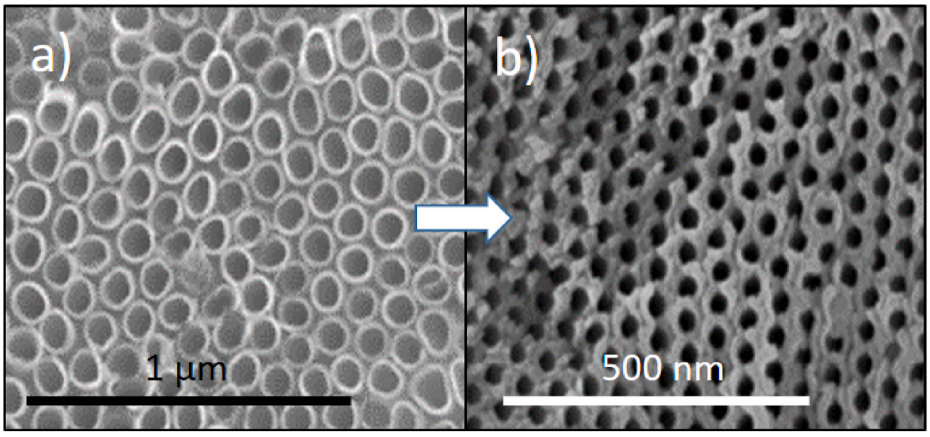


**Fig. 16.** Hydrotherrmal transformation of highly ordered $TiO_2$ nanotubes to topmost CT nanotubes. Reproduced from ref. 138, Copyright IOP Science.

variety of the differently shaped and structured particles is illustrated on Fig. 12.

*2.2.6. Peroxo complex approach*

Another synthesis of high-purity $CaTiO_3$ is called wet chemical peroxide route [110,111] which occurs via the precipitation of a peroxo $CaTiO_2(O_2).3H_2O$ precursor prepared from $CaC1_2$, $TiC1_4$ (or tetraisopropoxide), $H_2O_2$ and $NH_3$ as starting compounds [112–114] and subsequent complex decomposition by heating. The peroxo complex can be also prepared from titanylsulfate and transformed into CT powder by short microwave irradiation [115,116]. These routes are given in Table 12.

## 3. Nano and micro $CaTiO_3$ coats

Fabrication of thin CT coats on various surfaces can be achieved through processing of solid or vaporized Ca and Ti source precursors by physical methods like magnetron sputtering and laser ablative deposition, by physicochemical molecular like beam epitaxy and chemical vapour deposition, or can be also accomplished by using wet chemistry as hydrothermal or sol-gel routes. All these processes allow formation of variously structured coats which differ by distinctive phases, micro/nano morphologies, thickness and properties important in applied and fundamental research.

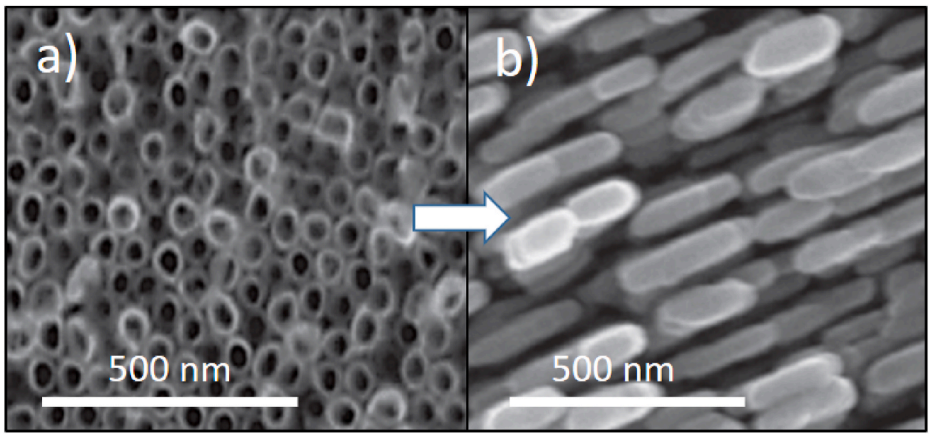


**Fig. 17.** Hydrothermal transformation of highly ordered $TiO_2$ nanotubes to topmost CT nanobricks. Reproduced from ref. 139, Copyright Elsevier.

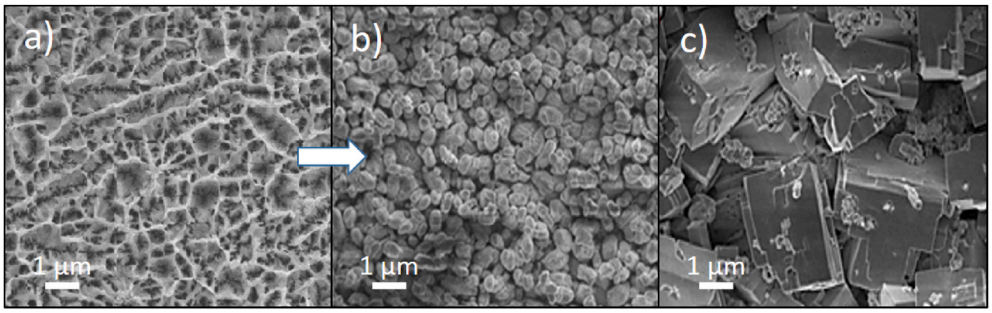


**Fig. 18.** Hydrothermal transformation of nanoporous $TiO_2$ surface (a) to eliptic (b) and prism-like (c) topmost microstructures by 1 M (b) and 4 M (c) concentrations of NaOH. Reproduced from ref. 140, Copyright Elsevier.

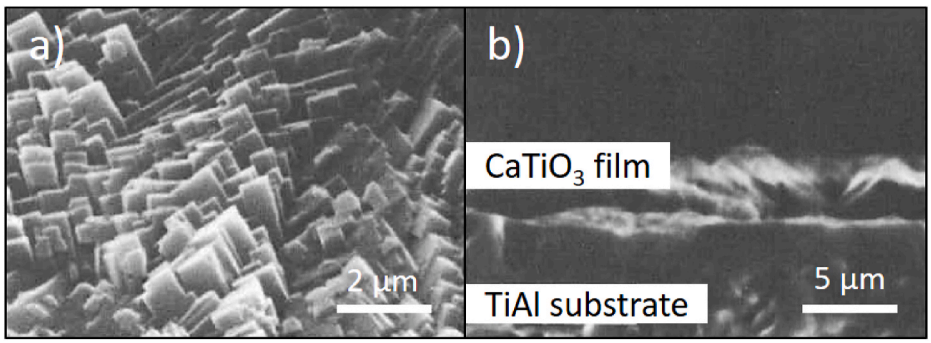


**Fig. 19.** The outer surface layer (a) and fractured cross section (b) of CT coat on TiAl alloy. Reproduced from ref. 141, Copyright Elsevier.

### *3.1. Physical and physicochemical methods*

The deposition of thin CT films by magnetron sputtering of a CT disc in flowing Ar gas normally yields films of low crystallinity and an additional heating is needed to increase the crystallinity and prevent film dissolution in aqueous solutions, which is important for subsequent studies. It is considered that Ca dissolution of topmost layers is due to their chemical instability and would deteriorate the recognition of proceses occurring on the liquid phase-CT interface, like formation of Ca phosphate in simulated body fluids [117,118].

An ultrahigh vacuum (UHV) sputtering for ultrathin film deposition on Ru or Pt surface was performed to determine the band gap and permittivity of the CT layer which was assumed an alternative to other high permittivity dielectrics for integration in future microelectronic devices like ultrathin metal-insulator-metal capacitors and field-effect transistor gate stacks [119,120]. In contrast to previous data, the theoretical and experimental band gap are considerably higher due to different defect densities or impurities and the difference can be ascribed to the usage of sputtering from high purity CT within the UHV sputter system reducing the number of defects or dopants.

The congruent ablative pulsed laser deposition from CT target under very low pressures of oxygen has been attempted [121–123] to deposit ultrathin CT layers with the stoichiometry matching the CT target. This goal has been utterly fulfilled with epitaxial growth of relatively thick CT layers on the $SrRuO_3$ buffer layer of $SrTiO_3$ and $LaAlO_3$ substrates [120] and partly succesfull in growing ultrathin $TiO_2$-terminated [122] or rutile-interposed [123] CT films.

The orthorhombic CT phase, stable up to ~1240 °C, was long considered a non-polar paraelectric material. It was only recently that ferroelectric CT property was detected at low temperatures in ~10–20 nm thick epitaxial CT films grown on surfaces which induce tensile epitaxial strain and increase the paraelectric to ferroelectric

**Table 15**
CT nanocomposites produced by sol gel-synthesis.

| Synthetic conditions | CT coat properties | CT coat application | Ref. |
|---|---|---|---|
| Ca nitrate, Ti isopropoxide dissolved in 2-methoxyethanol, nitric and lactic acids stabilizers, spin coating on Si wafers, heating at 400° C, crystallization by rapid thermal processing at 500–800° C in oxygen | 1–2 μm thick polycrystalline films with 150–200 nm-sized grains; crack-free adherent films on α-Ti substrates and slightly cracked films | Potential intermediate layer inhibitor of dissolution of hydroxyapatite coats on titanium implants | [145] |
| Ti butoxide, $CaCO_3$, solution in citric acid; multiple spin coating on a Pt/Ti/$SiO_2$/Si substrate, 3 min heating at 120 and 700° C and 1 h calcination at 700° C | Orthorhombic phase, uniform thickness and smooth surface of 65 nm, 200 nm, 250 nm and 340 nm thick films | Intrinsic mechanical properties of the films are thickness-dependent; potential for efficient performance in microwave dielectric device | [146] |
| Ti isopropoxide Ti $(OC_3H_7)_4$, hydrated Ca nitrate, spin coating on Si substrates, 10 min sintering in air at 300 and 800° C | 4 μm thick films with rough surface contaminated with anatase and carbonate impurities | Enhanced nucleation of calcium phosphate during immersion in SBF | [147] |
| Ti isopropoxide Ti $(OC_3H_7)_4$, hydrated Ca nitrate, HCl, $H_2O$, hydroxypropyl cellulose; dip-coating of quartz substrate, 1 h drying at 150° C, 1 h annealing at 400, 600 and 800° C | Homogeneous crack-free and nano-granular films with grain size 33–39 nm, porous structure and columnar topography | | [69] |
| Ti isopropoxide, CaO, EtOH, acetic acid, EDTA; Multiple spin-coating of Ti substrate, 24 h drying at 100° C and 1 h heating at 900° C | Coat of oval and closely packed 10 μm long and 5 μm wide particles | | [148] |
| Ca nitrate, Ti isopropoxide dissolved in 2-methoxyethanol, nitric and lactic acids stabilizers, spin coating on Ti substrate; drying at 150° C, pyrolysis at 400° C | Orthorhombic, 100 nm–3 μm thick films, crystallite size 25–35 nm, | Durable in SBF for at least 3 months, mechanical performance inproved by a thin diffusion $TiN_x$ layer | [149] |

transition temperature ($T_C$, Currie temperature) up to 140 K [124] or 175 K [125]. The ferroelectric properties of the thin CT films have been also detected when these films were deposited on substrates inducing compressive epitaxial strain and such ferroelectric films are stable at room temperatures and up to 800 K [126]. These ferroelectric tensile and compressive strained films respectively exhibit orthorhombic-like point group symmetry and a near-tetragonal unit cell and were grown using laser [123] or hybride molecular beam epitaxy (MBE) [125,126] within the self-regulated stoichiometric growth window which does not allow formation of defects originating from non-stoichiometric growth and destabilizing the ferroelectric phase.

Metalloorganic chemical vapour deposition (MOCVD) of CT films using organocalcium and organotitanium precursors [127–129] yields CT films containing $Ca(OH)_2$, $Ca_4Ti_3O_{10}$ and $TiO_2$ and the deposition of the single CT phase was achieved at the Ca/Ti precursors ratio lower than 1 [127,128]. The occurrence of columnar texture with small gaps is likely due to relaxation of thermal stress between the films and the substrate. The laser-induced MOCVD performed at different AlN substrate temperatures allows formation of (011)-, (101)- and (121)- oriented CT films of diverse morphologies at deposition rate 10 times higher than conventional thermal MOCVD [130,131].

All films prepared by physical and physicochemical methods are characterized in Table 13 and those obtained by MOCVD are illustrated in Fig. 13.

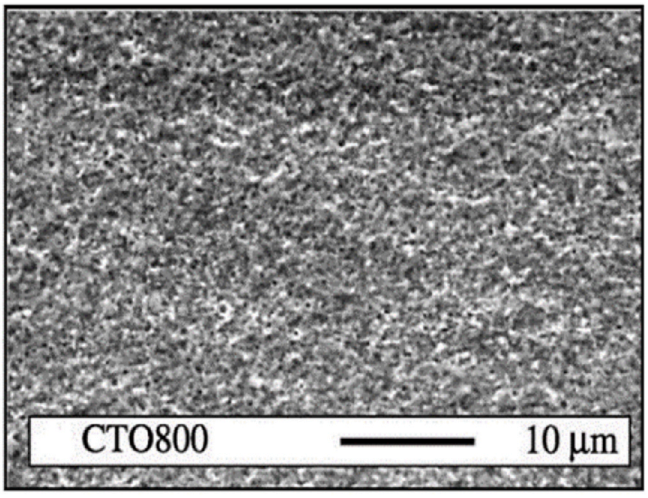


**Fig. 21.** Surface image of CT film prepared by spin coating and calcination at 800 °C. Reproduced from ref. 147, Copyright Elsevier.

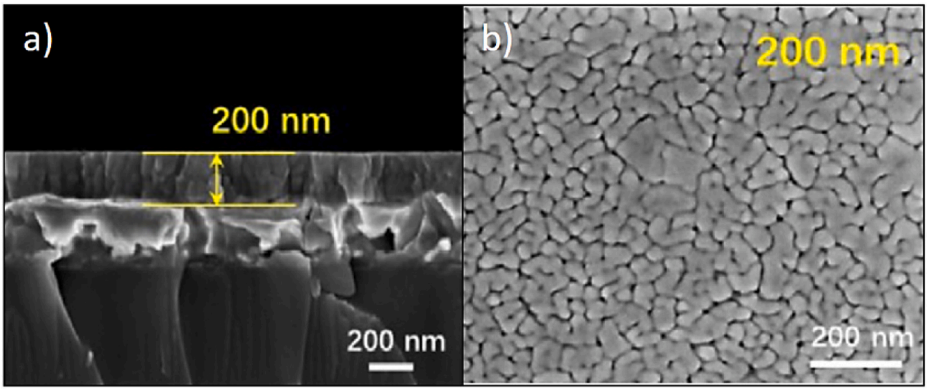


**Fig. 20.** Cross-section and surface images of CT film prepared by spin coating and calcination at 800 °C. Reproduced from ref. 146, Copyright Elsevier.

**Table 16**
Nanocomposite photocatalytic particles for water splitting.

| Synthetic conditions | Particles properties | Particles application | Ref. |
|---|---|---|---|
| Hydrothermally produced CT nanocrystals (0.1–0.4 μm, surface area 11.2 $m^2$/g), impregnation with aqueous $H_2PtCl_6.6H_2O$ and heat treatment | Pt/CT nanocomposite with 0.1–0.5 wt% Pt content | Photocatalyst of splitting $H_2O$ with UV light | [151] |
| CT nanocrystals (<100 nm, BET surface area 6.01 $m^2$/g after heating at 800° C) produced by sol-gel polymer precursor route, impregnation by irradiation of aqueous MeOH $H_2PtCl_6.6H_2O$ solution with simulated solar light | Pt/CT nanocomposite with 0.1 wt% Pt content | Photocatalyst of splitting $H_2O$ with UV light, $H_2$ evolution efficiency surpassing those of Pt-impregnated $ZnTiO_3$ and $NiTiO_3$ | [152] |
| Pt-loaded micro- and nano CT particles developed from cubic, concave cubic and rod-like nanoparticles, $H_2PtCl_6.6H_2O$ impregnation and photoconversion to Pt nanoparticles | PT/CT nanocomposite, cubic, concave cubic and rod-like cubic micro and nano particles with scattered 2–5 nm Pt nanoparticles; respective surface area 3.2, 3.1 and 9.7 $m_2$/g; band gap 3. 6 eV | UV–Vis photocatalytic evolution of $H_2$ from methanolic aqueous solution | [94] |
| CT nanosheets produced by hydrothermal route from anatase and rutile; subsequent impregnation in $H_2PtCl_6{\cdot}6H_2O$ aqueous solution, reduction of Pt-CT precursor by $H_2$, 5 h annealing at 700° C | Pt/CT nanocomposite, uniform nano-sheets with disordered surface, diameter 3–5 μm, thickness <100 nm, band gaps similar to $H_2$-untreated sample, EPR g-factor of $V_O$s 2.002 | UV–Vis photocatalyst of water splitting, high photocatalytic evolution of hydrogen | [153] |
| CT nanoparticles obtained by wet ball milling of $CaCO_3$ and $TiO_2$, Impregnation in $H_2PtCl_6{\cdot}6H_2O$ methanolic aqueous solution, Pt photodeposition by UV lamp | Pt/CT nanocomposite, 0.5–1 μm nanoparticles, crystalline size 31 nm, BET surface area 1.7 $m^2$/g, band gap 3.5 eV | UV photocatalyst for water cleavage and steam reforming of methane | [154] |
| CT nanoparticles, impregnation by $AgNO_3$ in $H_2O$-glycerol, Ar atmosphere, UV–Vis irradiation for conversion to $Ag^0$ | Ag/CT nanocomposite, size <100 nm, total surface area 6.7 $m^2$/g), Ag nanoparticle size 19 nm | UV–Vis photocatalyst of water splitting | [155] |
| CT nanoparticles prepared by solid state $CaCO_3$-rutile reaction in salt (KCl, NaCl, $CaCl_2$) flux or by wet ball-milling route, Ag nanoparticles were loaded by photodeposition in aqueous MeOH (reductant) | Ag/CT nanocomposite, Crystallite size 25–29 nm, Surface area 1–3.5 $m^2$/g, Average particle size ~1–3 μm | UV–Vis photocatalyst of water splitting and $CO_2$ reduction | [156] |
| AgCl/Ag nanoparticles introduced on hydrothermally produced nanosheet CT particles by UV–Vis photodeposition in HCl-acidified aqueous $AgNO_3$ solution, 6 h drying at 80° C | 2D AgCl/Ag/$CaTiO_3$ nano-heterojunction, 10-15 nm-AgCl/Ag nanoparticles on porous CT surface (pore size 13 nm, surface area 163.5 $m^2$/g), absorption extended to visible region | UV–Vis photocatalyst of water splitting, | [157] |
| Hydrothermally produced [58] nanosheet CT particles, treated with CdSe QDs in solution, dried at 60° C in vacuum | CdSe QDs/CT nanocomposite, visible absorption edge at 612 nm, CT band gap 3.27 eV CdSe band gap 1.6 eV | Highly stable and recyclable UV–Vis photocatalyst of water splitting | [158] |
| CT particles obtained by solvothermal route using $Ca(NO_3)_2.4H_2O$, Ti butoxide, NaOH, PEG-$H_2O$, 15 h heating in Teflon-lined vessel at 150° C and 12 h drying at 90° C; Treatment with aqueous $ZnCl_2$, $InCl_3$ thioacetamide solution at 80° C | $ZnIn_2S_4$/CT nanocomposite, cuboids of 600–700 nm and 400–450 nm sized edges, visible absorption edge at 535 nm, CT band gap 3.33 eV CdSe band gap 2.32 eV | Visible light photocatalyst for efficient hydrogen production | [159] |
| Hydrothermally prepared nanosized CT fusiforms from aqueous Ca nitrate, Ti butoxide and NaOH in teflon-lined vessel 24 h heated at 200° C, ultrasonic-assisted reactive dispersion of nano CT fusiforms with nano g-$C_3N_4$ particles for 24 h at 140° C and 6 h drying at 80° C | Porous nano g-$C_3N_4$/CT fusiforms, diameter 80–120 nm, length >300 nm, surface area 43.4 $m^2$/g pore size 18.5 nm | Solar light photocatalyst of water splitting | [160] |

### 3.2. Hydrothermal route

The hydrothermal route (Table 14) was used to deposit CT films on Ti substrates, fluorine-doped tin oxide (FTO), FTO-coated glass, titanium screws or TiAl alloys. It is common agreement that principle chemical reactions during CT hydrothermal synthesis in sealed vessels are controlled by reaction conditions and that higher temperature and pressure promote dissolution of Ti source precursor and increasing pH promotes formation of CT seeds.

A rather simple hydrothermal route for fabrication of CT films consists in heating titanium plates with a solution of calcium-ethylenediaminotetraacetic acid chelate, which enables to coat Ti surfaces with uniformly fixed microplatelets without any harm from the precipitation within solution [132]. The procedures using aqueous solution of Na or K hydroxide and Ca salt ($CaCl_2$) result in differently structured CT surfaces [133,134] and allow formation of intimately contacted euhedral cubes [135]. The synthesis of crystalline CT coatings from titanium screws pretreated by acidified hydrogen peroxide and mildly heated in alkaline solution of Ca salt does not require further calcination treatment which is normally needed for producing crystalline CT species and allows formation o densely accommodated cubic microparticles [136]. These different structures are shown in (Fig. 14).

The occurrence of the cubic CT phase in Ref. [134] appearing via a strong diffraction peak at 33.3° of the (1 10) lattice of cubic CT (JCPDS file 65–3287) is very interesting, since this phase normally exists only at very high temperatures and pressures [8] and its ambient existence was so far detected only in nanoparticles produced by high energy milling using the high ball to powder weight ratio, which may tremendously

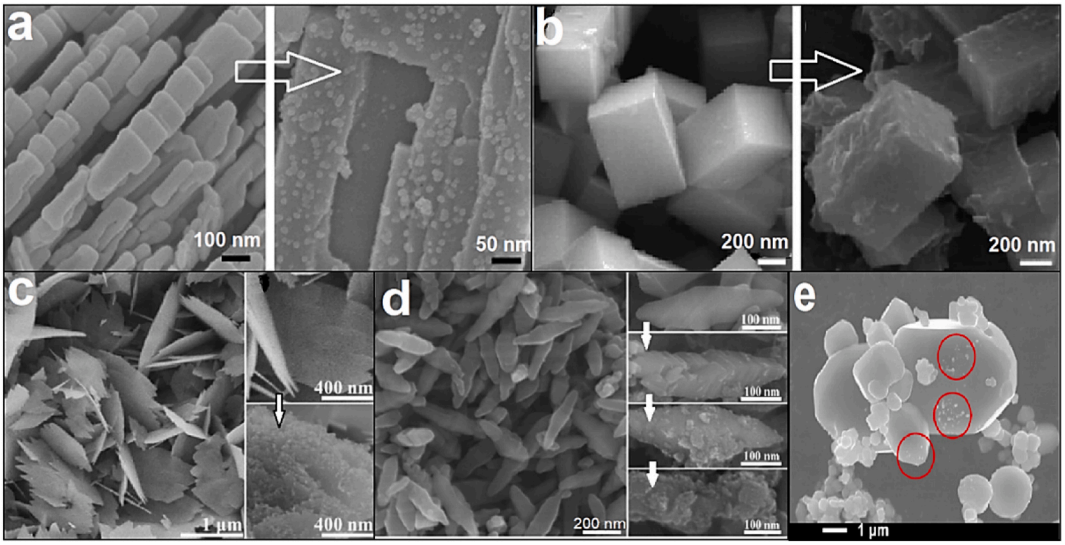


**Fig. 22.** Surface changes of pristine CT particles incurred by deposition of other nanoparticles. Deposition of CdSe QDs on CT nanosheets (a, reproduced from ref. 158, Copyright Elsevier), deposition of $ZnIn_2S_4$ nanoparticles on CT nanocubes (b, reproduced from ref. 159, Copyright Elsevier), deposition of AgCl/Ag nanoparticles on CT nanosheets (c, reproduced from ref. 157, Copyright Elsevier), deposition of nano g-$C_3N_4$ particles on CT fusiforms (d, reproduced from ref. 160, Copyright Elsevier) and deposition of Ag nanoparticles on oval μm-sized CT agglomerates (e, reproduced from ref. 156, Copyright Elsevier). The arrows illustrate the morphology changes from the pristine CT surface to the surface enriched by other particles and in (d) the evolution of CT surface roughening upon increasing amount of the depositing particles.

**Table 17**
Nanocomposite photocatalytic particles for removal of pollutants.

| Synthetic conditions | CT nanocomposite properties | Application | Ref. |
|---|---|---|---|
| N-CQDs solution from hydrothermal treatment of citric acid and urea added to aqueous CT precursor solution (Ca nitrate, PEG, Ti butoxide, NaOH) solvothermally treated in Teflon vessel at 15 h heated at 180° C for 15 h, drying at 60° C | N-CQDs/CT nanocomposite, 0.5–1.0 μm cubic particles, surface area 6.4 $m^2$/g, Vis absorption at 400–550 nm | Visible light photocatalyst for adsorption and oxidative removal of NO | [161] |
| $HAuCl_4$ solution added to ultrasonically activated CT nanocuboids hydrothermally prepared from P25 $TiO_2$ powder) suspension in aqueous ammonium oxalate solution and UV photoreduced to $Au^0$ nanoparticles, 2 h drying at 60° C | Au@CT nanocomposite,3–7 nm Au nanoparticles on nano CT cuboids (width 0.3–0.5 $\mu$m, length 0.8–1.1 $\mu$m) band gap 3.49 eV | Photocatalyst for UV, visible and simulated solar light induced degradation of aqueous RhB dye | [162] |
| Solvothermally prepared μm-sized sheets [101] suspended in aqueous solution of $AgNO_3$, $NH_4OH$ and cetyltrimethylamonium bromide yielded AgBr/CT powder, UV–Vis photoreduction, drying at 80° C | Ag@AgBr/CT nanocomposite with AgBr(cubic phase)/Ag nanoparticles deposited on μm-sized CT sheets, enhanced absorption within ~450–800 nm, band gap 3.28 eV | Visible light photocatalyst for degradation of aqueous MO dye | [163] |
| $Ca_{0.01}Fe_{2.99}O_4$ particles solvothermally treated in Teflon-lined vessel with $CaCl_2{\cdot}2H_2O$, Ti butoxide and NaOH dissolved in EtOH–$H_2O$; 24 h heating at 180 °C, 2 h drying at 90° C | Magnetic $Ca_{0.01}Fe_{2.99}O_4$/CT nanocomposite, spherical 85–200 nm-sized $Ca_{0.01}Fe_{2.99}O_4$ particles appended to a blend of sheet-, prism- or rod-like sub-μm-sized CT particles, enhanced visible absorption up to 710 nm | Visible-light induced photocatalytic decoloration of MB dye | [164] |
| Ultrasonic treatment of CT nanoparticles prepared by sol-gel polyacrylamide route [73] in MeOH–$H_2O$-acetic acid solution of $Bi(NO_3)_3{\cdot}5H_2O$ and NaBr, heating in Teflon-lined vessel at 200 °C for 5 h, 12 h drying at 60° C | CT/BiOBr nanocomposite,0.7–2.2 μm-sized and 70–110 nm thick BiOBr microplates decorated with spherical 15–50 nm-sized CT particles | Solar-light photocatalyst for degradation of aqueous RhB dye | [165] |
| Commercial CT and $TiO_2$ powders were mixed and heated at 600 and 600° C, milling by use of a zirconia mortar | Composite anatase/CT powders | Enhanced visible-light photo-bleaching of MB dye | [166] |
| Ultrasonic assisted precipitation–visible light-photoreduction process from aqueous solution of $AgNO_3$, NaCl and solvothermally [103] produced CT | Ag/AgCl/$CaTiO_3$,Ag/AgCl dots dispersed on 1-5 μm-sized fern-like CT, 350–800 nm absorption | visible-light photocatalyst of RhB degradation, more efficient than CT | [167] |
| Decoration by $Ag_2S$ nanoparticles of CT sub-μm-sized particles obtained by hydrothermal treatment of P25 $TiO_2$ suspended in aqueous solution of NaOH and $CaCl_2$ and 24 h heated in Teflon-lined vessel at 200° C, 12 h drying at 60° C | $Ag_2S$@CT nanocomposites,7-17 nm-sized $Ag_2S$ particles decorated on surface of CT particles of 0.8–1.1 μm in length and 0.3–0.5 μm in width,Band gap ~ 3.6 eV | UV and visible light photocatalyst for degradation of aqueous RhB dye | [168] |
| Sol-gel polymer precursor approach with acrylamide [73] applied to prepare CT nanoparticles which dispersed in EtOH with graphene were ultrasonically treated for 10 h at 60° C | CT/graphene nanocomposite,31–42 nm CT particles appended on 2D-sheet-like graphene, enhanced light absorbance over UV–visible light region | UV light photocatalyst for degradation of aqueous MO dye | [169] |
| CT powder (prepared by microwave assisted hydrothermal route from $TiO_2$ P25, $CaCl_2$, urea and NaOH) was suspended in methanolic $AgNO_3$ solution and exposed to UVC irradiation, drying at 70° C | Ag/CT nanocomposite,13.5 nm-sized Ag nanoparticles homogeneously distributed on CT cuboids (210-140 nm x 700–800 nm) having layered structure | Photoinactivation of green tide | [170] |

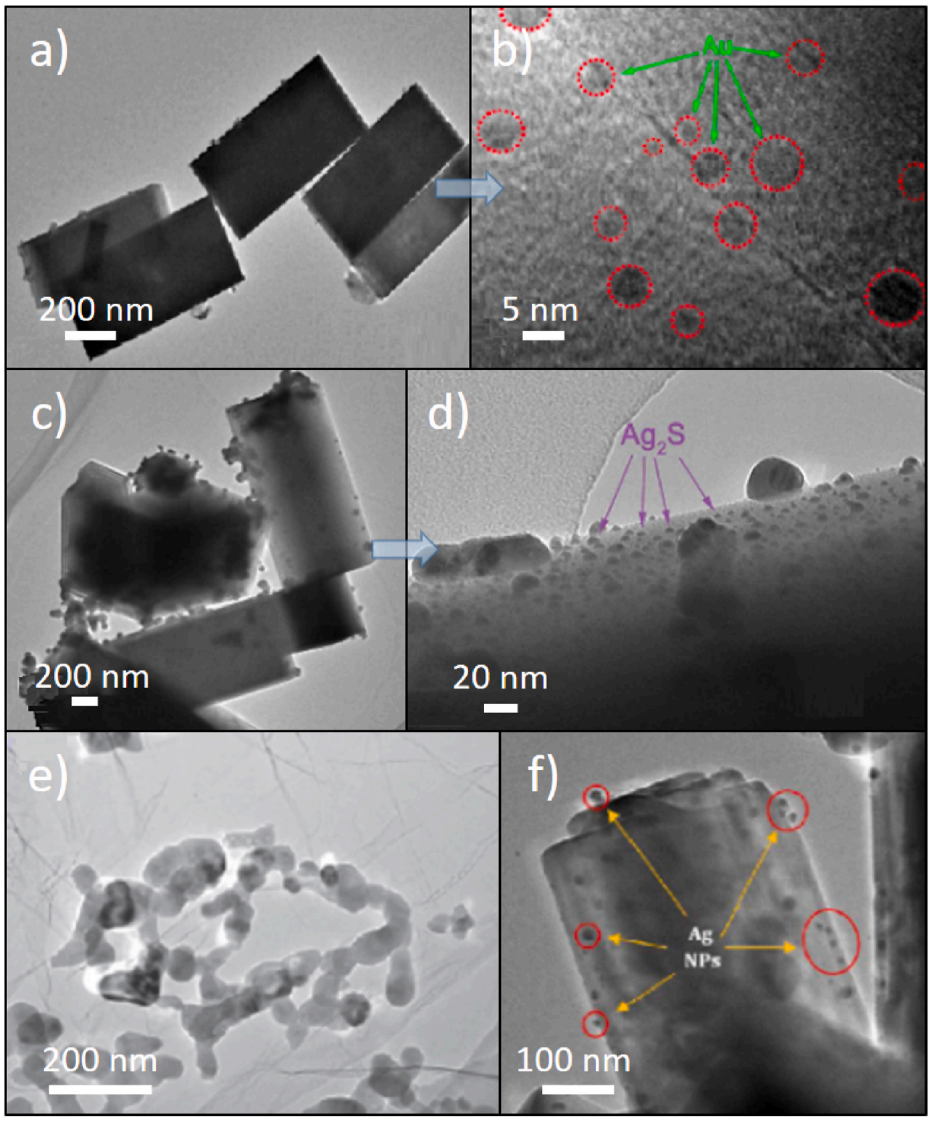


**Fig. 23.** Au nanoparticles deposited on CT nanocuboids (a, b reproduced from ref. 162, Copyright MDPI), $Ag_2S$ nanoparticles deposited on CT nanocuboids (c. d, reproduced from ref. 168, Copyright Desalination Publications), CT nanoparticles on graphene sheets (e, reprinted from ref. 169, Copyright IOP Publishing) and Ag nanoparticles on CT nanocuboids (f, reproduced from ref. 170, Copyright Elsevier).

increase surface area of the milled powders [26]. It can be therefore presumed that the very thin cubic CT layer adhearing on the nanoporous $TiO_2$ layer is uniquely stabilized by the structure of the nanoporous $TiO_2$ layer which may offer unusual epitaxy growth of cubic CT owing to its unique structure produced via calcination of dispersed $TiO_2$ sol with sacrificing ethyl cellulose and terpineol.

Two different micro-morphologies, specifically initial mesoporous micro-flowers and final micro-nests, were developed by hydrothermal treatment of amorphous flower-like $TiO_2$ microstructers which were preformed from ZnO flower-like microstructures as templates (Fig. 15). The initial CT micro-flower morphology develops through surface dissolution of sacrificing amorphous $TiO_2$ micro-flowers and reaction between $[Ti(OH)_6]^{2-}$ and $Ca^{2+}$ ions leading to self-organization of perovskite building blocks, while the ensuing transformation from micro-flowers to micro-nests [137] likely involves Ostwald ripening process of perovskite nanocrystals.

Crystalline CT surfaces incorporating nanoparticles were also prepared by facile two-step anodization–hydrothermal treatment in which highly regular $TiO_2$ nanotubes on Ti foil were first formed by the anodization in glycerol [138] and glycerol-$H_2O$ [139] electrolyte solution, or nanoporous $TiO_2$ surface were first formed by anodization in ethylene glycol [140] electrolyte solution. In the second step were these templates used as the starting material for hydrothermal transformation onto highly ordered CT nanotubes (Fig. 16), crystalline CT nanobricks (Fig. 17) or differently structured CT films composed of predominant micrometer-sized brick-, eliptic-, prism- and minor flower-like morphologies, whose size and form depend on the concentration of NaOH (Fig. 18).

One step hydrothermal-electrochemical treatment was accomplished with TiAl alloy samples by heating the Ti anode in agueous Ca $(OH)_2$–NaOH solution to prepare CT coats which can increase oxidation resistance of TiAl materials [141]. The produced CT films were well-crystallized CT prisms without apparent intermediate $TiO_2$ layer (Fig. 19).

This method was also applied with a Ti plate as an anode and it results in the formation of thin CT film mainly composed of microplate regions [142,143]. These films immersed in SBF induce deposition of Ca phosphate layer, which is believed to be due to Ca species adhered to CT substrate. Two-step hydrothermal treatment and ion exchange method was performed to fabricate a micro-sheet structured CT scaffold which proved its osteoconductive behaviour [144].

**Table 18**
Other photolytic and catalytic effects of nanocomposite particles.

| Synthetic conditions | CT nanocomposite properties | Application | Ref. |
|---|---|---|---|
| CT powder (prepared by sol-gel polymer precursor approach with Ti tert-butoxide, Ca sec-butoxide, acetic acid, Pluronic, alcohol, HCl and 4 h calcination in air at 450° C; UV–Vis photodeposition of Pt from $H_2PtCl_6{\cdot}6H_2O$ in aqueous CT suspensions | Pt/CT nanocomposite, 3–5 nm Pt dots on nanoporous agglomerated CT nanocrystals, surface area 62–70 $m^2/g$, band gap 2.79–3.14 eV, enhanced visible light absorption | Visible light photocatalyst for conversion of nitrobenzene to aniline | [171] |
| 2 h annealing of $CaCO_3$ with $TiO_2$ at 1500° C | CaO/CT composite, ultrafine particles | Catalyst of transesterification of sunflower oil with methanol at 60° C | [172] |
| Sol-gel hydrothermal treatment using Ti butoxide, acetic acid, EtOH–$H_2O$, CaO, 24 h heating in Teflon-lined vessel at 150° C, calcination at 550° C | Mesoporous CT with surface-stabilized basic $Ca^{2+}$ –$O^{2-}$ sites, pore size mainly 4.5–7 nm, surface area 31.4 $m^2/g$, agglomerated sub-μm-particles | Catalyst of transesterification of waste cooking oil into biodiesel | [173] |
| Ti butoxide hydrolysis in nano-$CaCO_3$ suspended in ethanol, heating of solid $Ti(OH)_4$-coated $CaCO_3$ precipitate at 500° to get a blend of CaO and $TiO_2$ and further calcination at 850° C to obtain CT-coated Ca nanoparticles | CaO nanoparticles coated with nanoscale CT layer produced via intermediate $TiO_2$-coated CaO nanoparticles | $CO_2$ reactive adsorbent, high durability of reactive sorption capacity verified by multiple carbonation-calcination cyclic runs | [174] |
| Ultrasound treatment of Ti butoxide, ethylene glycol, Ca hydroxide and $H_2O$ with graphene oxide sheets (GOS), freeze drying | GOS sheets decorated with ~20 nm-sized CT nanospheres | CT/GOS modified electrode for electrocatalytic and electrochemical sensing of chemotherapeutic drug flutamide | [175] |
| Slurry of CT powder and Ca nitrate in water stirred, dried and 4 h heated at 400° C in air and activated by methanation process | μm-sized CT particles coated with 10–30 nm-sized NiO nanoparticles | CT supported Ni nanoparticle catalyst for enhanced CO methanation | [176] |
| Different proportions of solvothermally prepared $TiO_2$ nanosheets and saturated $Ca(OH)_2$ solution were hydrothermally treated to achieve etching on (001) facet-exposed $TiO_2$ nanosheets for 2 h at 180° C, drying at 60° C | Integrated heterostructure CT/$TiO_2$ composites with enhanced-surface basicity to facilitate $CO_2$ adsorption and activation for reactive $CO_2$ reduction to CO in water | UV–Vis solar photocatalyst of $CO_2$ to CO conversion with performance almost 6 times higher than CT photocatalyst | [177] |

### 3.3. Sol gel route

Both simple sol-gel approach (2.2.2.) and sol-gel polymer precursor approach (2.2.3.) used for the fabrication of nano and micro CT particles were applied to prepare CT films on silicon, quartz, titanium and Pt/Ti/$SiO_2$/Si substrates. The sol precursor solution used for the interaction with these substrates was primarily produced from titanium isopropoxide, carboxylic acid and Ca salts (Table 15) and contained, in some cases, hydroxypropyl cellulose [69] or EDTA [148]. Typical CT coating procedures involve dipping or spin coating techniques to prepare sol layer on substrate, conversion to gel or resin by drying and heating and final calcination in air or oxygen. These steps are necessarily repeated in order to obtain films of required thickness. The SEM of thin nanosized smooth films prepared in Ref. [146] and thick μm-sized rough films prepared in Ref. [147] are respectively given for illustration in Fig. 20 and Fig. 21.

**Table 19**
Bioconductive nanocomposite particles.

| Synthetic conditions | CT nanocomposite properties | Application | Ref. |
|---|---|---|---|
| CT-$CaCO_3$ particles prepared from Ca nitrate and Ti i-propoxide in i-PrOH; CT-aC particles prepared from CaO, Ti i-propoxide, 2-ethylhexanoic acid/butanol; drying at 110° C and 2 h heating at 650° C | CT–$CaCO_3$ and CT-aC particles exert better osteoblast response than CT | Biomaterial for medical and dental applications | [178] |

## 4. Nano and micro $CaTiO_3$ composites - synthesis and use

There are more nano- and fewer micro-sized CT composite materials which occur as powders or coatings on various substrates and considerable efforts have been devoted to investigating these materials and achieving properties in some respect better than those of nano and micro CT forms. Their fabrication benefits from the earlier described syntheses of various single CT forms and a choice of proper composite component depends on the field of interest and potential application.

### 4.1. Nano and micro composite particles

Literature screening for nano- and microsized CT composites reveals that the nanosized entities have been paid much greater attention and that reports on micro-sized entites concern mostly 2D particles which have the third dimension of nanometer size.

The nanocomposite particles have been prepared for exploration of their potential use in photocatalytic water splitting, phorocatalytic degradation of pollutants in aquatic environment, as catalysts and adsorbents and also for upgrading physicochemical and electrochemical properties of single nano/micro CT forms.

#### 4.1.1. Photocatalysts of water splitting

Semiconductor-based photocatalysis of water splitting to form hydrogen and oxygen using solar light has been pursued by researchers as a potential means of clean and large-scale fuel production. However, an efficient solar-to-hydrogen energy conversion is hampered by poor activation of semiconductors and rapid recombination of photo-generated electron/hole pairs. One of approaches attempted to overcome these disadvantages is water splitting by using CT photocatalysts (Table 16) having an intimate contact with another nanospecies serving as a suitable co-photocatalyst.

An impregnation of CT photocatalyst with highly dispersed Pt nanoparticles, produced from hexachloroplatinic acid [150], by UV or solar photodeposition and/or subsequent $H_2$-thermal treatment [94,151,152] is of help to develop such a synergetic photocatalytic system.

Furthermore, CT surface can be also considered as composed of a topmost and a subsurface layer and it is possible that both layers, known to show different performance in catalytic reactions, can also exhibit different photocatalytic properties. Such photolytic non-equivalence of both layers was observed with CT nanosheets obtained by the simple

**Table 20**
Nanocomposite coats and their effects.

| Synthetic conditions | CT nanocomposite properties | Application | Ref. |
|---|---|---|---|
| Aerosol assisted CVD of mixed $Ca_2(CF_3CO_2)_3(CH_3CO_2)(i\text{PrOH})(H_2O)(THF)_3$ complex and Ti isopropoxide on FTO substrate at 500, 550 and 600° C | Anatase/CT nanocomposite film composed of 0.3–1.8 μm-sized spherical particles, enhanced visible absorption up to 800 nm, band gap 3.0 eV, | Photoelectrodes in photo-electrochemical water splitting | [179] |
| Pluronic F127-assisted solvothermal treatment from Ti i-propoxide, $CaCl_2$, NaOH in EtOH–$H_2O$ at 180° C, calcination at 550° C;<br>Solvent casting of dispersed Pluronic and CT particles, drying at 80° C, composite membranes hot-pressed at 50 atm, 175° C | Nonstoichiometric $CaTiO_{3-\delta}$ in Nafion membrane, 100–150 μm thick, crystallite size 145 nm, specific surface area 6.6 $m^2/g$ | Water-retention and reinforcing additive in low-humidity proton-exchange membrane | [180]<br>[181] |
| Electrodeposition of $CaHPO_4$ dihydrate and alkaline conversion to HaP, dip-coating in stabilized $TiO_2$ sol, annealing in air at 600° C, water steam treatment, dip-coating in PLA solution | (HA/CT/$TiO_2$/PLA coat, total thickness 2 mm, immersion/electrochemical tests in Hanks solution | Good adhesion and corrosion resistance of coated AZ31 alloy | [182] |
| Ti anodization in $H_2SO_4$ solution, liquid phase oxidation in $HNO_3/H_2O_2$ solution or thermal oxidation at 400° C in air, ensued by hydrothermal treatment in $Ca(OH)_2$–$Na_2SiO_3$ alkaline solution in Teflon-lined vessel at 180° C | Superhydrophilic CT/$SiO_3^{2-}$ coats, water contact angle <22 deg., increased fibronectin and albumin adsorption | Long lasting hydrophilicity, increased protein adsorption and enhancement of osteocondictivity | [183] |
| 3D printing on silicon resin containing 400-mesh $CaCO_3$ and $TiO_2$ powders, 3 h sintering at 1000–1200° C in Ar atmosphere | CT-incorporated β-$Ca_2SiO_4$ composite scaffold with regular marcoporous (400 μm) structure and μm-sized pores, enhanced cell proliferation and bone regeneration | Potential prototype for bone tissue engineering | [184] |
| Heating Ti plate in aqueous calcium hydroxide slurry at 600 and 800° C, CT/$TiO_2$ surface ratio depends on water content in heated slurry and annealing temperature | Surface layers of CT/$TiO_2$, layer richer in CT promotes Ca phosphate in Hanks solution compared to layer richer in $TiO_2$ | Inducer of biomimetic formation of calcium phosphate from SBF | [185]<br>[186] |
| Plasma electrochemical oxidation of Ti6Al4V plates in aqueous Ca acetate, $Ca(H_2PO_4)_2$, EDTA, heating with aqueous NaOH at 60° C, calcination at 800° C | Surface layer of CT/$TiO_2$,<br>Composed of CT, anatase and rutile and containing Na | Inducer of biomimetic formation of hydroxyapatite from SBF | [187]<br>[188] |
| Ti plate soaked in each of HAp and CT solutions prepared from Ti iso-propoxide or bis(2-ethylhexyl) hydrogen phosphate and added to CaO powder in BuOH diluted in 2-ethylhexanoic acid, heating at 650° C | Altering quadruple sequence of a-C-CT and HAp layers with respective 0.6 and 2.4 μm thicknesses,<br>Amorphous a-C layer contains agglomerated 10–20 nm sized CT particles | Enhanced adhesion to Ti surface | [189] |
| Dip coating of Ti substrate in CT-aC and HA solutions respectively prepared from CaO, 2-ethylhexanoic acid, BuOH, Ti propoxide and from CaO, BuOH, bis (2-ethylhexyl) hydrogen phosphate; drying at 110° C, annealing at 650° C | CT-aC coat induces enhanced MT3T3-E1 cell attachment, proliferation, and osteoblastic differentiation compared to HA coat | Bioconductive surface | [190] |
| Magnetron (enhanced with additional radiofrequency plasma source) sputtering of CT target combined with Ar plasma induced Ti ion implantation | Ti-implanted CT films on Si, wafer, 10–70 nm thickness, an excess of Ca and O as compared to the target stoichiometry, more Ca in outmost layer | Dissolution of CT films in SBF is impeded by Ti-implantation | [191] |
| Magnetron sputter-deposition of CT target and simultaneous implantation of accelerated titanium ions, annealing at 600° C; film thickness decreases with increased acceleration voltage or total Ti dose | Amorphous CT films on Ti,<br>Bonding strength of CT films to Ti increases with higher acceleration voltage and/or ion implantation dose, crystallization at 600° C and formation of $TiO_2$ layer between Ti substrate and CT | | [192] |
| 24 h heating of Ti plate or rod with KOH–$CaCl_2$ solution at 150° C in PTFE lined vessel and subsequent coating CT layer by 24 h heating in $K_2HPO_4$–KOH–$CaCl_2$ solution at 150–180° C in PTFE lined vessel | CT/HAp double layer containing $TiO_2$ of sufficient adhesion to Ti | Inducer of HAp formation from SBF | [135] |
| Coating HAp and CT in solution produced from Bis(2-ethylhexyl) hydrogen phosphate or Ti i-propoxide and added to CaO powder in BuOH diluted in 2-ethylhexanoic acid, respective annealing at 650 and 600° C | Double HAp(top)-CT layer on 50–200 μm pores punctured into Ti plate, thickness 4 μm, uncertain Ti distribution across the film, HAp contains tricalcium phosphate | HAp influences early bone ingrowth and exhibits enhanced osteocompatibility in smaller pores | [193] |
| Coating HAp pellets with Ti and annealing at 1100 °C for 2 h in air or in a $N_2/H_2$ gas mixture | Topmost CT spots on HAp surface with increased nanometer surface roughness, greater surface area, enhanced human osteoblast adhesion | CT increases osseointegration with juxtaposed bone | [194] |
| Ti surface modified via electrospun polyvinylidene/hydroxyapatite (PVP/HA) masking and subsequent scans of Nd:YAG pulsed laser irradiation | Adhesive networks of CT and α-tricalcium phosphate on Ti surface | Improvement of attachment and spreading of MG63 osteosarcoma-like cells | [195] |
| Composites with varying CT/HAp ratio sintered into pellets at 1200–1500° C for 3–5 h | Homogeneous distribution of 1–2 μm-sized CT particles along coarser calcium phosphate phase | Good adhesion, spreading and proliferation of L929 mouse fibroblast and SaOS2 human osteoblast cells | [196] |
| Homogenized Ti-HAp, CT-HAp and CT-TCP (tricalcium phosphate) nanopowder mixtures pellets nanopowder mxtures cold pressed into pellets, 3 h heated at 1100° C | Nanocomposite CT/HAp and CT/TCP<br>Human osteoblast adhesion and spreading enhancement with greater Ti substitution in HA lattice and with CT composites | Potential use of CT/TCP nanocomposite in orthopedic application | [197] |
| Laser cladding of dried paste, composed of μm-sized HAp and Ti powder in water glass, compacted on $(Zr_{0.62}Cu_{0.23}Fe_{0.05}Al_{0.1})_{97}Ag_3$ plate | 300 μm thick coat composed mainly of dendrite CT and minor $Ca_2P_2O_7$ | Potential bioactive coating on BMGs for biomedical implant applications | [198] |
| CT nanoparticles mixed in chitosan dissolved in acetic acid solution, lyophilization at −50° C, treatment of peeled off scaffolds in NaOH solution and DEI water | hybrid CT/chitosan scaffolds, orthorhombic CT nanoparticles distributed on amorphous chitosan scaffolds | Promotion of attachment, proliferation and biological function maintenance of Schwann cells | [199] |
| Hydrothermally treated Ti, Ti6Al4V and Ti13Nb13Zr alloy surfaces with mixed solutions of CaO and NaOH at 180° C for 2 h in Teflon-lined reactor, excess of NaOH or 2 h calcination at 400° C | Ca-incorporated crystalline CT-anatase film with sub-μm holes on surface, crystallinity increases with excess of NaOH,<br>enhanced hydrophilicity | Enhanced differentiation of pre-osteoblast MC3T3-E1 cells;<br>Inducer of Ca apatite from Hank's solution | [200–202] |

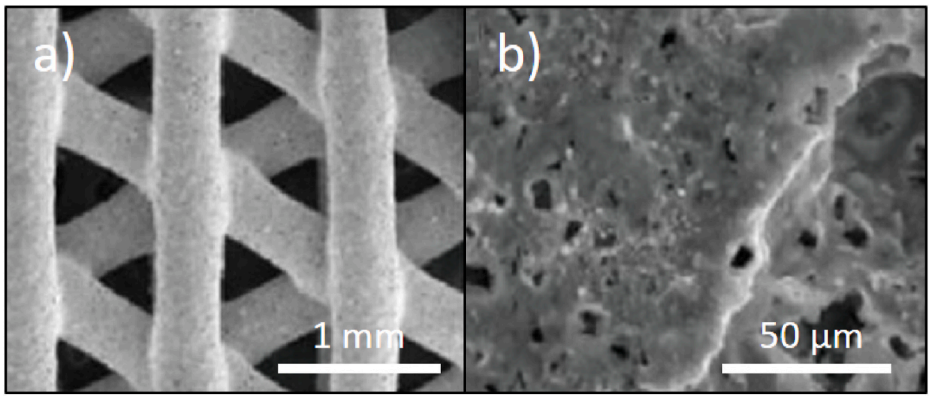


**Fig. 24.** SEM images of CT incorporated porous β-$Ca_2SiO_4$ composite scaffolds at different magnifications (a,b), reproduced from ref. 184, Copyright Elsevier.

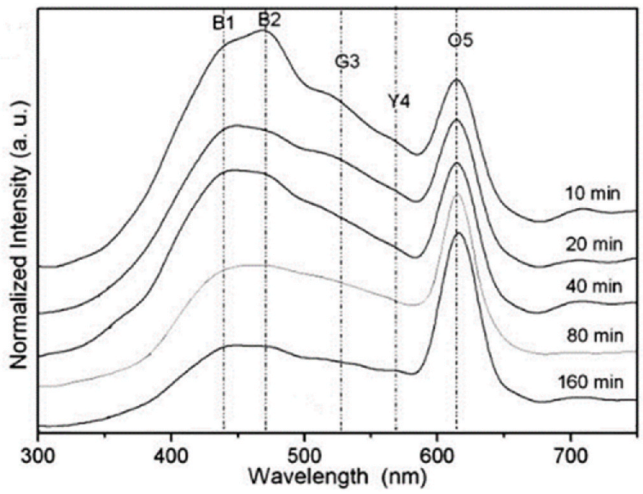


**Fig. 25.** Evolution of PL profile for CT nanoparticles generated by microwave assisted hydrothermal route and annealed for 10 up to 160 min before 350.7 nm excitation at room temperature. Reproduced from ref. 92, Copyright Elsevier.

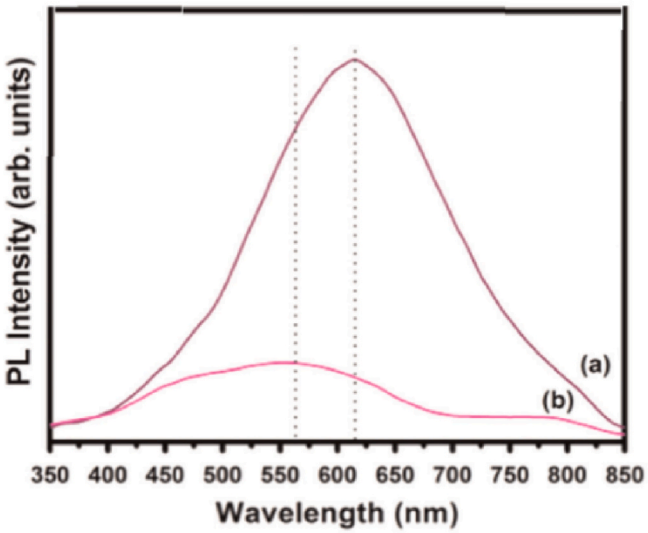


**Fig. 26.** Xe lamp excited PL spectra of CT nanoparticles produced from Ti isopropoxide (a) and Ti tetrachloride. Reproduced from ref. 93, Copyright Elsevier.

hydrothermal route and modified by Pt-catalyzed hydrogenation assisted by hydrogen spillover effect employed to avoid harsh reduction conditions leading to bulk defects [153]. Such hydrogenation induces an efficient disorder only in surface and sub-surface layers by creating oxygen vacancies. The disordered (topmost) surface layer is just 1–2 nm thick and the subsurface oxygen vacancies (sub-$V_O$s) can change energy band structure of CT nanosheets to form band tail states and improve charge separation, while surface oxygen vacancies (s-$V_O$s) can act as active centers facilitating $H_2$ formation.

Nano Pt/CT photocatalysts can also exhibit a higher production rate of hydrogen in a flowing mixture of water vapour and methane than in a flow of water vapour itself [154]. Considering the importance of the photocatalytic steam reforming of biomass as an alternative way to produce hydrogen, such hydrogen production through both photocatalytic water decomposition and photocatalytic steam reforming of methane may find use in industrial applications.

Other CT nanocomposite photocatalysts showing highly enhanced ability for inducing water splitting are Ag-loaded CT nanoparticles [155–157] of which one [157] exerts a double photocatalytic effect by promoting simultaneous water splitting on naked CT surface and $CO_2$ reduction to CO on Ag nanoparticles. Further nano CT composite photocatalysts with high water cleavage efficiency were fabricated through loading CT nanoparticles with CdSe quantum dots (QDs) [158] or $ZnIn_2S_4$ species [159] and by loading nanosized graphitic $C_3N_4$ particles on submicron fusiforms of CT nanoparticles [160]. The last nanocomposite prototype is an example of a nano-heterojunction in which enhanced $H_2$ photo-production is obviously caused by internal electric field of the nano-heterojunction and by high visible absorption and large surface area of the fusiform.

The deposition of the abovementioned nanoparticles on various forms of nano- and micro CT particles results in roughening of relatively flat pristine CT surfaces and this phenomenon is due to certain agglomeration of the depositing nanoparticles and is well observed by SEM and HRSEM analyses (Fig. 22).

#### 4.1.2. *Photocatalysts for removal of pollutants*

There are also several nanocomposite CT photocatalysts suitable for degradation of harmful pollutants (Table 17). The nitrogen-doped carbon quantum dots (N-CQDs) deposited on CT cubic nanoparticles decrease surface area but induce visible absorption of and NO adsorption on the formed N-CQDs/CT nanocomposite. Such nanocomposite also shows [161] high solar-light photocatalytic ability to oxidize NO to $NO_2^-$ and $NO_3^-$ and removes ubiquitous nitric oxide which is presently raising concerns as an aerosol precursor.

Many other nanocomposite particles exert capability to serve as photocatalysts for removal of harmful pollutants in aquatic environments or promote deactivation of hazardous marine algae tides. Some of them can make use of visible (solar) radiation [ [162–168]] and other

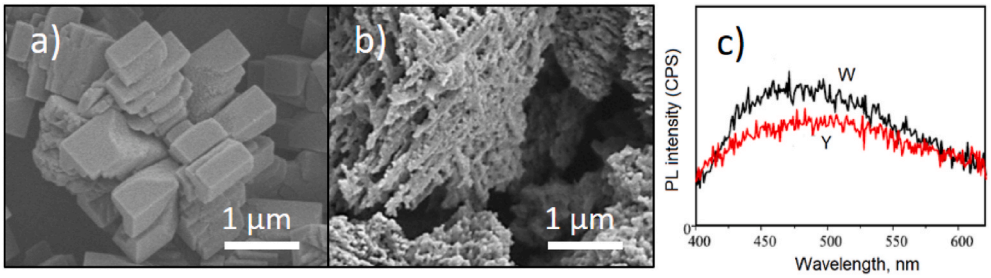


**Fig. 27.** SEM images and PL of W and Y powders excited by visible light of Xe lamp. Reproduced from ref. 100, Copyright Elsevier.

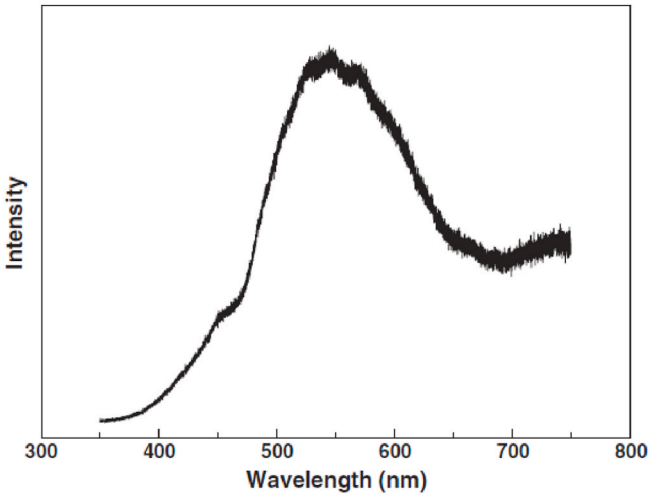


**Fig. 28.** Room temperature PL spectrum of CT nanoparticles obtained by solid state reaction upon excitation at 355 nm. Reproduced from ref. 39, Copyright Elsevier.

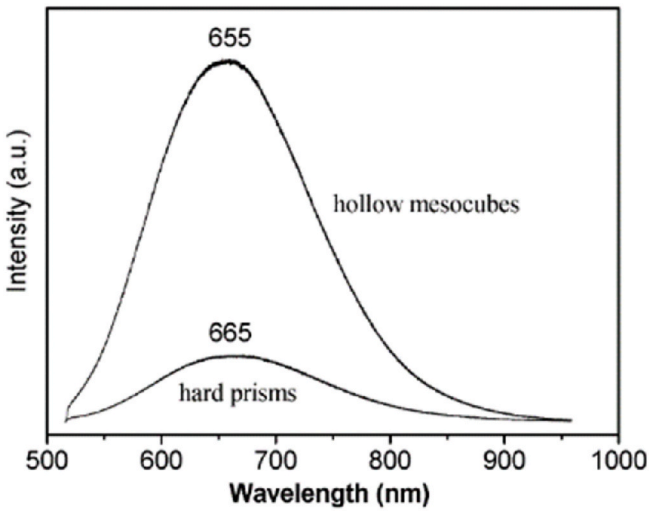


**Fig. 29.** Phootoluminescence of hollow mesocubes and rectangular prisms. Reproduced from ref. 101, Copyright Royal Society of Chemistry.

are active upon UV excitation [168–170].

The deposition of the abovementioned nanoparticles on surfaces of various forms of nano- and micro CT particles results in surface decoration by nm-sized particles but also in roughening of relatively flat pristine surfaces due to certain agglomeration of the depositing nanoparticles. SEM and HRSEM or HRTEM analyses are helpful to identify the size of the deposited particles and several post deposition morphologies are illustrated in Fig. 23.

#### 4.1.3. Other photocatalytic and catalytic effects

A Pt/CT nanocomposite can also act as a photocatalyst of conversion of nitrobenzene to aniline [171] and this eco-friendly route for aniline synthesis through solar light induced reaction may find further interest in search of an alternative applied process for aniline production from nitrobenzene.

Ultrafine particles of CaO/CT composite can catalyze methanolysis of sunflower [172] or waste cooking [173] oil at only moderate temperature, which is explained by a favorable effect of nano CaO entities stabilized on CT surface and is an important observation due to an ongoing research in the development of heterogeneous catalysts for biodiesel (a mixture of fatty acid methyl esters) production. Also CaO nanoparticles coated with CT nanoscale layer [174] present interestingly stabilized CaO entities near CT layer and can function as an efficient and durable $CO_2$ reactive adsorbent useable in many carbonation-calcination runs. Such phenomenon contradicts to low durability of reactive sorption capacity of the natural precursors of CaO-based adsorbents such as limestone and dolomite. CT nanospheres decorating surface of graphene oxide nanosheets attached to glassy carbon electrode enhance the electrocatalytic performance towards flutamide drug detection [175]. Ni nanoparticles supported on micron-sized CT particles catalyze methanation of carbon monoxide [176], which is important because of present interest in alternative routes of methanation of carbon oxide for production of synthetic natural gas and also for new strategies in reducing the emission of greenhouse gases in atmosphere. Nanocomposite $TiO_2$/CT particles with intimate CT-$TiO_2$ heterostructure developed by hydrothermal etching of $TiO_2$ nanosheets can serve as an efficient UV–Vis photocatalyst of $CO_2$ to CO conversion in water [177] and may also find more interest in helping to accomplish the abovementioned goals.

The syntheses and properties of these nanocomposites and their catalytic effects are given in Table 18.

#### 4.1.4. Biomedical materials

There is little interest in research of nano and micro sized particles finding use as biomaterials, because bioactivity of nano and micro sized species has been greatly examined for coats. The only study relates to composite CT-aC particles possessing a carbonaceous phase incorporating traces of $CaCO_3$ and CT-$CaCO_3$ particles both of which have been examined for their effect on proliferation, osteoblastic differentiation and mineralization of bone marrow stromal cells (Table 19 [178]).

### 4.2. Nano and micro composite coats

Nano and micro composite CT coats can exist as thin composite layers or thin juxtaposed layers of CT and another material assembled into double or multiple layer coats. There are several potential applications and effects of such CT composite coats which are compiled in Table 20.

Photoelectrochemical splitting of water for generating molecular

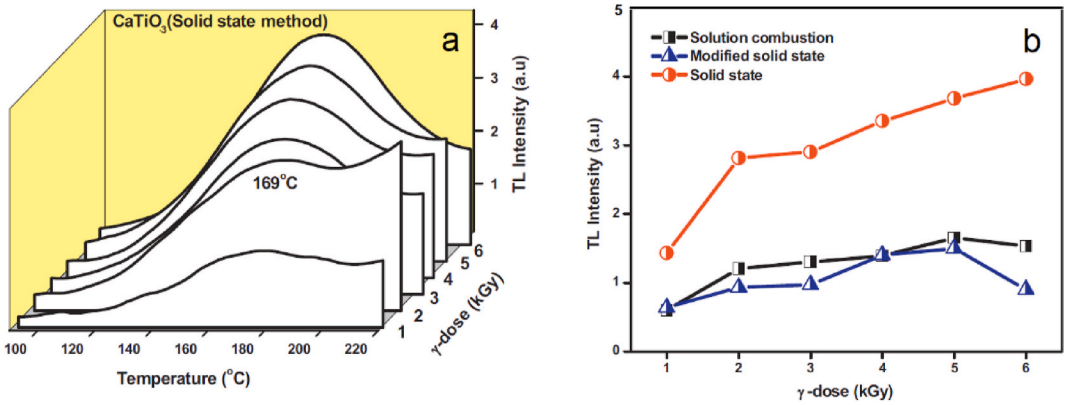


**Fig. 30.** TL of CT particles obtained by heating solid binary mixture (a) and variation of TL glow peak intensity of CT particles obtained by three different procedures (b). Reproduced from ref. 18, Copyright Elsevier.

hydrogen is considered to be a promising and low-cost way for solar energy conversion and micron-thick films composed of submicron and micron-sized anatase/CT particles deposited by CVD from Ca and Ti sources were shown to be useful photoanodes in photoelectrochemical cells [179].

Nafion (a sulfonated tetrafluoroethylene based fluoropolymer-copolymer) is a typical proton exchange membrane finding use in fuel cells and an incorporated non-stoichiometric calcium titanate $CaTiO_{3-\delta}$ possessing oxygen vacancies, aiding dissociative absorption of water, can act as a water retention additive which prevents a severe decrease in proton conductivity at higher temperatures caused by harmful water evaporation [180,181]. The CT nanocomposite can thus serve not only as a reinforcing additive but it can also facilitate the transfer of protons through the membrane and improve the overall fuel cell performance at high temperatures.

Magnesium alloys can find wide applications in orthopaedic implants provided that their surface is coated by a biocompatible layer decreasing their corrosion in *in vivo* conditions. A hydroxyapatite/calcium titanate/titanium dioxide/polylactic acid (HAp/CT/$TiO_2$/PLA) coating provides enhanced adhesion strength and corrosion resistance due to beneficial effect of $TiO_2$ transition layer and CT layer formed on the HA/$TiO_2$ interface by the reaction between HA and $TiO_2$ in the annealing $TiO_2$ process [182].

Ti alloys have relatively poor bone-forming properties and much attention was therefore given to enhance osteoconductivity of Ti and Ti alloys by modifying their surfaces. This effort encompassed fabrication of silicate-containing CT films with increased hydrophilicity [183], CT-incorporated β-$Ca_2SiO_4$ composite scaffold (Fig. 24 [184]), CT/$TiO_2$ [185–188] and CT/C [189,190] composite coats or Ti-implanted CT surface layers [191,192]. Hydroxyapatite (HAp) being a constituent of bone tissue and regarded as a nontoxic material was widely used as a suitable coat of Ti alloys. Its adhesion to Ti implants can be improved by using protective and bioconductive composite coats like a double CT-HAp layer [193], CT/HAp composite layer [194], CT/HAp double layer containing $TiO_2$ [135] or CT/α-tricalcium phosphate coat [195]. Surface biococonductivity was also examined with pressed pellets from nano/micro particles of CT and HAp and with phases of Ti nanoparticle-doped HAp or tricalcium phosphate both of which produced CT forms at their interface upon annealing [196,197].

Also Zr-based bulk metallic glasses (BMGs) are attractive as load-bearing biomedical implants due to high strength, relatively low Young's modulus and excellent biocompatibility and their surface was modified by laser cladding resulting in bioactive CT/Ca pyrophosphate layer whose main components respectively arise from high temperature reaction between Ti and HAp and from the HAp decomposition [198]. Hybride CT/chitosan scaffolds appear to promote the attachment, proliferation and biological function maintenance of Schwann cells, which is important in context of use of artificial nerve implants in human body [199].

Such list of different nanocomposite coats and their potential applications can be closed by noting better osseointegration properties of coatings containing CT together with an excess of calcium, which were ascribed to enhanced surface hydrophilicity and beneficial effect of Ca-incorporation [200–202].

## 5. Luminescence-structure relationship

Growing interest in nanotechnology involves searching for new phosphor materials with good photoluminescence (PL) and thermoluminescence (TL) properties. Certain attention was therefore also given to luminescence properties of nano and micro CT particles because of their potential technological application and the development of new luminescent materials. The PL of these species at room temperature occurs due to existing structural disorder of their solid system. It occurs neither in totally disorderd nor in totally ordered systems but requires some degree of structural order and some extent of structural disorder.

CT powders present interesting PL properties at room temperature, which are dependent on the structural organization level, preparation method and heat treatment conditions. On the other hand, the PL behavior of CT powders is a sensitive probe for the detection of their structural disorder of the titanium environment in crystalline phase. The luminescence of quasi-amorphous CT structures obtained by the polymeric precursor (Pechini) method was accounted for by the presence of distorted $[TiO_6]$–$[TiO_5]$ complex clusters but also by the structural disorder in the calcium site, which increases PL intensity and is due to charge exchanges between $Ca–O_{11}$ and $Ca–O_{12}$ clusters and intermediate levels in the gap state [203].

The powders obtained by the sol gel polymer precursor approach, annealed at different temperatures and subsequently irradiated with microwaves [68] showed a higher degree of structural organization, but they are less or not luminescent than those annealed without microwave irradiation, which are better PL emitters due to structural disorder at long and short range. This is caused by structural and surface defects believed to consist in oxygen vacancies in complex $[TiO_6]$-$[TiO_6]$ clusters or twists in bonding between these clusters.

PL was used to characterize the bottom-up process of the perovskite phase of nanoparticles produced by hydrothermal microwave route in order to deduce on the nature of generated CT mesocrystals [92]. The photoluminescent response covers a wide range of visible spectrum and consists of a broad luminescence band in the range of 350–580 nm and a band at 614 nm (Fig. 25). It is allocated to B1 and B2 (blue components), followed by a G3 (green component), a Y4 (yellow component), and a O5 (orange component) and reflects a close relation between a random polycrystalline distortion in the structure of nanoparticles, which can be

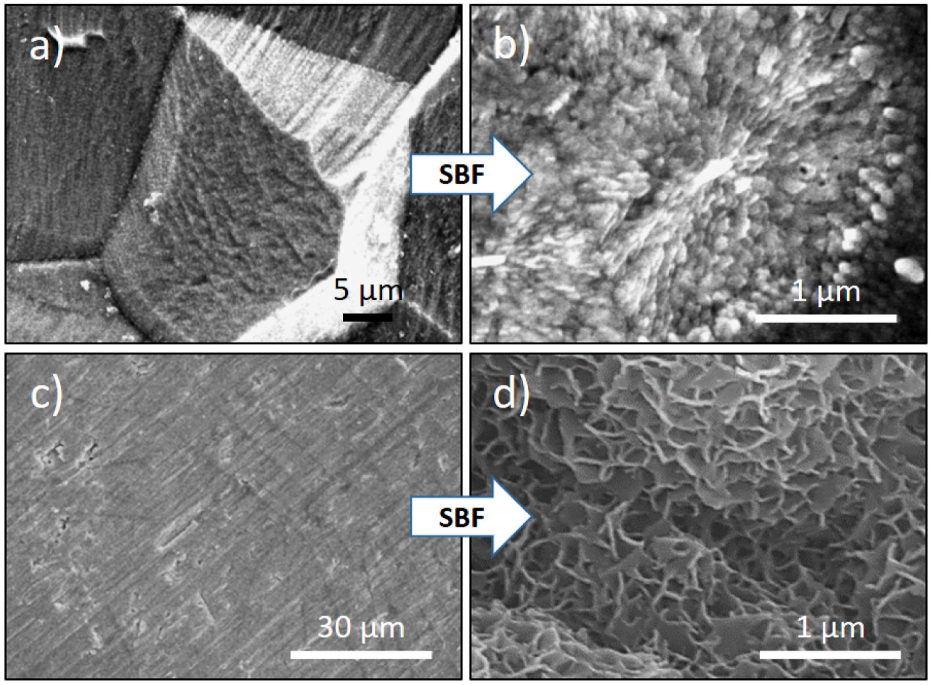


**Fig. 31.** SEM images of pristine and Ca phosphate modified CT surface; a, b (reproduced from ref. 143, Copyright Elsevier) and c, d (reproduced from ref. 200, Copyright Elsevier).

associated with the tilting (α angle < O–Ti–O) between adjacent $TiO_6$ octahedra (intermediate range) and the presence of intermediate energy states within the band gap which are claimed to be mainly responsible for the photoluminescence emissions.

PL was also used to examine whether different Ti source compounds ($TiCl_4$ or $Ti(OC_3H_7)_4$) can effect the development of the structure of CT nanoparticles prepared by microwave assisted hydrothermal route [93]. The different PL profiles and intensities (Fig. 26) were explained by the disorder coupled to the oxygen vacancies of $[TiO_5]$–$[TiO_6]$ in complex clusters in particles obtained from Ti isopropoxide and by twists in bonding between the $[TiO_6]$–$[TiO_6]$ complex clusters in particles obtained from Ti chloride.

Photoluminescent network-like hierarchical CT nanostructures built from 1D nanowires with oxygen vacancies were successfully synthesized through a hydrothermal route assisted by PVA surfactant and these powders have yellow appearance conversely to white and large irregular square-like structures obtained through the same procedure without PVA (Fig. 27 [100]). The yellow (Y) particles exert less intense photoluminescence than white (W) particles, which has been related to less recombination and more efficient migration of photogenerated charge carriers to the particle surface which also acts as visible light photocatalyst inducing water cleavage.

CT nanoparticles prepared by lower-temperature solid state synthesis **[39]** exhibit a strong and broad emission in the range of 527–568 nm (Fig. 28) and may be used as a green luminescent material. Such PL is ascribed to vacancies, "broken" surface or dangling bonds and other defect centers.

The hollow perovskite mesocubes (cubic boxes) have been grown by PEG-controlled solvothermal route in which PEG molecules appear to play a crucial role in the growth of the twinned, textured and hollow cubic nanostructures **[101]**. The box walls are neither single-crystalline, nor polycrystalline with strong preferred orientation, but are assembled by 3D perpendicular neighboring domains. These hollow mesocubes with high photoluminescence were formed in PEG but not in a PEG-10% water mixture when smooth prisms were formed instead (Fig. 29).

The crystalline CT nanoparticles prepared by solid state reactions and solution combustion in Ref. [18] were also investigated for their thermoluminescence (TL) after exposing to γ-radiation. It was observed that the thermoluminescence intensity for all the particle types is dependent on temperature and has similar profiles with broad peaks at 169 °C like shown for the particles prepared by heating the binary solid mixture (Fig. 30 a). The peak intensities were compared for all the nanoparticle types; they increase sublinearly with γ-dose (Fig, 30 b) and reveal the highest TL glow peak for the nanoparticles prepared by heating the binary solid mixture. It was also presumed that the observed glow peaks can be ascribed to oxygen vacancies.

Much previous interest has been also related to luminescence features of CT hosting trivalent rare-earth ions where the substitution of $Ca^{2+}$ sites results in the formation of $Ca^{2+}$ vacancies and consequently affects the 4f-4f transitions and upconversion luminescence properties. These rare-earth ions-doped CT materials are outside the scope of the current review.

## 6. Induction of calcium phosphates formation

Certain CT particles or coats noted in this review have been tested for their bioactivity by monitoring the growth of Ca phosphate/hydroxyapatite-like structures on their surfaces immersed in simulated body fluids (SBF). However, these fluids [204] are mere aqueous inorganic solutions mimicking the composition and ionic strength of the human extracellular fluid and can only induce the formation of nanospheres of X-ray-amorphous calcium phosphates instead of different biological apatites which grow in the presence of biological species in blood plasma and have a paracrystalline, carbonated and non-stochiometric nature. Such criterion of bioactivity proposed by Kokubo [205] and broadly used in many his and other studies of various Ti- and Si- based, inorganic ceramic or other surfaces [203] provides at best insufficient information and cannot be used as a sound bioactivity predictor [206], because hydroxyapatite or Ca phoshpate (CaP) formation is not principally controlled by biological processes but by physicochemical interactions of surfaces with components of supersaturated solutions. These interactions may, however, alter properties of the immersed surfaces and the observed Ca apatite/hydroxylapatite growth may proceed through different specific interactions of surface with SBF

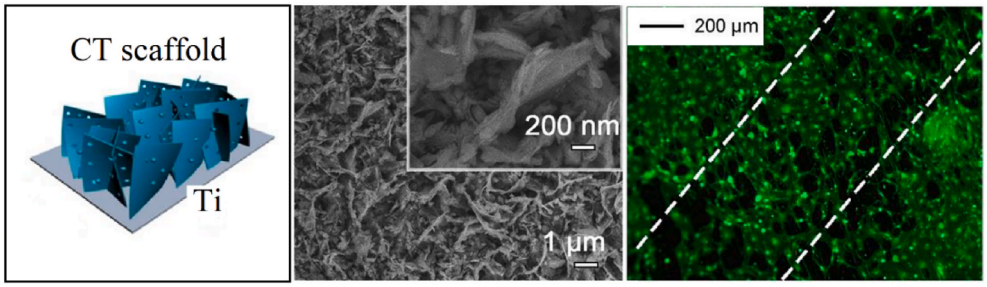


**Fig. 32.** Scheme and SEM image of CT scaffold with fluorescence images of migration of MC3T3-E1 cells (reproduced from ref. 144, Copyright Elsevier).

components and different mechanisms. As for these interactions, they can be clarified by refining published data on the performance of CT coats in water and SBF, but these data are at present scarce.

CT solubility in water is quite low at ambient temperature (<0.3 mg/L at 25 °C and pH 7.59) but is higher in hot water where CT surface releases Ca and develops a topmost nm-sized anatase layer and where the Ca release is decelerated by added $Ca^{2+}$ ions [207,208].

Similar type of dissolution was also observed in SBF with μm-sized amorphous or less crystallized CT coats deposited on a glassy carbon or an Si wafer. These coats deposited by CT sputterring or by Ti ion beam assisted-CT sputtering involving Ti implantation did not release Ti but Ca and the former released more Ca than the latter, which was ascribed to a more stable Ti-implanted outmost CT surface layer [191,192]. Nonetheless, just 50 nm thick coats prepared by only CT sputtering and additionally heated or heated during sputtering are durable in SBF and develop apatite films more efficiently if heated in air and not in vacuum [118]. The CT coats produced by the hydrothermal–electrochemical method on Ti or Ti6Al4V induce formation of apatite, which is not observed for the uncoated Ti and Ti6Al4V samples [143]. The CT coats with dense polycrystalline structure produced by sol-gel route on Si wafers [146] show higher ability to develop apatite than their amorphous counterparts which form cracks in SBF. The nanocomposite CT/$TiO_2$ surface layers on titanium produced by heating Ti plate in aqueous $Ca(OH)_2$ slurries [185,186] exert different ability to grow apatite in SBF; those richer in CT promote Ca phosphate growth more effectively than those richer in $TiO_2$. Dissimilar ability to grow apatite was also observed with CT coats on Ti6Al4V anode produced by plasma electrochemical oxidation of Ca salts-containing electrolytes and performed without and with additional alkali heat treatment [187,188]. The unheated amorphous (denoted as a $TiO_2$-based) coat possessed more Ca in the outmost layer but lower ability to grow apatite than the heated crystalline CT coat. However, these differences were not duly explained in terms of different morphologies or different effects of Ca contents. The CT coats deposited on heated quartz glass by metalloorganic CVD method allows faster apatite deposition when produced at 800 °C and slower deposition when produced at 600 °C, which is a consequence of different morphologies and/or different degree of contamination by $TiO_2$ and $Ca(OH)_2$ [127,128,209]. Formation of unspecified Ca phosphate was also reported for hydrophilic nanolamellate CT microstructures submerged in Hanks' solution and ascribed to corrosion of these entities [210].

There are several proposals on the mechanism of CT interactions in SBF, which are more or less only speculations on a sequence of two events. These are electrostatic interactions between calcium or phosphate ions with CT surface (formation of Stern layer) and a subsequent interaction with counterion to form Ca phosphate. The only conlusive proposal is based on a detailed experimental examination of separate calcium leaching from CT surface and phosphate adsorption experiments performed with commercial CT suspensions and using Zeta potential measurements at different pH [211]. It was deduced that phosphate ions are not adsorbed only on Ca sites but also on $TiO_2$ surface entities developed after calcium leaching from CT surface. However, the mechanism appears even more complex due to conceivable surface heterogeneities, different nature of diverse nano/micro morphologies noted throughout the review and even different effects of exposed (110), (011) and (001) topmost facets with different (Ca, TiO, O or $TiO_2$) terminations. These last structural features have been explored in theoretical calculations [212,213].

To this end, the growth of calcium apatite on various CT surfaces is faster or slower and although it is well detected (Fig. 31), its complex mechanism still remains to be utterly elucidated. After CT dissolution

$$CaTiO_3(s) + H_2O \rightarrow Ca^{2+}(aq) + TiO_2(s) + 2\ HO^-(aq)$$

many electrostatic interactions between $Ca^{2+}$ and $OH^-$ ions and solid CT and $TiO_2$ sites can occur in the initial stage and may later compete with the growth of Ca apatite and its dissolution and a re-growth. Nonetheless, in some stages the CT/$TiO_2$ surface becomes covered with a thin Ca phosphate layer and once this happens the growth of Ca phosphate should be necessarily controlled by the combination of Ca and phosphate ions in the bulk solution and may be aided by the formed Ca phosphate surface.

## 7. Effects on osseointegration with bone tissue

Further on we give a cautious comment on CT and CT nanocomposites osseointegration and before that we repeat that CT can very slowly dissolve in water and aqueous solutions and after leaching Ca change the CT structure of its topmost layer by forming $TiO_2$ sites (Section 6). These surface changes may play a role in processes occurring on CT surface immersed in physiological fluids despite that CT is considered to serve as a protective layer against corrosion.

### 7.1. $CaTiO_3$

The bio properties of CT and composite CT films noted in this review were revealed from *in vitro* and *in vivo* studies aimed at improved osseointegration of titanium substrates immersed in artificial physiological environments or surgically inserted in animal tissues. To begin this section, we should first give a short comment on osseointegration of Ti-based surfaces.

The osseointegration of Ti surface is a complex process controlled by primary bone remodeling (formation and resorption) which is effected by mesenchymal stem cells (MSCs), osteoblasts (OBs), osteoclasts (OCs) and osteoclast precursors [214]. In the course of this process, implant surface properties influence the fates of MSCs and OBs which form an osteogenic environment, while OCs regulate MSCc migration and degrade primary bone by creating conditions enabling OBs to create and calcify their matrix [215,216]. In this process, $Ca^{2+}$ ions promote the differentiation of bone cells and the mineralization of new bone [217], influence the adhesion and differentiation behavior of osteoblasts through Ca signaling pathway [218] and promote proliferation and migration of MSCs by increasing osteopontin expression [219]. Special effects on osseointegration are also exerted by micro/nano structured surfaces which can promote bonding with bone due to the surface

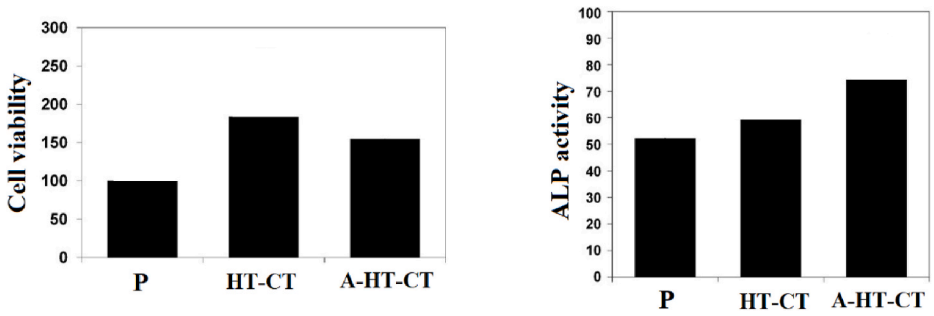


**Fig. 33.** MC3T3-E1 cell viability and alkaline phosphatase (ALP) activity on pristine (P), HT-CT and A-HT-CT treated surfaces of Ti13Nb13Zr alloy. Adapted from ref. 201, Copyright Elsevier.

interaction with ions, biomolecules and cells, thereby enhancing protein adsorption and cell adhesion, proliferation and differentiation toward specific lineages, but may also trigger diverse cell behavior and lead to adverse effects on osteogenic lineage differentiation and tissue integration with titanium implant.

The osseointegration of Ti surfaces with unavoidable oxidic topmost layer can be enhanced on hydrophilic and porous surfaces, on surfaces with micro- or mico/nano topography (e.g. Refs. [220–224]) and also by of $Ca^{2+}$ ions which enhance the osteoconductivity by stimulating the response of pre-osteoblasts cells [225], increase the growth rate of MC3T3-E1 cells [226] and promote adhesion, proliferation and early differentiation of MG63 cells [227]. However, it was also shown that Ca $(OH)_2$-treated titanium surfaces induce osteogenic differentiation in hMSCs, whereas $CaCl_2$ treatment had only a limited effect and these differences were ascribed to different amounts of calcium ions and apatite formation in both treatments [228]. It is also known that some nanostructured surfaces having specific charge density and/or hydrophilicity can promote cells' response and bone formation, while other specific nanostructured surfaces may exert a potential of hidden danger for the application of nanostructured implants.

As for osseointegration of CT surfaces, there is a misleading information in introduction of [144] affirming that CT can significantly promote adhesion of osteoblast and enhance the osseointegration. It is based on a wrong understanding of the cited results [178] which reveal that proliferation, osteoblastic differentiation, and mineralization of KUSA/A1 cells cultured on nanocomposite CT–$CaCO_3$ and CT-aC particles are greater than on CT nanoparticles. These cited results therefore indicate that $CaCO_3$ and aC constituents can play a key role in the cell response of the CT-$CaCO_3$ and CT-aC particles.

#### 7.1.1. *In vitro studies*

All present studies of capability of CT coats to enhance osseointegration with bone tissue suffer from the fact that CT entities coming into contact with physiological solution are not pure but combined with other constituents, which is the reason why the discrete effect of single CT cannot be well evaluated.

The hydrophilic CT-microshield scaffold promotes adhesion, migration, proliferation and differentiation of MC3T3-E1 cells more than does Ti foil [144], but such effect cannot be completely assigned to effect of neat CT. Such scaffold (Fig. 32) was characterized by XRD, Raman and EDS analyses and claimed to be composed of mere CT and Ti entities, but was not verified by XPS and its EDS corresponding to $CaTi_{2.63}O_{5.70}$ stoichiometry reveals that the sample contains a substantial amount of amorphous Ti oxide(s).

The hydrophilic CT film of unspecified elemental composition on Ti enhances differentiation of mouse bone marrow stromal ST-2 cells but not their proliferation as compared to the uncoated Ti surface [129]. The crystalline CT coatings with an XRD-observed TiO constituent on Ti screws increase proliferation and ALP activity of MC3T3-E1 cells more than uncoated titanium surface of screws [136].

The above examples thus do not provide any chance for discussion of specific reasons of increased bioactivity of CT coats, because several effects like $Ca^{2+}$ ions or different hydrophilicity and stem cells encapsulation ability of hydrated CT and oxidic Ti surface sites can be involved.

#### 7.1.2. *In vivo studies*

Histological observations of pristine Ti sample and a 50 nm thick crystalline CT-coated Ti samples surgically inserted in both soft and hard rat tissues revealed better new bond formation and a slight inflammatory reaction but no degeneration or necrosis on the coated sample, which was ascribed to an enhancement of new bone growth by a stable CT coat, since Ca/Ca + Ti depth profile, derived by AES, did not change within immersion time of 14 days in a 0.8% NaCl solution [117]. Similar positive effect on osteointegration was also observed for CT-microshield scaffold [144], implanted in the mice, when the comparison with implanted (oxidic) Ti sample revealed more new and regenerated bone tissues with trabeculae and matrices on CT-microshield scaffold. However, the scaffold composed of CT microshields accommodated on a platform obviously consisting of CT and oxidic Ti cannot be considered a pure CT. ESEM images of CT-coated Ti screws seemed to readily combine with the bone tissue and the uncoated screws did not, but the CT coat includes a minor TiO contribution [136].

### 7.2. *$CaTiO_3$ nanocomposites*

The superhydrophilic CT/$SiO_3^{2-}$ coat with a very low water contact angle shows higher fibronectin and albumin adsorption and better contact with tissue in rats' tibia when compared to the coat without incorporated $SiO_3^{2-}$ [183]. These advanced properties may be associated with increased hydrophilicity or specific interactions between $SiO_3^{2-}$ groups and the proteins.

Nanocomposite CT/$CaCO_3$ and CT-aC particles (containing small amounts of $CaCO_3$) show better proliferation, osteoblast differentiation and mineralization of bone marrow stromal cells than CT nanoparticles [178] and similar positive effect is also observed for the CT-aC coat which induces enhanced MT3T3-E1 cell attachment, proliferation, and osteoblastic differentiation when compared to HAp coat [190]. Disentangling this effect is difficult since calcium carbonate nanoparticles have slight effect on viability of human bone-marrow mesenchymal stem cells (hBMSCs) but significantly promote their osteogenic differentiation [229] and nanostructured HAp ceramics promotes MC3T3-E1 osteoblast growth and osseogenic differentiation [230].

CT interlayer between biocompatible HAp layer coated on titanium substrate decreases dissolution of HAp in human extracellular fluid and annealing [194] or laser scanning [195] of joint HAp and Ti layers induces reaction between HAp and Ti to yield a nanocomposite CT layers. Such layer was thought responsible for higher human osteoblasts adhesion on titanium coated with HAp and annealed in air as compared to Ti or HAp surfaces [194]. The laser-produced adhesive nanocomposite networks of CT with calcium phosphates and minor CaO on Ti surface exert higher MG63 osteosarcoma-like cells proliferation than

pristine (laser-untreated) HAp layers and this difference is related to CT or CaO effect. Homogeneously distributed μm-sized CT and HAp particles on surfaces of pellets pressed from CT and HAp microparticles of various proportions promote adhesion and proliferation of L929 fibroblast cells and SaOS2 osteoblast cells in a very similar fashion, which was explained by good and similar cellular functionality of both HAp and CT microphases [196]. Different view on the relative bioactivity of HAp and CT phases has been acquired in studies of adhesion of human CRL-11372 osteoblasts on pellets composed of homogeneously distributed nanoparticles of CT-HAp and CT-TCP (tricalcium phosphate) mixtures [197]. Osteoblast adhesion was significantly greater on the HAp-CT composites and TCP-CT composites than on pure HAp and the highest adhesion was observed on TCP-CT composite containing slight amount of tetracalcium hydrogen phosphate ($Ca_9HPO_4(PO_4)_5OH$) phase, although it was admitted that enhanced osteoblast adhesion may be due to increasing shrinkage in the unit lattice parameters and decreasing grain size occurring in the course of pellets fabrication.

Also with these nanocomposite systems a distintion between effects of CT and HAP or CT and TCP awaits to be carried out, because it is known that HAp [231,232] and tricalcium phosphate [233] are bioactive and also capable of enhancing attachment, proliferation and differentiation of osteoblasts. Furthermore, it is possible that not only surface chemistries but also nanostructure topography of the nanocomposites plays a crucial role as has been confirmed for thin calcium phosphate films replicating underlying nanostructured island-shaped grain topography of $TiO_2$ substrate [234].

Hydrophilic Ca-incorporated crystalline CT-anatase film on Ti6Al4V and Ti13Nb13Zr alloy surface show viability and enhanced differentiation of pre-osteoblast MC3T3-E1 cells and better bone-to-implant contact values as compared to pristine (hydrothermally untreated) Ti6Al4V and Ti13Nb13Zr alloy implants [200–202]. These differences were explained by the effect of copious Ca ions in Ti oxidic layer stimulating integrin-mediated osteoblast response through enhanced ligand binding of the integrin receptor and not by participation of CT phase. Different features observed for pristine Ti13Nb13Zr surface and hydrothermally (HT) grown and additionally in air annealed (A) CT films on Ti13Nb13Zr alloy are illustrated in Fig. 33.

An interesting example of nano CT composite are also scaffolds of mainly orthorhombic CT nanoparticles associated with amorphous phase of chitosan, which could obviously promote the attachment, proliferation and biological function maintenance of Schwann cells and might be of importance in peripheral nerve regeneration [199].

## 8. Conclusion

Nano- and micro-sized CT particles and coats and their composite counterparts of different phase, size, shape, morphology and arrangement of subunits were prepared by various classes of solid state reactions, wet chemical routes and physical methods and were broadly explored for their potential use as phosphors, adsorbents, catalysts, inducers of biomimetic calcium phosphate formation, UV and Vis photocatalysts of water splitting and degradation of pollutants in aquatic environment, and promoters of osseointegration of titanium implants with bone.

Apart from these uses in these fields of major interest, some of these forms were resolved as advanced electrochemical sensor/biosensor, piezoelectric ceramics, dielectric low-loss properties ceramics, corrosion resistant film, biodegradable elastomer, microwave-assisted photoluminescent particle, low temperature ferroelectric epitaxial layer or dye-sensitized solar cell.

CT powders present interesting PL properties at room temperature, which are dependent on the structural organization level, preparation method and heat treatment conditions. On the other hand, the PL behavior of CT powders is a sensitive probe for the detection of their structural disorder of the titanium environment in crystalline phase.

Certain CT particles or coats appear to induce biomimetic formation of calcium phosphate from simulated body fluids and the mode of apatite/hydroxylapatite growth on their surfaces was refined on the basis of the performance of CT coats in water and SBF.

Osseointegration properties of CT and composite CT forms noted in *in vitro* and *in vivo* studies were discussed in terms of behaviour of these forms in water or SBF and possible effects of nano/micro topography, CT sites and composite components.

The minute slow dissolution of topmost CT layers in aquatic media (water, SBF) indicating hydrolytic instability of CT surface may have serious impact on interpretation of CT bioactivity and physicochemical, catalytic and photocatalytic properties of CT surface immersed in aqueous solutions, which has not been admitted in previous studies.

## Declaration of competing interest

The authors declare that they have no known competing financial interests or personal relationships that could have appeared to influence the work reported in this paper.

## Acknowledgements

This work was supported by the project n. 201 ”Advanced porous biomaterials functionalized with stem cells for enhancing of osseointegration of implants: MATEGRA” realised within the frame of the Program IN-TERREG V-A: Cross-border cooperation between the Czech Republic and the Federal State of Germany Bavaria, Aim European Cross-border cooperation 2014–2020. The realisation is supported by financial means of the European Regional Development Fund (85% of the costs) and the state budget of the Czech Republic (5%).

Note: The images in Figure Captions with cited references were reproduced with permissions from the Copyright owners.

## References

[1] V.V. Lemanov, A.V. Sotnikov, E.P. Smirnova, M. Weihnacht, R. Kunze, Perovskite CaTiO3 as an incipient ferroelectric, Solid State Commun. 110 (1999) 611, https://doi.org/10.1016/S0038-1098(99)00153-2.

[2] A. Linz Jr., K. Herrington, Electrical and optical properties of synthetic calcium titanate crystal, J. Chem. Phys. 28 (1958) 824, https://doi.org/10.1063/1.1744278.

[3] A. Fereira, Negative temperature coefficient resistance (NTCR) ceramic thermistors: an industrial perspective, J. Am. Ceram. Soc. 92 (2009) 967–983, https://doi.org/10.1111/j.1551-2916.2009.02990.x.

[4] H.F. Kay, P.C. Bailey, Structure and properties of CaTiO3, Acta Crystallogr. 10 (1957) 219–226, https://doi.org/10.1107/S0365110X57000675.

[5] S.A.T. Redfern, High-temperature structural phase transitions in perovskite (CaTiO3), J. Phys. Condens. Matter 8 (1996) 8267–8275, https://doi.org/10.1088/0953-8984/8/43/019.

[6] T. Nakamura, P.-H. Sun, Y.J. Shan, Y. Inaguma, M. Itoh, I.-S. Kim, J.-H. Sohn, M. Ikeda, T. Kitamura, H. Konagaya, On the perovskite-related materials of high dielectric permittivity with small temperature dependence and low dielectric loss, Ferroelectrics 196 (1997) 205–209, https://doi.org/10.1080/00150199708224163.

[7] X.S. Wang, C.N. Xu, H. Yamada, K. Nishikubo, X.G. Zheng, “Electro-mechano-optical conversions in $Pr_{3+}$–doped $BaTiO_3$–$CaTiO_3$ ceramics, Adv. Mater. 17 (2005) 1254–1258, https://doi.org/10.1002/adma.200401406.

[8] S. Tariq, A. Ahmed, S. Saad, S. Tariq, Structural, electronic and elastic properties of the cubic CaTiO3 under pressure: a DFT study, AIP Adv. 5 (2015), 077111, https://doi.org/10.1063/1.4926437.

[9] E. Cockayne, B.P. Burton, Phonons and static dielectric constant in $CaTiO_3$ from first principles, Phys. Rev. B 62 (2000) 3735–3743, https://doi.org/10.1103/PhysRevB.62.3735.

[10] M. Yashima, R. Ali, Structural phase transition and octahedral tilting in the calcium titanate perovskite $CaTiO_3$, Solid State Ionics 180 (2009) 120–126, https://doi.org/10.1016/j.ssi.2008.11.019.

[11] R. Ali, M. Yashima, Space group and crystal structure of the Perovskite $CaTiO_3$ from 296 to 1720 K, J. Solid State Chem. 178 (2005) 2867–2872, https://doi.org/10.1016/j.jssc.2005.06.027 and refs. therein.

[12] M. Yashima, R. Ali, Structural phase transition and octahedral tilting in the calcium titanate perovskite $CaTiO_3$, Solid State Ionics 180 (2009) 120–126, https://doi.org/10.1016/j.ssi.2008.11.019.

[13] B.J. Kennedy, C.J. Howard, B.C. Chakoumakos, Phase transitions in perovskite at elevated temperatures—a powder neutron diffraction study, J. Phys. Condens. Matter 11 (1999) 1479–1488, https://doi.org/10.1088/0953-8984/11/6/012.

[14] M.O. Ramirez, T.T.A. Lummen, I. Carrasco, E. Barnes, U. Aschauer, D. Stefanska, A.S. Gupta, C. de las Heras, H. Akamatsu, M. Holt, P. Molina, A. Barnes, R.

C. Haislmaier, P.J. Deren, C. Prieto, L.E. Bausá, N.A. Spaldin, V. Gopalan, Emergent room temperature polar phase in $CaTiO_3$ nanoparticles and single crystals, Apl. Mater. 7 (2019), 011103, https://doi.org/10.1063/1.5078706.
[15] I. Fatimah, Y. Rahmadianti, R.A. Pudiasari, Photocatalyst of perovskite CaTiO3 nanopowder synthesized from CaO derived from snail shell in comparison with the use of CaO and CaCO3, IOP Conf. Ser. Mater. Sci. Eng. 349 (2018), 012026, https://doi.org/10.1088/1757-899X/349/1/012026.
[16] S.S. Gaikwad, A.V. Borhade, V.B. Gaikwad, A green chemistry approach for synthesis of CaTiO3 Photocatalyst: its effects on degradation of methylene blue, phytotoxicity and microbial study, Der Pharma Chem. 4 (2012) 184–193. http://derpharmachemica.com/archive.html.
[17] G. Gralik, A.E. Thomsen, C.A. Moraes, F. Raupp-Pereira, D. Hotza, Processing and characterization of $CaTiO_3$ perovskite ceramics, Process. Appl. Ceram. 8 (2014) 53–57, https://doi.org/10.2298/PAC1402053G.
[18] M. Shivaram, R. H Krishna, H. Nagabhushana, S.C. Sharma, B.M. Nagabhushana, B.S. Ravikumar, N. Dhananjaya, C. Shivakumara, J.L. Rao, R.P.S. Chakradhar Synthesis, characterization, EPR and thermoluminescence properties of CaTiO3 nanophosphor, Mater. Res. Bull. 48 (2013) 1490–1498, https://doi.org/10.1016/j.materresbull.2012.12.065.
[19] A. Kawashima, K. Matsubara, K. Honda, Development of heterogeneous base catalysts for biodiesel production, Bioresour. Technol. 99 (2008) 3439–3443, https://doi.org/10.1016/j.biortech.2007.08.009.
[20] K.S. Venkataraman, K.S. Narayanan, Energetics of collision between grinding media in ball mills and mechanochemical effects, Powder Technol. 96 (1998) 190–201, https://doi.org/10.1016/S0032-5910(97)03368-8.
[21] M.J. Jaycock, G.D. Parfitt, Chemistry of Interfaces, Ellis Horwood, Chichester, 1981, https://doi.org/10.1002/bbpc.19810850925. Chap. 4.
[22] G.I. Finch, K.P. Sinha, Proc. R. Soc. London, Ser. A. 239 (1957) 145.
[23] N.J. Welham, Mechanically induced reaction between alkaline earth metal oxides and TiO2, J. Mater. Res. 13 (1998) 1607–1613, https://doi.org/10.1557/JMR.1998.0221.
[24] G. Brankovic, V. Vukotic, Z. Brankovic, J.A. Varela, Investigation on possibility of mechanochemical synthesis of CaTiO3 from different precursors, J. Eur. Ceram. Soc. 27 (2007) 729–732, https://doi.org/10.1016/j.jeurceramsoc.2006.04.051.
[25] S. Manafi, M. Jafarian, Synthesis of perovskite CaTiO3 nanopowders with different morphologies by mechanical alloying without heat treatment, Int. J. Phys. Sci. 8 (2013) 1277–1283. http://www.academicjournals.org/IJPS.
[26] S. Manafi, M. Jafarian, Determining the optimal conditions for calcium titanate nanostructures synthesized by mechanical alloying method, Adv. Ceram. Prog. 1 (2015) 11–16, https://doi.org/10.30501/ACP.2015.69994.
[27] S.K. Manik, S.K. Pradhan, Microstructure characterization of ball milled prepared nanocrystalline perovskite CaTiO3 by Rietveld method, Mater. Chem. Phys. 86 (2004) 284–292, https://doi.org/10.1016/j.matchemphys.2004.03.010.
[28] S. Palaniandy, N.H. Jamil, Influence of milling conditions on the mechanochemical synthesis of CaTiO3 nanoparticles, J. Alloys Compd. 476 (2009) 894–902, https://doi.org/10.1016/j.jallcom.2008.09.133.
[29] G. Mi, F. Saito, S. Suzuki, Y. Waseda, Formation of CaTiO3 by grinding from mixtures of CaO or Ca(OH)2 with anatase or rutile at room temperature, Powder Technol. 97 (1998) 178–182, https://doi.org/10.1016/S0032-5910(98)00012-6.
[30] G. Mi, Y. Murakami, D. Shindo, F. Saito, Microstructural investigation of CaTiO3 formed mechanochemically by dry grinding of a CaO–TiO2 mixture, Powder Technol. 104 (1999) 75–79, https://doi.org/10.1016/S0032-5910(99)00045-5.
[31] V.M. Vukotić, N. Radojević, L. Živković, Z. Vuković, B.D. Stojanović, Mechanically activated synthesis of CaTiO3 from mixture of CaO and $TiO_2$, Mater. Sci. Forum 494 (2005) 393–398. https://doi.org/10.4028/www.scientific.net/msf.494.393.
[32] B. Tyliszczak, K.Z. Gaca, A. Sobczak-Kupiec, P. Dulian, Mechanochemical synthesis and investigations of calcium titanate powders and their acrylic dispersions, J. Eur. Ceram. Soc. 34 (2014) 2259–2264, https://doi.org/10.1016/j.jeurceramsoc.2014.02.020.
[33] S. Sahoo, Negative temperature coefficient resistance of $CaTiO_3$ for thermistor application, Trans. Electr. Electron. Mater. 21 (2020) 91–98, https://doi.org/10.1007/s42341-019-00159-x.
[34] K. Wieczorek-Ciurowa, P. Dulian, A. Nosal, J. Domagała, Effects of reagents' nature on mechanochemical synthesis of calcium titanate, J. Therm. Anal. Calorim. 101 (2010) 471–477, https://doi.org/10.1007/s10973-010-0802-0.
[35] V. Berbenni, A. Marini, Mechanical activation of calcium titanate formation from $CaCO_3$ $TiO_2$ mixtures, J. Mater. Sci. 39 (2004) 5279–5282, https://doi.org/10.1023/B:JMSC.0000039228.02104.63.
[36] I.R. Evans, J.A.K. Howard, T. Srecković, M.M. Ristić, Variable temperature in situ X-ray diffraction study of mechanically activated synthesis of calcium titanate, CaTiO3.Mater. Res. Bull. 38 (2003) 1203–1213, https://doi.org/10.1016/S0025-5408(03)00113-2.
[37] Z. Kesić, I. Lukić, M. Zdujić, Č. Jovalekić, V. Veljković, D. Skala, Assessment of $CaTiO_3$, $CaMnO_3$, $CaZrO_3$ and $Ca_2Fe_2O_5$ perovskites as heterogeneous base catalysts for biodiesel synthesis, Fuel Process. Technol. 143 (2016) 162–168, https://doi.org/10.1016/j.fuproc.2015.11.018.
[38] V.M. Vukotic, T. Srekovic, Z.V. Marinkovic, G. Brankovic, M. Cilense, D. Arandjelovic, Mechanochemical synthesis of CaTiO3 from CaCO3 - TiO2 mixture, Mater. Sci. Forum 453–454 (2004) 429–434. https://doi.org/10.4028/www.scientific.net/MSF.453-454.429.
[39] J. Li, Y.C. Zhang, T.X. Wang, M. Zhang, Low temperature synthesis and optical properties of $CaTiO_3$ nanoparticles from $Ca(NO_3)_2{\cdot}4H_2O$ and TiO2 nanocrystals, Mater. Lett. 65 (2011) 1556–1558, https://doi.org/10.1016/j.matlet.2011.03.031.
[40] L. Wang, J. Li, M. Feng, L. Min, J. Yang, S. Yu, Y. Zhang, X. Hu, Z. Yang, Perovskite-type calcium titanate nanoparticles as novel matrix for designing sensitive electrochemical biosensing, Biosens. Bioelectron. 96 (2017) 220–226, https://doi.org/10.1016/j.bios.2017.05.004.
[41] X. Lei, B. Xu, B. Yang, B. Xu, X. Guo, A novel method of synthesis and microstructural investigation of calcium titanate powders, J. Alloys Compd. 690 (2017) 916–922, https://doi.org/10.1016/j.jallcom.2016.08.213.
[42] T.H. Okabe, R.O. Suzuki, T. Oishi, K. Ono, Thermodynamic properties of dilute titanium-oxygen solid solution in beta phase, Mater. Trans., JIM 32 (1991) 485–488, https://doi.org/10.2320/matertrans1989.32.485.
[43] Y.X. Zhang, X.Y. Nai, M. Wei, D.H. Zhu, C.C. Zhu, W. Li, Preparation and characterization of calcium titanate (CaTiO3) whiskers via molten salt method, Adv. Mater. Res. 630 (2013) 89–92. https://doi.org/10.4028/www.scientific.net/amr.630.89.
[44] G. Pfaff, F. Schmidt, W. Ludwig, A. Feltz, $M^{II}TiO(C_2O_4)_2{\cdot}4H_2O$ ($M^{II}$=Mg, Ca, Sr or Ba) as precursors of the formation of $M^{II}TiO_3$ powders, J. Therm. Anal. 33 (1988) 771–779, https://doi.org/10.1007/bf02138586.
[45] B.M. Patil, R.S. Srinivasa, S.R. Dharwadkar, Synthesis of CaTiO3 from calcium titanyl oxalate hexahydrate (CTO) as precursor employing microwave heating technique, Bull. Mater. Sci. 30 (2007) 225–229, https://doi.org/10.1007/s12034-007-0040-7.
[46] Y. Deng, S. Tang, S. Wu, Synthesis of calcium titanate from $[Ca(H_2O)_3]_2[Ti_2(O_2)_2O(NC_6H_6O_6)_2].2H_2O$ as a cheap single source precursor, Solid State Sci. 12 (2010) 339–344, https://doi.org/10.1016/j.solidstatesciences.2009.11.010.
[47] R.P. Singh, Conventional and microwave synthesis of mesoporous calcium titanate nanopowders: a comparative study, J. Sol. Gel Sci. Technol. 88 (2018) 574–583, https://doi.org/10.1007/s10971-018-4860-2.
[48] D.A. Salinas, C.L. Marchena, L.B. Pierella, G. Pecchi, Catalytic oxidation of 2-(methylthio)-benzothiazole on alkaline earth titanates, ATiO3 (A = Ca, Sr, Ba), Mol. Catal. 438 (2017) 76–85, https://doi.org/10.1016/j.mcat.2017.05.019.
[49] H.S. Gopalakrishnamurthy, M.S. Rao, T.R.N. Kutty, Thermal decomposition of titanyl oxalates IV. Strontium and calcium titanyl oxalates, Thermochim. Acta 13 (1975) 183–191, https://doi.org/10.1016/0040-6031(75)80080-3.
[50] N.J. Ali, J. Bultitude, L.A. Xue, S.J. Milne, Preparation of stoichiometric MTiO3 a powders (M = Ba, Sr, Ca) from catecholate complexes, Mater. Res. Soc. Symp. Proc. 121 (1988) 269–274, https://doi.org/10.1557/PROC-121-269.
[51] Y. Saito, H. Takao, K. Wada, Synthesis of platelike $CaTiO_3$ particles by a topochemical microcrystal conversion method and fabrication of textured microwave dielectric ceramics, Ceram. Int. 34 (2008) 745–751, https://doi.org/10.1016/j.ceramint.2007.09.017.
[52] K.C. Patil, Advanced ceramics: combustion synthesis and properties, Bull. Mater. Sci. 16 (1993) 533–541, https://doi.org/10.1007/BF02757654.
[53] K.C. Patil, S.T. Aruna, T. Mimani, Combustion synthesis: an update, Curr. Opin. Solid State Mater. Sci. 6 (2002) 507–512, https://doi.org/10.1016/S1359-0286(02)00123-7.
[54] M. Muthuraman, N.A. Dhas, K.C. Patil, Combustion synthesis of oxide materials for nuclear waste immobilization, Bull. Mater. Sci. 17 (1994) 977–987, https://doi.org/10.1007/BF02757574.
[55] K. Manjunath, C.G. Thimmanna, Studies on synthesis, characterization and applications of nano $CaTiO_3$ Powder, Current Nanomaterials 1 (2016) 145–155, https://doi.org/10.2174/2405461501666160805125748.
[56] S. Lanfredi, F. Storti, L.P.M. Simões, E. Djurado, M.A.L. Nobre, Synthesis and structural characterization of calcium titanate by spray pyrolysis method, Mater. Lett. 201 (2017) 148–151, https://doi.org/10.1016/j.matlet.2017.05.001.
[57] G. Pfaff, Synthesis of calcium titanate powders by the **sol-gel** process, Chem. Mater. 6 (1994) 58–62, https://doi.org/10.1021/cm00037a013.
[58] R. Tamayo, R. Espinoza-González, F. Gracia, U.P. Rodrigues-Filho, M. Flores, E. Sacari, As(III) removal from aqueous solution by calcium titanate nanoparticles prepared by the sol gel method, Nanomaterials 9 (2019) 733, https://doi.org/10.3390/nano9050733.
[59] R. Naser, A. Zargar Kharazi, G. Dini, Fabrication of PGS/$CaTiO_3$ nano-composite for biomedical application, Int. J. Nanosci. Nanotechnol. 12 (2016) 103–108. http://www.ijnnonline.net/article_20406.html.
[60] S.A.U. Portia, S. Rajkumar, E. Elanthamilan, J.P. Merlin, K. Ramamoorthy, Effect of annealing temperature on structural, optical and visible light photocatalytic performance of $CaTiO_3$ catalysts synthesized by simple sol-gel technique, Inorg. Chem. Commun. 119 (2020) 108051, https://doi.org/10.1016/j.inoche.2020.108051.
[61] S.A. Hosseini, Preparation and characterization of calcium titanate nanoparticles with the aid of different acids and study of their photocatalytic properties, J. Mater. Sci. Mater. Electron. 28 (2017) 3703–3708, https://doi.org/10.1007/s10854-016-5976-1.
[62] C. Han, J. Liu, W. Yang, Q. Wu, H. Yang, X. Xue, Photocatalytic activity of $CaTiO_3$ synthesized by solid state, sol–gel and hydrothermal methods, J. Sol. Gel Sci. Technol. 81 (2017) 806–813, https://doi.org/10.1007/s10971-016-4261-3.
[63] T. Puangpetch, P. Sommakettarin, S. Chavadej, T. Sreethawong, Hydrogen production from water splitting over Eosin Y-sensitized mesoporous-assembled perovskite titanate nanocrystal photocatalysts under visible light irradiation, Int. J. Hydrogen Energy 35 (2010) 12428–12442, https://doi.org/10.1016/j.ijhydene.2010.08.138.
[64] M.P. Pechini, Method of preparing lead and alkaline earth titanates and niobates and coating method using the same to form a capacitor, U.S. Patent 3 (1967) 330–697.

[65] T. Salmi, E. Paatero, P. Nyholm, Kinetic model for the increase of reaction order during polyesterification, Chem. Eng. Process 43 (2004) 1487–1493, https://doi.org/10.1016/j.cep.2004.01.006.

[66] L.S. Cavalcante, V.S. Marques, J.C. Sczancoski, M.T. Escote, M.R. Joya, J. A. Varela, M.R.M.C. Santos, P.S. Pizani, E. Longo, Synthesis, structural refinement and optical behavior of CaTiO3 powders: a comparative study of processing in different furnaces, Chem. Eng. J. 143 (2008) 299–307, https://doi.org/10.1016/j.cej.2008.05.017.

[67] A.M. Ferrari, T.O. Germiniano, J.E. Savoia, R.G. Marques, V.A. dos Santos Ribeiro, A.C. Ueda, CaTiO3 perovskite in the photocatalysis of textile wastewater, Rev. Ambient. Água 14 (2019) e2336, https://doi.org/10.4136/ambi-agua.2336.

[68] V.S. Marques, L.S. Cavalcante, J.C. Sczancoski, D.P. Volanti, J.W.M. Espinosa, M. R. Joya, M.R.M.C. Santos, P.S. Pizani, J.A. Varela, E. Longo, Influence of microwave energy on structural and photoluminescent behavior of CaTiO3 powders, Solid State Sci. 10 (2008) 1056–1061, https://doi.org/10.1016/j.solidstatesciences.2007.11.004.

[69] M.R. Mohammadi, D.J. Fray, Synthesis of highly pure nanocrystalline and mesoporous $CaTiO_3$ by a particulate sol–gel route at the low temperature, J. Sol. Gel Sci. Technol. 68 (2013) 324–333, https://doi.org/10.1007/s10971-013-3173-8.

[70] M.C. Cordero-Cabrera, G.S. Walker, D.M. Grant, Effect of processing parameters on the particle size and stabilisation of titania sols, J. Mater. Sci. 40 (2005) 3709–3714, https://doi.org/10.1007/s10853-005-2825-7.

[71] D. Zhang, S. Liu, X. Song, Z. Xu, B. Yang, L. Chen, Y. Tan, F. Li, Preparation of calcium titanate based on the cotton template method and its simultaneous removal performance to heavy metals and organic pollutants in water, J. Adv. Oxid. Technol. 19 (2016) 9–18, https://doi.org/10.1515/jaots-2016-0101.

[72] D. Zhang, C.L. Zhang, P. Zhou, Preparation of porous nano-calcium titanate microspheres and its adsorption behavior for heavy metal ion in water, J. Hazard Mater. 186 (2011) 971–977, https://doi.org/10.1016/j.jhazmat.2010.11.096.

[73] D. Zhang, M. Wang, G. Ren, E. Song, Preparation of biomorphic porous calcium titanate and its application for preconcentration of nickel in water and food samples, Mater. Sci. Eng. C 33 (2013) 4677–4683, https://doi.org/10.1016/j.msec.2013.07.030.

[74] X. Yan, X. Huang, Y. Fang, Y. Min, Z. Wu, W. Li, J. Yuan, L. Tan, Synthesis of rodlike $CaTiO_3$ with enhanced charge separation efficiency and high photocatalytic activity, Int. J. Electrochem. Sci. 9 (2014) 5155–5163.

[75] S.J. Lee, Y.C. Kim, J.H. Hwang, An organic-inorganic solution technique for fabrication of nano-sized $CaTiO_3$ powder, J. Ceram. Process. Res. 5 (2004) 223–226.

[76] T. Xian, H. Yang, X. Shen, J.L. Jiang, Z.Q. Wei, W.J. Feng, Preparation of high-quality BiFeO3 nanopowders via a polyacrylamide gel route, J. Alloys Compd. 480 (2009) 889–892, https://doi.org/10.1016/j.jallcom.2009.02.068.

[77] Y.S. Huo, H. Yang, T. Xian, J.L. Jiang, Z.Q. Wei, R.S. Li, W.J. Feng, A polyacrylamide gel route to different-sized $CaTiO_3$ nanoparticles and their photocatalytic activity for dye degradation, J. Sol. Gel Sci. Technol. 71 (2014) 254–259, https://doi.org/10.1007/s10971-014-3366-9.

[78] L. Di, H. Yang, T. Xian, Y. Huo, An efficient $CaTiO_3$ nano sonocatalyst toward the dye degradation under ultrasonic irradiation, J. Ceram. Soc. Jap. 124 (2016) 1146–1151, https://doi.org/10.2109/jcersj2.16142.

[79] Q. Zhang, Y. Li, Z. Ren, Z. Ahmad, X. Li, G. Han, Synthesis of porous CaTiO3 nanotubes with tunable hollow structures via single-nozzle electrospinning, Mater. Lett. 152 (2015) 82–85, https://doi.org/10.1016/j.matlet.2015.03.103.

[80] M.M. Lencka, R.E. Riman, Thermodynamics of the hydrothermal synthesis of calcium titanate with reference to other alkaline-earth titanates, Chem. Mater. 7 (1995) 18–25, https://doi.org/10.1021/cm00049a006.

[81] S.S.S. Afghahi, M. Jafarian, S. Zargari, Y. Atassi, Synthesis of calcium titanate Powder with hollow square based prism morphology via one-step surfactant free hydrothermal method: temperature effect and optical properties, Trans. Indian Ceram. Soc. 76 (2017) 237–241, https://doi.org/10.1080/0371750X.2017.

[82] D. Wang, Z. Guo, Y. Chen, J. Hao, W. Liu, In situ hydrothermal synthesis of nanolamellate CaTiO3 with controllable structures and wettability, Inorg. Chem. 46 (2007) 7707–7709, https://doi.org/10.1021/ic700777f.

[83] W. Dong, B. Li, Y. Li, X. Wang, L. An, C. Li, B. Chen, G. Wang, Z. Shi, General approach to well-defined perovskite $MTiO_3$ (M=Ba, Sr, Ca, and Mg) nanostructures, J. Phys. Chem. C 115 (2011) 3918–3925, https://doi.org/10.1021/jp110660v.

[84] W. Dong, G. Zhao, B. Song, G. Xu, J. Zhou, G. Han, Surfactant-free fabrication of CaTiO3 butterfly-like dendrite via a simple one-step hydrothermal route, CrystEngComm 14 (2012) 6990–6997, https://doi.org/10.1039/C2CE25472G.

[85] W. Dong, G. Zhao, Q. Bao, X. Gu, Effects of morphologies on the photocatalytic properties of $CaTiO_3$ nano/microstructures, J. Ceram. Soc. Jpn. 124 (2016) 475–479, https://doi.org/10.2109/jcersj2.15272.

[86] S.K. Durrani, Y. Khan, N. Ahmed, M. Ahmad, M.A. Hussain, Hydrothermal growth of calcium titanate nanowires from titania, J. Iran. Chem. Soc. 8 (2011) 562–569, https://doi.org/10.1007/BF03249091.

[87] Y. Huang, H. Chiu, C. Lee, Growth of $CaTiO_3$ dendrites and rectangular prisms through a wet chemical method, CrystEngComm 11 (2009) 1904–1909, https://doi.org/10.1039/B900213H.

[88] Y. Li, X.P. Gao, G.R. Li, G.L. Pan, T.Y. Yan, H.Y. Zhu, Titanate nanofiber reactivity: fabrication of $MTiO_3$ (M=Ca, Sr, and Ba) perovskite oxides, J. Phys. Chem. C 113 (2009) 4386–4394, https://doi.org/10.1021/jp810805f.

[89] T.R.N. Kutty, R. Vivekanandan, Precipitation of rutile and anatase (TiO2) fine powders and their conversion to MTiO3 (M = Ba, Sr, Ca) by the hydrothermal method, Mater. Chem. Phys. 19 (1988) 533–546, https://doi.org/10.1016/0254-0584(88)90045-4.

[90] S. Li, J. Zhang, S. Jamil, Q. Cai, S. Zang, Conversion of eggshells into calcium titanate cuboid and its adsorption properties, Res. Chem. Intermed. 44 (2018) 3933–3946, https://doi.org/10.1007/s11164-018-3332-1.

[91] J. Zhuang, Q. Tian, S. Lin, W. Yang, L. Chen, P. Liu, Precursor morphology-controlled formation of perovskites CaTiO3 and their photo-activity for As(III) removal, Appl. Catal., B 156–157 (2014) 108–115, https://doi.org/10.1016/j.apcatb.2014.02.015.

[92] M.L. Moreira, E.C. Paris, G.S. do Nascimento, V.M. Longo, J.R. Sambrano, V. R. Mastelaro, M.I.B. Bernardi, J. Andrés, J.A. Varela, E. Longo, Structural and optical properties of CaTiO3 perovskite-based materials obtained by microwave-assisted hydrothermal synthesis: an experimental and theoretical insight, Acta Mater. 57 (2009) 5174–5185, https://doi.org/10.1016/j.actamat.2009.07.019.

[93] T.M. Mazzo, G.S.N. Libanori, M.L. Moreira, W. Avansi, V.R. Mastelaro, J. A. Varela, E. Longo, Influence of titanium precursor on photoluminescent emission of micro-cube-shaped $CaTiO_3$, J. Lumin. 165 (2015) 130–137, https://doi.org/10.1016/j.jlumin.2015.03.028.

[94] T. Kimijima, K. Kanie, M. Nakaya, A. Muramatsu, Hydrothermal synthesis of size- and shape-controlled $CaTiO_3$ fine particles and their photocatalytic activity, CrystEngComm 16 (2014) 5591–5597, https://doi.org/10.1039/C4CE00376D.

[95] T. Alammar, I. Hamm, M. Wark, A.-V. Mudring, Low-temperature route to metal titanate perovskite nanoparticles for photocatalytic applications, Appl. Catal., B 178 (2015) 20–28, https://doi.org/10.1016/j.apcatb.2014.11.010.

[96] Y. Yan, H. Yang, X. Zhao, H. Zhang, J. Jiang, A hydrothermal route to the synthesis of CaTiO3 nanocuboids using P25 as the titanium source, J. Electron. Mater. 47 (2018) 3045–3050, https://doi.org/10.1007/s11664-018-6183-z.

[97] L.M. Lozano-Sánchez, S.-W. Lee, T. Sekino, V. Rodrıguez-González, Practical microwave-induced hydrothermal synthesis of rectangular prism-like CaTiO3, CrystEngComm 15 (2013) 2359–2362, https://doi.org/10.1039/C3CE27040H.

[98] Y. Hang, Y. Si, Q. Zhou, H. Yin, A. Wang, A. Cao, Morphology-controlled synthesis of calcium titanate particles and adsorption kinetics, isotherms, and thermodynamics of Cd(II), Pb(II), and Cu (II) cations, J. Hazard Mater. 380 (2019) 120789, https://doi.org/10.1016/j.jhazmat.2019.120789.

[99] T.R.N. Kutty, R. Vivekanandan, Preparation of CaTiO3 fine powders by the hydrothermal method, Mater. Lett. 5 (1987) 79–83, https://doi.org/10.1016/0167-577X(87)90080-2.

[100] J. Pei, J. Meng, S. Wu, Q. Lin, J. Li, X. Wei, G. Han, Z. Zhang, Hierarchical CaTiO3 nanowire-network architectures for $H_2$ evolution under visible-light irradiation, J. Alloys Compd. 806 (2019) 889–896, https://doi.org/10.1016/j.jallcom.2019.07.294.

[101] X. Yang, I.D. Williams, J. Chen, J. Wang, H. Xu, H. Konishi, Y. Pan, C. Liang, M. Wu, Perovskite hollow cubes: morphological control, three-dimensional twinning and intensely enhanced photoluminescence, J. Mater. Chem. 18 (2008) 3543–3546, https://doi.org/10.1039/B808396G.

[102] X. Yang, J. Fu, C. Jin, J. Chen, C. Liang, M. Wu, W. Zhou, Formation mechanism of CaTiO3 hollow crystals with different microstructures, J. Am. Chem. Society 132 (2010) 14279–14287, https://doi.org/10.1021/ja106461u.

[103] H. Zhao, Y. Duan, X. Sun, Synthesis and characterization of $CaTiO_3$ particles with controlled shape and size, New J. Chem. 37 (2013) 986–991, https://doi.org/10.1039/C3NJ40974K.

[104] T. Kimijima, K. Kanie, M. Nakaya, A. Muramatsu, Solvothermal synthesis of shape-controlled perovskite $MTiO_3$ (M = Ba, Sr, and Ca) particles in $H_2O$/polyols mixed solutions, Mater. Trans. 55 (2014) 147–153, https://doi.org/10.2320/matertrans.M2013350.

[105] W. Dong, B. Song, G. Zhao, W. Meng, G. Han, Effects of the volume ratio of water and ethanol on morphosynthesis and photocatalytic activity of $CaTiO_3$ by a solvothermal process, Appl. Phys. A 123 (2017) 348, https://doi.org/10.1007/s00339-017-0931-4.

[106] D. Yu, J. Zhang, F. Wang, M. Zhao, K. Du, S. Shu, J. Zou, Y. Wan, High-symmetry epitaxial growth under solvothermal conditions: a strategy for architectural growth of tubular and nontubular $CaTiO_3$ microstructures with regular geometrical morphologies and tunable dimensions, Cryst. Growth Des. 13 (2013) 3138–3143, https://doi.org/10.1021/cg400514q.

[107] W. Dong, B. Song, W. Meng, Gaoling Zhao, G. Han, A simple solvothermal process to synthesize CaTiO3 microspheres and its photocatalytic properties, Appl. Surf. Sci. 349 (2015) 272–278, https://doi.org/10.1016/j.apsusc.2015.05.006.

[108] W. Dong, Q. Bao, X. Gu, G. Zhao, Controlled synthesis of flower-like $CaTiO_3$ and effects of morphology on its photocatalytic activities, J. Ceram. Soc. Jpn. 123 (2015) 643–648, https://doi.org/10.2109/jcersj2.123.643.

[109] D. Stoyanova, I. Stambolova, V. Blaskov, K. Zaharieva, I. Avramova, O. Dimitrov, S. Vassilev, A. Eliyas, N. Nedyalkov, Mechanical milling of hydrothermally obtained CaTiO3 powders—morphology and photocatalytic activity, Nano-Struct. Nano-Objects 18 (2019) 100301, https://doi.org/10.1016/j.nanoso.2019.100301.

[110] Murata Manufacturing Co Ltd, A Process for the Preparation of Titanates, UK Patent No. 1 445672, 1974. March.

[111] M. Murata, A. Kitao, Preparation of Titanates, US Patent No. 4061, 1976, p. 583.

[112] G. Pfaff, Naβchemische synthese von $SrTiO_3$- und $CaTiO_3$-sinterpulvern durch Fällung von $SrTiO_2(O_2).3H_2O$ und $CaTiO_2(O_2)$, $3H_2O$. Z. Chem. 29 (1989) 30–31, https://doi.org/10.1002/zfch.19890290120.

[113] Z. Yang, H. Yamada, G.R. Miller, Synthesis and characterization of high-purity $CaTiO_3$, Am. Ceram. Soc. Bull. 64 (1985) 1550–1554.

[114] G. Pfaff, Peroxide route to synthesize calcium titanate powders of different composition, J. Eur. Ceram. Soc. 9 (1992) 293–299, https://doi.org/10.1016/0955-2219(92)90064-K.

[115] C. Karthikeyan, M. Thamima, S. Karuppuchamy, Dye removal efficiency of perovskite structured CaTiO3 nanospheres prepared by microwave assisted

method, in: Materials Today: Proceedings, 2019, https://doi.org/10.1016/j.matpr.2019.05.421, 2214-7853.
[116] C. Karthikeyan, M. Thamima, S. Karuppuchamy, Structural and photocatalytic property of CaTiO3 nanosphere, Mater. Sci. Forum 979 (2020) 169–174. https://doi.org/10.4028/www.scientific.net/MSF.979.169.
[117] N. Ohtsu, K. Sato, A. Yanagawa, K. Saito, Y. Imai, T. Kohgo, A. Yokoyama, K. Asami, T. Hanawa, $CaTiO_3$ coating on titanium for biomaterial application - optimum thickness and tissue response, J. Biomed. Mater. Res. 82 (2007) 304–315, https://doi.org/10.1002/jbm.a.31136.
[118] N. Ohtsu, K. Sato, K. Saito, K. Asami, T. Hanawa, Calcium phosphates formation on $CaTiO_3$ coated titanium, J. Mater. Sci. Mater. Med. 18 (2007) 1009–1016, https://doi.org/10.1007/s10856-006-0114-x.
[119] A. Krause, W. Weber, A. Jahn, K. Richter, D. Pohl, B. Rellinghaus, U. Schröder, J. Heitmann, T. Mikolaick, Evaluation of the electrical and physical properties of thin calcium titanate high-k insulators for capacitor applications, J. Vac. Sci. Technol. B 29 (2011), 01AC07, https://doi.org/10.1116/1.3521507.
[120] A. Krause, W.M. Weber, D. Pohl, B. Rellinghaus, A. Kersch, T. Mikolajick, Investigation of band gap and permittivity of the perovskite $CaTiO_3$ in ultrathin layers, J. Phys. D Appl. Phys. 48 (2015) 415304, https://doi.org/10.1088/0022-3727/48/41/415304.
[121] J. Hao, W. Si, X.X. Xi, R. Guo, A.S. Bhalla, L.E. Cross, Dielectric properties of pulsed-laser-deposited calcium titanate thin films, Appl. Phys. Lett. 76 (2000) 3100, https://doi.org/10.1063/1.126536.
[122] S. Muff, M. Fanciulli, A.P. Weber, N. Pilet, Z. Ristic, Z. Wang, N.C. Plumb, Milan Radovic, J. H. Dil, Observation of a two-dimensional electron gas at $CaTiO_3$ film surfaces, Appl. Surf. Sci. 432 (2018) 41–45, https://doi.org/10.1016/j.apsusc.2017.05.229.
[123] N. Ohtsu, A. Ito, K. Saito, T. Hanawa, Characterization of calcium titanate thin films deposited on titanium with reactive sputtering and pulsed laser depositions, Surf. Coating. Technol. 201 (2007) 7686–7691, https://doi.org/10.1016/j.surfcoat.2007.02.043.
[124] M.D. Biegalski, L. Qiao, Y. Gu, A. Mehta, Q. He, Y. Takamura, A. Borisevich, L.-Q. Chen, Impact of symmetry on the ferroelectric properties of $CaTiO_3$ thin films, Appl. Phys. Lett. 106 (2015) 162904, https://doi.org/10.1063/1.4918805.
[125] R.C. Haislmaier, E.D. Grimley, M.D. Biegalski, J.M. LeBeau, S. Trolier-McKinstry, V. Gopalan, R. Engel-Herbert, Unleashing strain induced ferroelectricity in complex oxide thin films via precise stoichiometry control, Adv. Funct. Mater. 26 (2016) 7271–7279, https://doi.org/10.1002/adfm.201602767.
[126] R.C. Haislmaier, Y. Lu, J. Lapano, H. Zhou, N. Alem, S.B. Sinnott, R. Engel-Herbert, V. Gopalan, Large tetragonality and room temperature ferroelectricity in compressively strained $CaTiO_3$ thin films, Apl. Mater. 7 (2019), 051104, https://doi.org/10.1063/1.5090798.
[127] M. Sato, R. Tu, T. Goto, Preparation conditions of $CaTiO_3$ film by metal-organic chemical vapor deposition, Mater. Trans. 47 (2006) 1386–1390, https://doi.org/10.2320/matertrans.47.1386.
[128] M. Sato, R. Tu, T. Goto, K. Ueda, T. Narushima, Hydroxyapatite formation on MOCVD-$CaTiO_3$ coated Ti, Key Eng. Mater. 352 (2007) 301–304. https://doi.org/10.4028/www.scientific.net/KEM.352.301.
[129] N. Shiraishi, R. Ishiko-Uzuka, K. Takahashi, T. Ogawa, T. Anada, O. Suzuki, T. Goto, K. Sasaki, Effect of functionally-graded calcium titanate film prepared by metal-organic chemical vapor deposition on titanium implant, Appl. Sci. 9 (2019) 172, https://doi.org/10.3390/app9010172.
[130] H. Katsui, Y. Kumagai, T. Goto, High-speed deposition of highly-oriented calcium titanate film by laser CVD, J. Jpn. Soc. Powder Powder Metall. 63 (2016) 123–127, https://doi.org/10.2497/jjspm.63.123.
[131] H. Katsui, T. Goto, Bio-ceramic coating of Ca–Ti–O system compound by laser chemical vapor deposition, in: K. Sasaki, N. Takahashi, O. Suzuki (Eds.), Interface Oral Health Science, Springer, Singapore, 2016, https://doi.org/10.1007/978-981-10-1560-1-4. Chap. 4.
[132] Y. Fujishiro, N. Sato, S. Uchida, T. Sato, Coating of CaTiO3 on titanium substrates by hydrothermal reactions using calcium-ethylene diamine tetra acetic acid chelate, J. Mater. Sci. Mater. Med. 9 (1998) 363–367, https://doi.org/10.1023/A:1013201627622.
[133] M. Kon, R. Sultana, E. Fujihara, K. Asaoka, T. Ichikawa, Calcium titanate film-coating on titanium with hydrothermal treatments, Key Eng. Mater. (2007) 737–740, 330–332, https://doi.org/10.4028/www.scientific.net/kem.330-332.737.
[134] S. Yang, H. Kou, H. Wang, K. Cheng, J. Wang, The photoelectrochemical properties of N3 sensitized $CaTiO_3$ modified $TiO_2$ nanocrystalline electrodes, Electrochim. Acta 55 (2009) 305–310, https://doi.org/10.1016/j.electacta.2009.08.055.
[135] Y. Ohba, T. Watanabe, E. Sakai, M. Daimon, Coating of HAp/$CaTiO_3$ multilayer on titanium substrates by hydrothermal method, J. Ceram. Soc. Jap. 107 (1999) 907–912, https://doi.org/10.2109/jcersj.107.907.
[136] Y. Zhu, X. Wang, Y. Zhou, C. Zhao, J. Yuan, Z. Wu, S. Wu, S. Wang, In situ formation of bioactive calcium titanate coatings on titanium screws for medical implants, RSC Adv. 6 (2016) 53182–53187, https://doi.org/10.1039/C6RA06597J.
[137] M. Ye, M. Wang, D. Zheng, N. Zhang, C. Lin, Z. Lin, Garden-like perovskite superstructures with enhanced photocatalytic activity, Nanoscale 6 (2014) 3576–3584, https://doi.org/10.1039/C3NR05564G.
[138] X. Shi, H. Yang, Z. Liang, A. Tian, X. Xue, Synthesis of vertically aligned CaTiO3 nanotubes with simple hydrothermal method and its photoelectrochemical property, Nanotechnology 29 (2018) 385605, https://doi.org/10.1088/1361-6528/aacfde.
[139] C.-Y. Chen, K. Ozasa, K. Katsumata, M. Maeda, K. Okada, N. Matsushita, $CaTiO_3$ nanobricks prepared from anodized TiO2 nanotubes, Electrochem. Commun. 22 (2012) 101–104, https://doi.org/10.1016/j.elecom.2012.05.012.
[140] F. Zhang, S. Chen, C. Lin, Y. Yin, Anodic-hydrothermal preparation of prism-shaped $CaTiO_3$ structure on titanium surface, Appl. Surf. Sci. 257 (2011) 3092–3096, https://doi.org/10.1016/j.apsusc.2010.10.122.
[141] M. Yoshimura, W. Urushihara, M. Yashima, M. Kakihana, CaTiO3 coating on TiAl by hydrothermal-electrochemical technique, Intermetallics 3 (1995) 125–128, https://doi.org/10.1016/0966-9795(95)92676-Q.
[142] J.P. Wiff, V.M. Fuenzalida, R.A. Zarate, J.L. Arias, M.S. Fernandez, Characterization of hydrothermal–electrochemical calcium titanate coatings on titanium and biomedical titanium alloy, J. Phys. Condens. Matter 16 (2004) S1345–S1350, https://doi.org/10.1088/0953-8984/16/14/047.
[143] J.P. Wiff, V.M. Fuenzalida, J.L. Arias, M.S. Fernandez, Hydrothermal–electrochemical CaTiO3 coatings as precursor of a biomimetic calcium phosphate layer, Mater. Lett. 61 (2007) 2739–2743, https://doi.org/10.1016/j.matlet.2006.06.092.
[144] H. Cheng, H. Hua, G. Li, M. Zhang, K. Xiang, Z. Zhu, Y. Wane, Calcium titanate micro-sheets scaffold for improved cell viability and osteogenesis, Chem. Eng. J. 389 (2020) 124400, https://doi.org/10.1016/j.cej.2020.124400.
[145] S. Holliday, A. Stanishevsky, Crystallization of $CaTiO_3$ by sol–gel synthesis and rapid thermal processing, Surf. Coating. Technol. 188–189 (2004) 741–744, https://doi.org/10.1016/j.surfcoat.2004.07.044.
[146] R. Li, Y. Li, C. Yan, Y. Bao, H. Sun, H. Hu, N. Li, Thickness-dependent and tunable mechanical properties of CaTiO3 dielectric thin films determined by nanoindentation technique, Ceram. Int. 46 (2020) 22643–22649, https://doi.org/10.1016/j.ceramint.2020.06.027.
[147] M. Manso, M. Langlet, J.M. Martínez-Duart, Testing sol-gel CaTiO3 coatings for biocompatible applications, Mater. Sci. Eng. C 23 (2003) 447–450, https://doi.org/10.1016/S0928-4931(02)00319-3.
[148] M.R. Sahu, P.K. Mallik, S.C. Patnaik, A. Behera, Synthesis and microstructure $CaTiO_3$ coating by sol-gel spin-coating process, Int. J. Res. Sppl. Sci. Biotechnol. 5 (2018) 6–9. https://www.ijrasb.com/ojs/index.php/ojs-ijrasb/article/view/46.
[149] V. Stanishevsky, S. Holliday, Mechanical properties of sol–gel calcium titanate bioceramic coatings on titanium, Surf. Coating. Technol. 202 (2007) 1236–1241, https://doi.org/10.1016/j.surfcoat.2007.07.091.
[150] F. Zhang, J. Chen, X. Zhang, W. Gao, R. Jin, N. Guan, Y. Li, Synthesis of titania-supported platinum catalyst: the effect of pH on morphology control and valence state during photodeposition, Langmuir 20 (2004) 9329–9334, https://doi.org/10.1021/la049394o.
[151] H. Mizoguchi, K. Ueda, M. Orita, S.C. Moon, K. Kajihara, M. Hirano, H. Hosono, Decomposition of water by a $CaTiO_3$ photocatalyst under UV light irradiation, Mater. Res. Bull. 37 (2002) 2401–2406, https://doi.org/10.1016/S0025-5408(02)00974-1.
[152] S. Liu, Y. Qu, R. Li, G. Wang, Y. Li, Photocatalytic activity of $MTiO_3$ (M = Ca, Ni, and Zn) nanocrystals for water decomposition to hydrogen, J. Mater. Res. 29 (2014) 1295–1301, https://doi.org/10.1557/jmr.2014.110.
[153] J. Cai, A. Cao, J. Huang, W. Jin, J. Zhang, Z. Jiang, X. Li, Understanding oxygen vacancies in disorder-engineered surface and subsurface of CaTiO3 nanosheets on photocatalytic hydrogen evolution, Appl. Catal., B 267 (2020) 118378, https://doi.org/10.1016/j.apcatb.2019.118378.
[154] K. Shimura H. Yoshida, Hydrogen production from water and methane over Pt-loaded calcium titanate photocatalyst, Energy Environ. Sci. 3 (2010) 615–617, https://doi.org/10.1039/B922793H.
[155] A. Alzahrani, D. Barbash, A. Samokhvalov, One-pot synthesis and photocatalytic hydrogen generation with nanocrystalline Ag(0)/$CaTiO_3$ and in situ mechanistic studies, J. Phys. Chem. C 120 (2016) 19970–19979, https://doi.org/10.1021/acs.jpcc.6b05407.
[156] H. Yoshida, L. Zhang, M. Sato, T. Morikawa, T. Kajino, T. Sekito, S. Matsumoto, H. Hirata, Calcium titanate photocatalyst prepared by a flux method for reduction of carbon dioxide with water, Catal. Today 251 (2015) 132–139, https://doi.org/10.1016/j.cattod.2014.10.039.
[157] Z. Jiang, J. Pan, B. Wang, C. Li, Two dimensional Z-scheme AgCl/Ag/$CaTiO_3$ nano-heterojunctions for photocatalytic hydrogen production enhancement, Appl. Surf. Sci. 436 (2018) 519–526, https://doi.org/10.1016/j.apsusc.2017.12.065.
[158] J. Han, Y. Liu, F. Dai, R. Zhao, L. Wang, Fabrication of CdSe/$CaTiO_3$ nanocomposties in aqueous solution for improved photocatalytic hydrogen production, Appl. Surf. Sci. 459 (2018) 520–526, https://doi.org/10.1016/j.apsusc.2018.08.026.
[159] F. Dai, Y. Wang, R. Zhao, X. Zhou, J. Han, L. Wang, $ZnIn_2S_4$ modified $CaTiO_3$ nanocubes with enhanced photocatalytic hydrogen performance, Int. J. Hydrogen Energy 45 (2020) 28783–28791, https://doi.org/10.1016/j.apsusc.2018.08.026.
[160] J. Pan, Z. Jiang, S. Feng, C. Zhao, Z. Dong, B. Wang, J. Wang, C. Song, Y. Zheng, C. Li, The enhanced photocatalytic hydrogen production of the fusiform g-$C_3N_4$ modification $CaTiO_3$ nano-heterojunction, Int. J. Hydrogen Energy 43 (2018) 19019–19028, https://doi.org/10.1016/j.ijhydene.2018.08.102.
[161] J. Wang, F. Han, Y. Rao, T. Hu, Y. Huang, J. Cao, S.C. Lee, Visible-light-driven nitrogen-doped Carbon Quantum Dots/$CaTiO_3$ composite catalyst with enhanced NO adsorption for NO removal, Ind. Eng. Chem. Res. 57 (2018) 10226–10233, https://doi.org/10.1021/acs.iecr.8b01731.
[162] Y. Yan, H. Yang, Z. Yi, R. Li, X. Wang, Enhanced photocatalytic performance and mechanism of Au@$CaTiO_3$ composites with Au nanoparticles assembled on $CaTiO_3$ nanocuboids, Micromachines 10 (2019) 254, https://doi.org/10.3390/mi10040254.

[163] L. Bai, Q. Xu, Z. Cai, Synthesis of Ag@AgBr/CaTiO3 composite photocatalyst with enhanced visible light photocatalytic activity, J. Mater. Sci. Mater. Electron. 29 (2018) 17580–17590, https://doi.org/10.1007/s10854-018-9861-y.
[164] G.K. Kara, M. Moshari, M. Rabbani, R. Rahimi, A novel and green heterogeneous photocatalytic system ($Ca_{0.01}Fe_{2.9}$ $O_4$/$CaTiO_3$ nanocomposite): protocol synthesis, characterization, and study of photo-decoloration activity, Mater. Chem. Phys. 259 (2021) 124062, https://doi.org/10.1016/j.matchemphys.2020.124062.
[165] Y. Yan, H. Yang, Z. Yi, et al., Direct Z-scheme $CaTiO_3$@BiOBr composite photocatalysts with enhanced photodegradation of dyes, Environ. Sci. Pollut. Res. 26 (2019) 29020–29031, https://doi.org/10.1007/s11356-019-06085-y.
[166] S. Otsuka-Yao-Matsuo, T. Omata, S. Ueno, M. Kita, Photobleaching of methylene blue aqueous solutions sensitized by composite powders of titanium oxide with $SrTiO_3$, $BaTiO_3$, and $CaTiO_3$, Mater. Trans. 44 (2003) 2124–2129, https://doi.org/10.2320/matertrans.44.2124.
[167] Y. Wang, C.-G. Niu, L. Wang, Y. Wang, X.-G. Zhang, G.-M. Zeng, Synthesis of fern-like Ag/AgCl/$CaTiO_3$ plasmonic photocatalysts and their enhanced visible-light photocatalytic properties, RSC Adv. 6 (2016) 47873–47882, https://doi.org/10.1039/C6RA06435C.
[168] Y. Yan, H. Yang, Z. Yi, T. Xian, R. Li, X. Wang, Construction of $Ag_2S$@$CaTiO_3$ heterostructure photocatalysts for enhanced photocatalytic degradation of dyes, Desalination Water Treat 170 (2019) 349–360, https://doi.org/10.5004/dwt.2019.24747.
[169] T. Xian, H. Yang, Y.S. Huo, Enhanced photocatalytic activity of $CaTiO_3$-graphene nanocomposites for dye degradation, Phys. Scripta 89 (2014) 115801, https://doi.org/10.1088/0031-8949/89/11/115801.
[170] S.-W. Lee, L.M. Lozano-Sánchez, V. Rodríguez-González, Green tide deactivation with layered-structure cuboids of Ag/$CaTiO_3$ under UV light, J. Hazard Mater. 263 (2013) 20–27, https://doi.org/10.1016/j.jhazmat.2013.08.017.
[171] A. Shawky, M. Alhaddad, K.S. Al-Namshah, R.M. Mohamed, Nasser S. Awwad, Synthesis of Pt-decorated $CaTiO_3$ nanocrystals for efficient photoconversion of nitrobenzene to aniline under visible light, J. Mol. Liq. 304 (2020) 112704, https://doi.org/10.1016/j.molliq.2020.112704.
[172] Ž. Kesić, I. Lukić, M. Zdujić, Č. Jovalekić, V. Veljković, D. Skala, Assessment of $CaTiO_3$, $CaMnO_3$, $CaZrO_3$ and $Ca_2Fe_2O_5$ perovskites as heterogeneous base catalysts for biodiesel synthesis, Fuel Process. Technol. 143 (2016) 162–168, https://doi.org/10.1016/j.fuproc.2015.11.018.
[173] N.Y. Yahya, N. Ngadi, M. Jusoh, N.A.A. Halim, Characterization and parametric study of mesoporous calcium titanate catalyst for transesterification of waste cooking oil into biodiesel, Energy Convers. Manag. 129 (2016) 275, https://doi.org/10.1016/j.enconman.2016.10.037, 28.
[174] S.F. Wu, Y.Q. Zhu, Behavior of $CaTiO_3$/nano-CaO as a $CO_2$ reactive adsorbent, Ind. Eng. Chem. Res. 49 (2010) 2701–2706, https://doi.org/10.1021/ie900900r.
[175] T.-W. Tseng, U. Rajaji, T.-W. Chen, S.-M. Chen, Y.-C. Huang, V. Mani, A.I. Jothi, Sonochemical synthesis and fabrication of perovskite type calcium titanate interfacial nanostructure supported on graphene oxide sheets as a highly efficient electrocatalyst for electrochemical detection of chemotherapeutic drug, Ultrason. Sonochem. 69 (2020) 105242, https://doi.org/10.1016/j.ultsonch.2020.105242.
[176] C. Jia, J. Gao, J. Li, F. Gu, G. Xu, Z. Zhong, F. Su, Nickel catalysts supported on calcium titanate for enhanced CO methanation, Catal. Sci. Technol. 3 (2013) 490–499, https://doi.org/10.1039/C2CY20542D.
[177] J. Lin, J. Hu, C. Qiu, H. Huang, L. Chen, Y. Xie, Z. Zhang, H. Lin, X. Wang, In situ hydrothermal etching fabrication of $CaTiO_3$ on $TiO_2$ nanosheets with heterojunction effects to enhance $CO_2$ adsorption and photocatalytic reduction, Catal. Sci. Technol. 9 (2019) 336–346, https://doi.org/10.1039/C8CY02142B.
[178] A.P. Rodriguez, M. Inoue, T. Tanaka, M. Miyake, A.M. Sfer, E. Kishimoto, H. Tsujigiwa, R.S. Rivera, H. Nagatsuka, Effect of $CaTiO_3$–$CaCO_3$ prepared by alkoxide method on cell response, J. Biomed. Mater. Res. 93 (2010) 297–303, https://doi.org/10.1002/jbm.a.32551.
[179] M.A. Ehsan, R. Naeem, V. McKee, A. Rehman, A.S. Hakeem, M. Mazhar, Fabrication of photoactive $CaTiO_3$-$TiO_2$ composite thin film electrodes via facile single step aerosol assisted chemical vapor deposition route, J. Mater. Sci. Mater. Electron. 30 (2019) 1411–1424, https://doi.org/10.1007/s10854-018-0411-4.
[180] L. Mazzapioda, C.L. Vecchio, O. Danyliv, V. Baglio, A. Martinelli, M.A. Navarra, Composite Nafion-$CaTiO_{3-\delta}$ membranes as electrolyte component for PEM fuel cells, Polymers 12 (2020), https://doi.org/10.3390/polym12092019, 2019.
[181] L. Mazzapioda, M.A. Navarra, F. Trequattrini, A. Paolone, K. Elamin, A. Martinelli, O. Palumbo, Composite Nafion membranes with $CaTiO_{3-\delta}$ additive for possible applications in electrochemical devices, Membranes 9 (2019) 143, https://doi.org/10.3390/membranes9110143.
[182] B. Li, K. Zhang, W. Yang, X. Yin, Y. Liu, Enhanced corrosion resistance of HA/$CaTiO_3$/$TiO_2$/PLA coated AZ31 alloy, J. Taiwan Inst. Chem. Eng. 59 (2016) 465–473, https://doi.org/10.1016/j.jtice.2015.07.028.
[183] L. Zhu, Y. Saito, K. Koike, K. Kuroda, M. Okido, Fabrication of the silicate containing $CaTiO_3$ film with hydrophilic and smooth surface on titanium to improve osteoconductivity, Mater. Trans. 60 (2019) 1807–1813, https://doi.org/10.2320/matertrans.ME201905.
[184] Z. Kang, B. Yu, S. Fu, D. Li, X. Zhang, Z. Qian, Z. Zhong, B. Yu, H. Ding, Y. Zhu, J. Huang, Three-dimensional printing of $CaTiO_3$ incorporated porous β-$Ca_2SiO_4$ composite scaffolds for bone regeneration, Appl. Mater. Today 16 (2019) 132–140, https://doi.org/10.1016/j.apmt.2019.05.005.
[185] N. Ohtsu, C. Abe, T. Ashino, S. Semboshi, K. Wagatsuma, Calcium-hydroxide slurry processing for bioactive calcium-titanate coating on titanium, Surf. Coating. Technol. 202 (2008) 5110–5115, https://doi.org/10.1016/j.surfcoat.2008.05.035.
[186] N. Ohtsu, M. Hayashi, J. Ueta, T. Kanno, Biofunctional calcium titanate coating on titanium by simple chemical treatment process using calcium-hydroxide slurry-effects of the heating temperatures, Prog. Org. Coating 70 (2011) 353–357, https://doi.org/10.1016/j.porgcoat.2010.11.015.
[187] D. Wei, Y. Zhou, D. Jia, Y. Wang, Formation of $CaTiO_3$/$TiO_2$ composite coating on titanium alloy for biomedical applications, J. Biomed. Mater. Res. B 84 (2008) 444–451, https://doi.org/10.1002/jbm.b.30890.
[188] D. Wei, Y. Zhou, D. Jia, Y. Wang, Structure of calcium titanate/titania bioceramic composite coatings on titanium alloy and apatite deposition on their surfaces in a simulated body fluid, Surf. Coating. Technol. 201 (2007) 8715–8722, https://doi.org/10.1016/j.surfcoat.2007.04.124.
[189] N. Nagai, M. Okauchi, A. Rodriguez, M. Gunduz, H. Hu, M. Kubota, N. Nagaoka, H. Nagatsuka, T. Takagi, M. Akao, Development of new titanium coating material ($CaTiO_3$-aC) with modified decomposition method, J. Hard Tissue Biol. 17 (2008) 47–54, https://doi.org/10.2485/jhtb.17.47.
[190] M. Inoue, A.P. Rodriguez, T. Takagi, N. Katase, M. Kubota, N. Nagai, H. Nagatsuka, M. Inoue, N. Nagaoka, S. Takagi, K. Suzuki, Effect of a new titanium coating material ($CaTiO_3$-aC) prepared by thermal decomposition method on osteoblastic cell response, J. Biomater. Appl. 24 (2010) 657–672, https://doi.org/10.1177/0885328209340334.
[191] K. Asami, K. Saito, N. Ohtsu, S. Nagata, T. Hanawa, Titanium-implanted $CaTiO_3$ films and their changes in Hanks' solution, Surf. Interface Anal. 35 (2003) 483–488, https://doi.org/10.1002/sia.1554.
[192] N. Ohtsu, K. Sato, K. Saito, T. Hanawa, K. Asami, Evaluation of degradability of $CaTiO_3$ thin films in simulated body fiuids, Mater. Trans. 45 (2004) 1778–1781, https://doi.org/10.2320/matertrans.45.1778.
[193] P. Zhou, M. Akao, Preparation and characterization of double layered coating composed of hydroxyapatite and perovskite by thermal decomposition, Bio Med. Mater. Eng. 7 (1997) 67–81, https://doi.org/10.3233/BME-1997-7106.
[194] T.J. Webster, C. Ergun, R.H. Doremus, W.A. Lanford, Increased osteoblast adhesion on titanium-coated hydroxyapatite that forms $CaTiO_3$, J. Biomed. Mater. Res. 67 (2003) 975–980, https://doi.org/10.1002/jbm.a.10160.
[195] M. Yadi, H. Esfahani, M. Sheikhi, M. Mohammadi, $CaTiO_3$/α-TCP coatings on CP-Ti prepared via electrospinning and pulsed laser treatment for in-vitro bone tissue engineering, Surf. Coating. Technol. 401 (2020) 126256, https://doi.org/10.1016/j.surfcoat.2020.126256.
[196] A.K. Dubey, G. Tripathi, B. Basu, Characterization of hydroxyapatite-perovskite (CaTiO3) composites: phase evaluation and cellular response, J. Biomed. Mater. Res. B 95 (2010) 320–329, https://doi.org/10.1002/jbm.b.31716.
[197] C. Ergun, H. Liu, J.W. Halloran, T.J. Webster, Increased osteoblast adhesion on nanograined hydroxyapatite and tricalcium phosphate containing calcium titanate, J. Biomed. Mater. Res. 80 (2007) 990–997, https://doi.org/10.1002/jbm.a.30923.
[198] Z. Liu, K.C. Chan, L. Liu, S.F. Guo, Bioactive calcium titanate coatings on a Zr-based bulk metallic glass by laser cladding, Mater. Lett. 82 (2012) 67–70, https://doi.org/10.1016/j.matlet.2012.05.022.
[199] G. Li, Q. Xiao, R. McNaughton, L. Han, L. Zhang, Y. Wang, Y. Yang, Nanoengineered porous chitosan/$CaTiO_3$ hybrid scaffolds for accelerating Schwann cells growth in peripheral nerve regeneration, Colloids Surf., B 158 (2017) 57–67, https://doi.org/10.1016/j.colsurfb.2017.06.026.
[200] J.-W. Park, K.-B. Park, J.-Y. Suh, Effects of calcium ion incorporation on bone healing of Ti6Al4V alloy implants in rabbit tibiae, Biomaterials 28 (2007) 3306–3313, https://doi.org/10.1016/j.biomaterials.2007.04.007.
[201] J.-W. Park, Y. Tustusmi, C.S. Lee, C.H. Park, Y.-J. Kim, J.-H. Jang, D. Khang, Y.-M. Im, H. Doi, N. Nomura, T. Hanawa, Surface structures and osteoblast response of hydrothermally produced $CaTiO_3$ thin film on Ti–13Nb–13Zr alloy, Appl. Surf. Sci. 257 (2011) 7856–7863, https://doi.org/10.1016/j.apsusc.2011.04.054.
[202] J.-Y. Suh, O.-C. Jeung, B.-J. Choi, J.-W. Park, Effects of a novel calcium titanate coating on the osseointegration of blasted endosseous implants in rabbit tibiae, Clin. Oral Implants Res. 18 (2007) 362–369, https://doi.org/10.1111/j.1600-0501.2006.01323.x.
[203] S. de Lazaro, J. Milanez, A.T. de Figueiredo, V.M. Longo, V.R. Mastelaro, F.S. De Vicente, A.C. Hernandes, J.A. Varela, E. Longo, Relation between photoluminescence emission and local order-disorder in the $CaTiO_3$ lattice modifier, Appl. Phys. Lett. 90 (2007) 111904, https://doi.org/10.1063/1.2713359.
[204] A.C. Tas, The use of physiological solutions or media in calcium phosphate synthesis and processing, Acta Biomater. 10 (2014) 1771–1792, https://doi.org/10.1016/j.actbio.2013.12.047.
[205] T. Kokubo, Bioactive glass ceramics: properties and applications, Biomaterials 12 (1991) 155–163, https://doi.org/10.1016/0142-9612(91)90194-F.
[206] H. Pan, X. Zhao, B.W. Darvell, W.W. Lu, Apatite-formation ability – predictor of "bioactivity"? Acta Biomater. 6 (2010) 4181–4188, https://doi.org/10.1016/j.actbio.2010.05.01325.
[207] S. Myhra, H.E. Bishop, J.C. Rivière, M. Stephenson, Hydrothermal dissolution of perovskite ($CaTiO_3$), J. Mater. Sci. 22 (1987) 3217–3226, https://doi.org/10.1007/BF01161185.
[208] Z. Zhang, M.G. Blackford, G.R. Lumpkin, K.L. Smith, E.R. Vance, Aqueous dissolution of perovskite ($CaTiO_3$): effects of surface damage and [$Ca^{2+}$] in the leachant, J. Mater. Res. 20 (2005) 2462–2473, https://doi.org/10.1557/jmr.2005.0294.
[209] M. Sato, R. Tu, T. Goto, K. Ueda, T. Narushima, Apatite formation behavior on bio-ceramic films prepared by MOCVD, J. Ceram. Soc. Jap. 117 (2009) 461–465, https://doi.org/10.2109/jcersj2.117.461.
[210] D. Wang, Y. Liu, H. Hu, Z. Zeng, F. Zhou, W. Liu, Electrochemical characterization of the solution accessibility of $CaTiO_3$ microstructures and improved

biomineralization, J. Phys. Chem. C 112 (2008) 16123–16129, https://doi.org/10.1021/jp8063323.
[211] J. Coreño, O. Coreño, Evaluation of calcium titanate as apatite growth promoter, J. Biomed. Mater. Res. 75 (2005) 478–484, https://doi.org/10.1002/jbm.a.30447.
[212] J.-M. Zhang, J. Cui, K.-W. Xu, V. Ji, Z.-Y. Man, *Ab initio* modeling of $CaTiO_3$ (110) polar surfaces, Phys. Rev. B 76 (2007) 115426, https://doi.org/10.1103/PhysRevB.76.115426.
[213] R.I. Eglitis, D. Vanderbilt, Ab initio calculations of the atomic and electronic structure of $CaTiO_3$ (001) and (011) surfaces, Phys. Rev. B 78 (2008) 155420, https://doi.org/10.1103/PhysRevB.78.155420.
[214] T. Stich, F. Alagboso, T. Křenek, T. Kovářík, V. Alt, D. Docheva, Implant-bone-interface: Reviewing the impact of titanium surface modifications on osteogenic processes in vitro and in vivo. Bioeng. Transl. Med., Early View, https://doi.org/10.1002/btm2.10239.
[215] E.M. Lotz, M.B. Berger, Z. Schwartz, B.D. Boyan, Regulation of osteoclasts by osteoblast lineage cells depends on titanium implant surface properties, Acta Biomater. 68 (2018) 296–307, https://doi.org/10.1016/j.actbio.2017.12.039.
[216] R. Olivares-Navarrete, S.L. Hyzy, J.H. Park, G.R. Dunn, D.A. Haithcock, C. E. Wasilewski, B.D. Boyan, Z. Schwartz, Mediation of osteogenic differentiation of human mesenchymal stem cells on titanium surfaces by a Wnt-integrin feedback loop, Biomaterials 32 (2011) 6399–6411, https://doi.org/10.1016/j.biomaterials.2011.05.036.
[217] S. Dhivya, A. Keshav Narayan, R. Logith Kumar, S. Viji Chandran, M. Vairamani, N. Selvamurugan, Proliferation and differentiation of mesenchymal stem cells on scaffolds containing chitosan, calcium polyphosphate and pigeonite for bone tissue engineering, Cell Prolif 51 (2018), e12408, https://doi.org/10.1111/cpr.12408.
[218] M. Zayzafoon, Calcium/calmodulin signaling controls osteoblast growth and differentiation, J. Cell. Biochem. 97 (2006) 56–70, https://doi.org/10.1002/jcb.20675.
[219] M.N. Lee, H.-S. Hwang, S.-H. Oh, A. Roshanzadeh, J.-W. Kim, J.H. Song, E.-S. Kim, J.-T. Koh, Elevated extracellular calcium ions promote proliferation and migration of mesenchymal stem cells via increasing osteopontin expression, Exp. Mol. Med. 50 (2018) 142, https://doi.org/10.1038/s12276-018-0170-6, 16 pages.
[220] K. Li, S. Liu, T. Hu, I. Razanau, X. Wu, H. Ao, L. Huang, Y. Xie, X. Zheng, Optimized Nanointerface engineering of micro/nanostructured titanium implants to enhance cell−nanotopography interactions and osseointegration, ACS Biomater. Sci. Eng. 6 (2020) 969–983, https://doi.org/10.1021/acsbiomaterials.9b01717.
[221] A. Klos, X. Sedao, T.E. Itina, C. Helfenstein-Didier, C. Donnet, S. Peyroche, L. Vico, A. Guignandon, V. Dumas, Ultrafast laser processing of nanostructured patterns for the control of cell adhesion and migration on titanium alloy, Nanomaterials 10 (2020) 864, https://doi.org/10.3390/nano10050864.
[222] D.V. Nazarov, V.M. Smirnov, E.G. Zemtsova, N.M. Yudintceva, M.A. Shevtsov, R. Z. Valiev, Enhanced osseointegrative properties of ultra-fine-grained titanium implants modified by chemical etching and atomic layer deposition, ACS Biomater. Sci. Eng. 4 (2018) 3268–3281, https://doi.org/10.1021/acsbiomaterials.8b00342.
[223] M. Ortiz-Hernandez, K.S. Rappe, M. Molmeneu, C. Mas-Moruno, J. Guillem-Marti, M. Punset, C. Caparros, J. Calero, J. Franch, M. Fernandez-Fairen, J. Gil, Two different strategies to enhance osseointegration in porous titanium: inorganic thermo-chemical treatment versus organic coating by peptide adsorption, Int. J. Mol. Sci. 19 (2018) 2574, https://doi.org/10.3390/ijms19092574.
[224] P. Chen, T. Aso, R. Sasaki, M. Ashida, Y. Tsutsumi, H. Doi, T. Hanawa, Adhesion and differentiation behaviors of mesenchymal stem cells on titanium with micrometer and nanometer-scale grid patterns produced by femtosecond laser irradiation, J. Biomed. Mater. Res. 106 (2018) 2735–2743, https://doi.org/10.1002/jbm.a.36503.
[225] Sunarso, R. Toita, K. Tsuru, K. Ishikawa, Immobilization of calcium and phosphate ions improves the osteoconductivity of titanium implants, Mater. Sci. Eng. C 68 (2016) 291–298, https://doi.org/10.1016/j.msec.2016.05.090.
[226] M. Nakagawa, L. Zhang, K. Udoh, S. Matsuya, K. Ishikawa, Effects of hydrothermal treatment with $CaCl_2$ solution on surface property and cell response of titanium implants, J. Mater. Sci. Mater. Med. 16 (2005) 985–991, https://doi.org/10.1007/s10856-005-4753-0.
[227] S.S. Lim, C.Y. Chai, H.-S. Loh, In vitro evaluation of osteoblast adhesion, proliferation and differentiation on chitosan-$TiO_2$ nanotubes scaffolds with $Ca^{2+}$ ions, Mater. Sci. Eng. C 76 (2017) 144–152, https://doi.org/10.1016/j.msec.2017.03.075.
[228] R. Sawada, K. Kono, K. Isama, Y. Haishima, A. Matsuoka, Calcium-incorporated titanium surfaces influence the osteogenic differentiation of human mesenchymal stem cells, J. Biomed. Mater. Res. 101 (2013) 2573–2585, https://doi.org/10.1002/jbm.a.34566.
[229] X. Li, X. Yang, X. Liu, W. He, Q. Huang, S. Li, Q. Feng, Calcium carbonate nanoparticles promote osteogenesis compared to adipogenesis in human bone-marrow mesenchymal stem cells, Prog. Nat. Sci. Mater Int. 28 (2018) 598–608, https://doi.org/10.1016/j.pnsc.2018.09.004.
[230] K. Lin, L. Xia, J. Gan, Z. Zhang, H. Chen, X. Jiang, J. Chang, Tailoring the nanostructured surfaces of hydroxyapatite bioceramics to promote protein adsorption, osteoblast growth, and osteogenic differentiation, ACS Appl. Mater. Interfaces 5 (2013) 8008–8017, https://doi.org/10.1021/am402089w.
[231] A. Mello, Z. Hong, A.M. Rossi, L. Luan, M. Farina, W. Querido, J. Eon, J. Terra, G. Balasundaram, T. Webster, A. Feinerman, D.E. Ellis, J.B. Ketterson, C. L. Ferreira, Osteoblast proliferation on hydroxyapatite thin coatings produced by right angle magnetron sputtering, Biomed. Mater. 2 (2007) 67–77, https://doi.org/10.1088/1748-6041/2/2/003.
[232] M.L. Cairns, B.J. Meenan, G.A. Burke, A.R. Boyd, Influence of surface topography on osteoblast response to fibronectin coated calcium phosphate thin films, Colloids Surf., B 78 (2010) 283–290, https://doi.org/10.1016/j.colsurfb.2010.03.013.
[233] P. Kasten, I. Beyen, P. Niemeyer, R. Luginbühl, M. Bohner, W. Richter, Porosity and pore size of β-tricalcium phosphate scaffold can influence protein production and osteogenic differentiation of human mesenchymal stem cells: an in vitro and in vivo study, Acta Biomater. 4 (2008) 1904–1915, https://doi.org/10.1016/j.actbio.2008.05.017.
[234] M. M McCafferty, G.A. Burke, B.J. Meenan, Calcium phosphate thin films enhance the response of human mesenchymal stem cells to nanostructured titanium surfaces, J. Tissue Eng. 5 (2014) 1–12, https://doi.org/10.1177/2041731414537513.